

ON THE GENERATION OF  
AURORAL KILOMETRIC RADIATION

by

James Lauer Green

A thesis submitted in partial fulfillment  
of the requirements for the degree of  
Doctor of Philosophy in Physics  
in the Graduate College of  
The University of Iowa

July, 1979

Thesis supervisor: Professor Donald A. Gurnett

## ACKNOWLEDGEMENTS

My sincerest thanks and gratitude go to Dr. Donald Gurnett who has helped shape my sense of scientific curiosity and has allowed me to travel extensively to obtain data and present scientific papers. Without Don's guidance and help this thesis would not have been possible. Fruitful discussions with Drs. David Barbosa, John Craven, Michelle Thomsen, Stanley Shawhan, and Ching S. Wu, all of whom I hold in the highest esteem, are gratefully acknowledged. Special thanks go to Dr. Thomas Potemra for the use of the Triad data, Dr. Nicolaos Saflekos for help in the analyzation of Triad magnetometer data, Dr. Robert Hoffman for the use and interpretation of the AE-D particle data, and Dr. James Van Allen for the use of the Hawkeye magnetometer data. In addition, Dr. Van Allen has played an extremely important role (arranging for financial support) in obtaining the Hawkeye spacecraft data for which this study makes ample use. Much of the computer programming in the emission cone study (Section II) was accomplished with the expert help of Dennis Gallagher.

I wish also to thank S. Faven and J. Gunther for their efforts in making the Triad magnetometer data quickly available and gratefully acknowledge the assistance of S. J. Akasofu of the Geophysical Institute, University of Alaska, in the acquisition of all Triad data used in this study. Ron Janetzke aided me in obtaining the AE-D particle

data and key punching help by Ann Persoon deserves special mention. I am pleased to thank Kathy Goodner who expertly typed this thesis and Joyce Chrisinger and Jeana Wonderlich who did a beautiful job in drafting all the figures.

The research at the University of Iowa was supported by the National Aeronautics and Space Administration through Grants NGL-16-001-002 and NGL 16-001-043, Contracts NAS1-11257 and NAS1-13129, with Langley Research Center, and Contracts NAS5-11074 and NAS5-11431 with Goddard Space Flight Center and by the Office of Naval Research through Contract N00014-76-C-0016.

I dedicate this thesis to my wife Diana which I hope will repay her, in some way, for the dedication she has shown me throughout my graduate career.

## ABSTRACT

Simultaneous observations between the Hawkeye spacecraft in the AKR emission cone and the low altitude polar orbiting spacecraft Triad and AE-D reveal that auroral kilometric radiation (AKR) is correlated with a variety of auroral particle precipitation in the evening to midnight local time sector. It is found that as the AKR intensity increases so does the integrated current sheet intensity of auroral zone field-aligned currents observed by Triad increase from a survey of 257 simultaneous observations. Statistically, the linear correlation coefficient between the log of the AKR power flux and the log of the current sheet intensity is 0.57.

A qualitative survey based on 93 simultaneous observations of AKR and electron particle precipitation observed by AE-D shows that auroral kilometric radiation is more closely associated with inverted-V electron precipitation than with plasma sheet precipitation. Quantitatively, a good correlation (linear correlation coefficient of 0.65) is found between the log of the AKR power flux and the peak energy of inverted-V events. In addition, systematic increases in the differential particle flux in the high energy tail of the most field-aligned portion ( $\sim 0 \pm 7 \frac{1}{2}^\circ$  pitch angle) of the distribution functions of the inverted-V events are associated with AKR power flux increases. From a determination of the simultaneous power in the high energy tail of



the precipitating inverted-V events and the AKR bursts, the efficiency of converting the charge particle energy into EM radiation increases from  $10^{-5}\%$  to a maximum of about 1%. The 1% conversion efficiency may be possible for a dynamic range in AKR intensity as large as 40 db.

Auroral kilometric radiation observations from Hawkeye during low altitude (2.0 to 2.5  $R_E$ ) auroral zone passes reveal that intense AKR has a low frequency cutoff near the local electron gyrofrequency ( $f_g^-$ ) with maximum electric field strengths as large as 12 mV/m. The large electric fields observed near  $f_g^-$  are consistent with high altitude observations of AKR using a simple  $1/R^2$  scaling indicating that the kilometric radiation in or near the average source region is almost completely electromagnetic. Evidence is presented which explains the observed frequency cutoff as being consistent with AKR propagating in the right-hand extraordinary (R-X) polarized mode.

The results presented in this study indicate that kilometric radiation is generated by inverted-V electron distribution functions in a direct coupling mechanism between particle energy and R-X mode electromagnetic waves in the region of the auroral zone where  $f_g^- \gg f_p^-$  (the local electron plasma frequency). Only two proposed generation mechanisms are able to account for most of the observations. It is not possible to conclusively determine if either of these direct generation mechanisms plays a major role in the generation of auroral kilometric radiation.

## TABLE OF CONTENTS

	Page
LIST OF TABLES . . . . .	vii
LIST OF FIGURES . . . . .	viii
I. INTRODUCTION . . . . .	1
II. THE DETAILED INTENSITY DISTRIBUTION OF THE AKR EMISSION CONE . . . . .	6
III. A CORRELATION BETWEEN AURORAL KILOMETRIC RADIATION AND FIELD-ALIGNED CURRENTS . . . . .	14
A. Observations Of Field-Aligned Currents From Triad . . .	14
B. Constraints On the Triad and Hawkeye Observations . . .	17
C. Qualitative Comparison Of Auroral Kilometric Radiation and Field-Aligned Currents . . . . .	18
D. Quantitative Analysis Of Auroral Kilometric Radiation and Field-Aligned Currents . . . . .	20
E. Possible Sources Of Scatter In the Correlation Between AKR and Field-Aligned Currents . . . . .	21
IV. AN INVESTIGATION OF THE RELATIONSHIP BETWEEN AURORAL KILOMETRIC RADIATION AND AURORAL PARTICLE PRECIPITATION . .	23
A. Constraints On the AE-D and Hawkeye Observations . . .	23
B. Qualitative Comparison Of Auroral Kilometric Radiation and Auroral Particle Precipitation . . . . .	25
C. Quantitative Analysis Of Auroral Kilometric Radiation and Inverted-V Events . . . . .	29
D. Possible Sources Of Scatter In the Correlation Between AKR and Inverted-V Events . . . . .	38
V. INTERPRETATIONS AND DISCUSSION OF THE SIMULTANEOUS OBSERVATIONS OF AURORAL KILOMETRIC RADIATION AND AURORAL PARTICLE PRECIPITATION . . . . .	40
A. Possible Role Of Field-Aligned Currents In the Generation and Amplification Of AKR . . . . .	40
B. Possible Role Of Inverted-V Electron Precipitation In the Generation and Amplification Of AKR . . . . .	44

	Page
VI. HAWKEYE PLASMA WAVE OBSERVATIONS OF AURORAL KILOMETRIC RADIATION AT LOW ALTITUDES IN THE AURORAL ZONE . . . . .	46
A. The Observed Low Frequency Cutoff Of AKR At the Local Electron Gyrofrequency . . . . .	46
B. Interpretation Of the Low Frequency Cutoff As a Propagation Effect . . . . .	49
VII. COMPARISON OF THE CHARACTERISTICS OF AKR PRESENTED IN THIS STUDY WITH PROPOSED GENERATION MECHANISMS . . . . .	51
A. Introduction . . . . .	51
B. Review Of the Theory Of Amplified Doppler Shifted Gyroemission As a Mechanism For the Generation and Amplification Of AKR . . . . .	54
C. Review Of the Theory Of Relativistic Normal Cyclotron Resonance As a Mechanism For the Generation and Amplification Of AKR . . . . .	60
D. Comparison Of Direct Generation Mechanisms With AE-D Plasma Observations . . . . .	64
E. Comparison Of the Direct Generation Mechanisms With Hawkeye Emission-Cone Observations . . . . .	70
VIII. CONCLUSIONS . . . . .	73
REFERENCES . . . . .	77
APPENDIX A: TABLES . . . . .	84
APPENDIX B: FIGURES . . . . .	89

## LIST OF TABLES

	Page
Table 1	
The distribution of electric field measurements when Hawkeye is in the AKR emission cone as a function of AE-D precipitating electron measure- ments in the auroral oval from 20 hours to 01 hour magnetic local time. . . . .	85
Table 2	
Proposed generation mechanisms. . . . .	86

## LIST OF FIGURES

	Page
<p>Figure 1</p>	<p>Bursts or storms of auroral kilometric radiation as observed by the Hawkeye spacecraft near apogee at 178, 100, 56.2 and 42.2 kHz. The sporadic nature of this radiation is exhibited in the intensity of the noise which varies by more than 20 db in a few minutes or less and 80 db over the course of the storm. Storms of auroral kilometric radiation lasting for several hours are not uncommon. . . . .</p>
	90
<p>Figure 2</p>	<p>Schematic representation of the results from Gallagher and Gurnett [1979] on their determination of the AKR source region(s). The average source region of auroral kilometric radiation at 178 kHz is found in the 11 to 23 hour magnetic local time meridian at approximately <math>2.5 R_E</math> (earth radius) geocentric radial distance along auroral field lines (<math>\sim 70^\circ</math> invariant latitude) on the nightside. The borders of the emission pattern (shaded region) were defined by a drop in the observed AKR power flux by two or more orders of magnitude. . . . .</p>
	92

Figure 3      The frequency of occurrence diagram of auroral kilometric radiation (from Green et al. [1977]) as observed from the IMP-6 and Hawkeye spacecraft at 178 kHz as a function of magnetic local time and magnetic latitude. Note that the threshold used varied as  $1/R^2$ . Since the source region of AKR was not well known at the time of this study, the R variable used was the satellite's geocentric radial distance. . . . . 94

Figure 4      Scatter plot of simultaneous measurements of AKR electric field intensities at 178 kHz from IMP-6 (normalized to  $30 R_E$ ) and the AE index from a paper by Voots et al. [1977]. Each point represents a 10-minute average obtained while IMP-6 was in the AKR emission cone (black shading in Figure 2) which was determined by Green et al. [1977]. The linear correlation coefficient of the log of the AKR power flux versus the log of the AE index was found to be 0.51. . . . . 96

Figure 5      Two dimensional polar plots of the intensity distribution of the AKR emission cone in the northern hemisphere are shown in two latitude

and local time coordinate systems. The third dimension, radial distance, is taken into account by applying a  $1/R^2$  scaling to the power flux measurements relative to the origin of each coordinate system and normalizing to  $7 R_E$  about the origin. The left-hand panel has organized all the Hawkeye and IMP-6 observations in the familiar earth-centered system of magnetic latitude and magnetic local time. The best representation of the intensity distribution of the AKR emission cone (shaded) is found in the source-centered plot (right-hand panel) where all the observations are transformed into a coordinate system with the average source region of AKR at the origin. The average source region used is consistent with the results of Gallagher and Gurnett [1979]. . . . . 98

Figure 6

The source-centered AKR emission cone at 178 kHz is shown in greater detail at five representative local times. Note the rapid drop in the average intensity (2 to 3 orders of magnitude) as a function of decreasing latitude for the 8.5 and 4 hours local time side panels. There

is less than 10 db variation in the averaged intensity in almost all of the emission cone as illustrated in the 18.5 and 0.5 hours local time side panels. Unlike the intense decametric radio emissions from Jupiter which are believed to be generated into a large hollow cone its terrestrial counterpart, auroral kilometric radiation, is beamed into a nearly homogenous emission cone. . . . . 100

Figure 7

The top panel presents simultaneous  $(R/7 R_E)^2$  normalized (with respect to the average AKR source region, see text) power flux measurements from the Hawkeye and IMP-6 spacecrafts. The bottom shows the trajectories of these two satellites in the emission cone (crossed-hatched boundaries) during the time of the simultaneous observations. All enhanced emissions observed by Hawkeye are attributed to auroral kilometric radiation. When IMP-6 is in the emission cone (after ~ 23 hours universal time) both satellites observe nearly identical AKR power flux illustrating that the source of



auroral kilometric radiation illuminates the entire emission cone uniformly and simultaneously. . . . . 102

Figure 8

The three panels (A, B, and Z) on the right-hand side are plots of the measured ambient magnetic field ( $B_M$ ) from the triaxial sensors on board Triad minus a theoretical geomagnetic field ( $B_T$ ) in units of gammas. The large perturbation from the baseline formed by the  $B_M - B_T$  curve in the A panel is attributed to two east-west field-aligned current sheets. The left-hand side illustrates the orientation of the A, B, and Z magnetic field sensors onboard Triad during a pass over College, Alaska. The direction of the magnetic field sensors is used in determining the orientation of the auroral zone current sheets. . . . . 104

Figure 9

A polar plot in magnetic local time and invariant latitude of field-aligned currents observed by Triad during weakly disturbed times ( $|AL| < 100\gamma$ ) from Iijima and Potemra [1976]. The crossed-hatched section from 19 hours to 01 hours is

the magnetic local time region where the most intense bursts of AKR are believed to originate. Note, also, that this is the region where the most complicated auroral zone current system is found. Only Triad magnetometer measurements inside the cross-hatched region will be used in this study. . . . . 106

Figure 10

The top panel shows power flux measurements as a function of time from the Hawkeye satellite while it is in the AKR emission cone during the four consecutive passes of the Triad spacecraft through the auroral oval in the northern hemisphere. The Triad magnetometer measurements from the A sensor plotted with respect to the baseline formed by  $B_M - B_T$  are shown in the bottom panels, A, B, C, and D. Note that when Triad observes large deflections in the magnetic field due to field-aligned currents Hawkeye observes intense kilometric radiation (times B, C, and D) but when little disturbances in the auroral zone are found, Panel A, Hawkeye does not detect kilometric radiation above the receiver's threshold. . . . . 108

Figure 11

Simultaneous power flux measurements of AKR at 178 kHz versus the integrated current intensity of auroral zone field-aligned currents. A  $(R/7 R_E)^2$  normalization to the power flux measurements is applied to take into account the radial dependence of this radiation. The R variable is the distances from the satellite to the average source region of AKR (see text). The triangles represent an upper limit to the power flux since AKR was not detected at those times. A correlation can be seen in that, as the power flux increases so does the integrated current sheet intensity of field-aligned currents. . . . . 110

Figure 12

The top panel shows electric field measurements as a function of time from Hawkeye while it is in the AKR emission cone during three consecutive AE-D auroral zone passes. The panels labeled orbit 698, 699, 700 are energy-time spectrograms from the LEE experiment onboard AE-D. Note that AKR appears to be more closely related to inverted-V electron precipitation than to plasma sheet precipitation. . . . . 112

- Figure 13 Scatter plot of simultaneous measurements of AKR intensity (normalized to  $7 R_E$  and having a  $1/R^2$  scaling) and the peak energy in inverted-V events observed by AE-D. The correlation coefficient between the log of the power flux and the peak energy is 0.65. . . . . 114
- Figure 14 Three electron distribution functions at  $\sim 0^\circ$  pitch angle ( $\pm 7 1/2^\circ$ ) during the inverted-V events used in Figure 13. In the upper right corner of each panel is the simultaneous AKR power flux measurement from the Hawkeye spacecraft. These three distribution functions are representative of the AE-D observations during times of weak (top panel), moderate (center panel), and intense (bottom panel) auroral kilometric radiation. . . . . 116
- Figure 15 Scatter plot of the  $(R/7 R_E)^2$  normalized AKR intensity at 178 kHz and the effective tail temperature ( $T_{||}$  defined in text) of the electron distribution functions at  $\sim 0^\circ$  pitch angle of the inverted-V events used in Figure 13. The triangles represent times when auroral

kilometric radiation was not detected above the receivers threshold. During times when the power flux is weak ( $< 10^{-17}$  watts/(m<sup>2</sup>Hz))  $T_{||}$  is less than  $1.8 \times 10^8$  °K. In addition, for  $T_{||}$  greater than  $1.8 \times 10^8$  °K the associated AKR power flux is moderate ( $10^{-17}$  to  $10^{-15}$  watts/(m<sup>2</sup>Hz)) to intense ( $> 10^{-15}$  watts/(m<sup>2</sup>Hz)). . . . 118

Figure 16

Scatter plot of simultaneous measurements of AKR intensity at 178 kHz (normalized to  $7 R_E$  and having a  $1/R^2$  scaling) and the energy flux of the same inverted-V events plotted in Figures 13 and 15. The top scale is an estimate of the amount of power available in the precipitating inverted-V events. The far right hand scale is an estimate of the amount of power in the AKR bursts. Note that if the precipitating inverted-V events are the sole energy reservoir for AKR that the generation mechanism can have a maximum efficiency of about 1%. . . . . 120

Figure 17

Scatter plot of simultaneous measurements of AKR intensity at 178 kHz (normalized to  $7 R_E$  and having a  $1/R^2$  scaling) versus the energy

flux of the inverted-V events in Figure 16 integrated from 6.88 keV to 25 keV. If the high energy tail in the distribution function of the precipitating inverted-V events plays a major role in the generation or amplification of auroral kilometric radiation then efficiencies as high as 0.1 to 1% may be possible for a dynamic range in AKR intensity as large as 40 db. . . . . 122

Figure 18

The main feature of intense auroral kilometric radiation observed by Hawkeye during low altitude auroral zone passes is that it occurs in regions where the wave frequency (178 kHz in this case) is greater than both the local electron gyrofrequency and the local electron plasma frequency. The dashed line marked  $f_g^-$  is the measured local electron gyrofrequency. The electron plasma frequency,  $f_p^-$ , is estimated on the basis that it is the low-frequency cutoff of the continuum radiation and the upper-frequency cutoff of the auroral hiss. . . . . 124

Figure 19

A scatter plot of electric field measurements at 178 kHz from Hawkeye southern passes on the night-side of the earth plotted as a function of the ratio of the wave frequency to the local electron gyrofrequency ( $f/f_g^-$ ). The maximum electric field of AKR measured is nearly 12 mV/m. Note that there is a sharp cutoff of at least five orders of magnitude in the AKR intensity at the local electron gyrofrequency. To clearly illustrate the cutoff of AKR at  $f_g^-$  passes for which intense auroral hiss emissions at 178 kHz occurred were eliminated. Virtually all the data below  $10^{-16}$  watts/(m<sup>2</sup>Hz) is continuum radiation which displays no cutoff at  $f = f_g^-$ . . . . . 126

Figure 20

The expected radial variations of  $f_p^-$ ,  $f_g^-$ , and  $f_{R=0}$  along an auroral magnetic field line. The frequencies  $f_p^-$  and  $f_{R=0}$  present propagation barriers or cutoffs to downward propagating radiation with left-hand (L-O) and right-hand (R-X) polarizations, respectively. Note that in regions where  $f_p^- \ll f_g^-$  then  $f_g^- \simeq f_{R=0}$ . . . . . 128

Figure 21      The top and bottom panels are contour plots of typical electron distribution functions  $F(v)$ , in velocity space used in the theories of Wu and Lee [1979] (top panel) and Melrose [1976] (bottom panel) for the generation of AKR. In the bottom panel the source of free energy for AKR amplification is in the precipitating portion of  $F(v)$ . The contour at  $1 \text{ sec}^3/\text{km}^6$  shows the shape of a high velocity precipitating beam (large  $V_{||}$ ) which also extends to large perpendicular velocities. In the top panel the source of free energy is in the ascending part of  $F(v)$ . This distribution has a loss-cone feature which is characterized by a depletion of upgoing electrons having small pitch angles (small  $V_{\perp}$ ). . . . . 130

Figure 22      On the left-hand side are three contour plots of inverted-V electron distribution functions in velocity space observed by AE-D. These three distributions are associated with weak (top), moderate (center) and intense (bottom) auroral kilometric radiation observed simultaneously by Hawkeye. The corresponding energy flux of each distribution as a function of pitch angle



is shown on the right-hand side. Note that in precipitating portion of the distribution functions (from  $0$  to  $90^\circ$ ) there is at least an order of magnitude more energy than in the ascending portion (from  $90^\circ$  to  $180^\circ$ ). The high velocity beam or peak in the distribution functions, nearly centered about zero degrees pitch angle, is a characteristic feature of inverted-V electron distributions. . . . . 132

Figure 23

Ray paths in the noon-midnight meridian for the Melrose (bottom panel) and the Wu and Lee (top panel) generation mechanisms in the model magnetosphere shown in Figure 20. The resultant angular distribution for Melrose's mechanism (shaded region, bottom panel) is that of a filled-in emission cone and agrees well with the observations (see Figure 5 or 6). However, in the absence of near source propagation effects the Wu and Lee mechanism (shaded region, top panel) produces a hollow emission cone. . . . . 134

## I. INTRODUCTION

Auroral kilometric radiation or AKR is the most intense electromagnetic radiation that is generated by the earth's magnetosphere. AKR is observed in the frequency range from 30 kHz to about 700 kHz. A typical spectrum of auroral kilometric radiation (see Gurnett [1974] or Kaiser and Alexander [1977a]) decreases rapidly with increasing and decreasing frequency from the spectral peak near 250 kHz. Thus, the AKR spectrum has almost a spike appearance in plots of intensity versus frequency with a width (bandwidth) of 200 kHz at half of the intensity of the spectral peak. Kaiser and Alexander [1977a] have determined that the frequency of the spectral peak of auroral kilometric radiation varies inversely with geomagnetic activity from 300 kHz during very quiet times to below 200 kHz during very disturbed times. Gurnett [1974] estimated that at peak intensity the total power of auroral kilometric radiation is sometimes as high as  $10^9$  watts.

An example of kilometric radiation observed near apogee ( $\sim 22 R_E$ ,  $R_E$  = earth radius) by the Hawkeye spacecraft is illustrated in Figure 1. This figure shows the electric field intensities (height of vertical bars) in units of power flux of auroral kilometric radiation at frequencies 178, 100, 56.2 and 42.2 kHz. As can be seen in Figure 1, auroral kilometric radiation occurs in distinct bursts or storms

lasting typically from tens of minutes to hours and extending above the receiver noise level by 60 db or more.

The scientific research on auroral kilometric radiation in the past five years has primarily centered on determining the source location(s) for this radio emission. The origin of this radiation has been difficult to determine since auroral kilometric radiation is extremely sporadic and can vary in intensity by as much as 80 db on a time scale of minutes and possibly seconds (see Figure 1). A recent study by Gallagher and Gurnett [1979], however, demonstrates quite clearly that the intense kilometric radiation near 178 kHz is generated, on the average, at low altitudes ( $\sim 2.5 R_E$ ) on the nightside of the earth at auroral zone latitudes. The source region(s) of auroral kilometric radiation, shown schematically in Figure 2 from Gallagher and Gurnett [1979], agrees extremely well with the previous published results of Gurnett [1974] and of Kurth et al. [1975] and corresponds to the "region of frequent TKR (or AKR) activity" determined by Alexander and Kaiser [1976].

The angular distribution of auroral kilometric radiation was determined at several frequencies from a frequency of occurrence survey by Green et al. [1977]. Figure 3 is from Green et al. [1977] and is a frequency of occurrence diagram of kilometric radiation at 178 kHz. The frequency of occurrence analysis determines the percentage of times Hawkeye and IMP-6 observed kilometric radiation at the magnetic latitude and magnetic local time of the spacecraft. The black shading in Figure 3, termed the AKR emission cone, is the region of magnetic latitude

and magnetic local time where Hawkeye and IMP-6 had the highest probability of observing auroral kilometric radiation. Green et al. [1977] found that at 178 kHz the highest probability of observing AKR occurs at magnetic latitudes  $\geq 60^\circ$  on the dayside of the earth, and  $\geq 20^\circ$  on the nightside (see Figure 3). In addition, from simultaneous observations from IMP-8 and Hawkeye and from ray tracing in a model magnetosphere Green et al. [1977] concluded that the topside plasmasphere on the nightside produces an abrupt latitude propagation cutoff to the radiation and prevents auroral kilometric radiation generated in the southern hemisphere from being observed in the northern hemisphere. Figure 2 also schematically illustrates these results.

From ray tracing calculations Green et al. [1977] concluded that auroral kilometric radiation propagating in the R-X (right-hand extraordinary) mode could reproduce the angular distribution (from Figure 3) observed. Gurnett and Green [1978] using cutoffs in the radio emission spectrum of auroral kilometric radiation observed by the Hawkeye spacecraft near perigee in the southern hemisphere (possibly even in the source region) determined that AKR was propagating in the R-X mode. Direct measurements of auroral kilometric radiation by Kaiser et al. [1978] confirmed these results. In addition, Kaiser et al. have observed the degree of polarization in some kilometric storms to be as high as 95%.

One of the most interesting aspects of auroral kilometric radiation is that it has been observed to be related to auroral phenomena.

The intense kilometric radiation has been correlated with high-latitude ground-based magnetic disturbances produced by the auroral electrojet current as measured by the AE index. Dunckel et al. [1970] were the first to determine that AE was highest at the time of AKR noise bursts and significantly lower both before and after the bursts from a study of 32 AKR storms. The most extensive study of the correlation between auroral kilometric radiation and the AE index was done by Voots et al. [1977]. Figure 4 is from Voots et al. [1977] and illustrates that as the mean of the AKR power flux increases so does the mean of the AE index. Kaiser and Alexander [1977b] like Voots et al. [1977] found that there is a good qualitative association in individual AKR bursts with AE.

A close association between auroral kilometric radiation and discrete auroral arcs was demonstrated by Gurnett [1974] and by Kurth et al. [1975]. This was accomplished by comparing photographs of the nightside auroral zone taken by the optical scanner on board the DAPP satellite with the electric field measurements of AKR by IMP-6. The occurrence of sporadic bursts of the kilometric radiation with the occurrence of discrete auroral arcs led Kurth et al. [1975] to refer to this radio noise as auroral kilometric radiation which, up until then, was commonly referred to as terrestrial kilometric radiation (TKR). In addition, Gurnett [1974] concluded that auroral kilometric radiation must be associated with inverted-V electron precipitation in the auroral zone since Ackerson and Frank [1972] had previously shown that inverted-V electron precipitation events are correlated with discrete auroral arcs.

The purpose of this thesis is to investigate possible correlations between auroral kilometric radiation and auroral zone particle precipitation to determine if there are specific features in the distributions of the precipitating particles which play a major role in the generation or amplification of kilometric radiation. To accomplish the task of correlating auroral kilometric radiation with particle precipitation, simultaneous measurements from several satellites will be used. This thesis uses the polar orbiting Hawkeye spacecraft, far from the earth ( $\geq 7 R_E$ ), to observe the integrated AKR power flux intensity while low altitude polar orbiting spacecraft such as Triad and AE-D will be used to measure field-aligned currents and electron precipitation, respectively, in the pre-midnight auroral zone. Field-aligned currents determined from magnetic field observations are a measure of the current along the geomagnetic field due to all species of charge particles at all energies.

In addition, this thesis presents low altitude auroral zone observations of auroral kilometric radiation from the Hawkeye spacecraft in or near the average source region. The maximum electric field strength measured in or near the average source region is presented. From cutoffs in the radio emission spectrum of auroral zone emissions the polarization of auroral kilometric radiation and characteristic frequencies in the auroral zone plasma is determined. These observations aid in the determination of which proposed generation mechanism(s) are most consistent with the observations.

## II. THE DETAILED INTENSITY DISTRIBUTION OF THE AKR EMISSION CONE

Multi-satellite comparisons between auroral kilometric radiation and auroral particle precipitation can not be properly carried out without considering Hawkeye's position in the illumination pattern of the kilometric emission. It is important to note that the decametric radiation from Jupiter, which may be the Jovian counterpart to the earth's auroral kilometric radiation, is believed to be beamed into a hollow emission cone (see for example, Dulk [1970]). The frequency of occurrence survey in Figure 3 (from Green et al. [1977]) illustrates that the AKR emission cone does appear to be filled in to at least a power flux level of  $7.35 \times 10^{-16}$  watts/(m<sup>2</sup>Hz) at  $7 R_E$  (normalized to  $7 R_E$ ). It should be noted that bursts of auroral kilometric radiation with intensities greater than  $10^{-14}$  watts/(m<sup>2</sup>Hz) (normalized to  $7 R_E$ ) are common. Thus, Figure 3 does not rule out the possibility that, like the Jovian decametric radiation, the center of the AKR emission cone may at least be partially hollow. If the emission cone is hollow it would greatly complicate multi-spacecraft comparisons since special considerations of Hawkeye's position in the emission cone would have to be made.

It is clear that a study of the detailed intensity distribution of AKR must first be done to determine when the Hawkeye observations are representative of kilometric radio emission from the auroral zone.



The satellites used to determine the intensity distribution of the AKR emission cone at 178 kHz are Hawkeye and IMP-6, since they have nearly identical plasma wave experiments whose outputs, once calibrated, are easily combined (see Green et al. [1977]). In addition, the combined orbital coverage of Hawkeye and IMP-6 provided observations over essentially the entire northern hemisphere (see Figure 1 of Gallagher and Gurnett [1979]). Hawkeye and IMP-6 were in highly elliptical earth orbits. The apogee of Hawkeye was over the north polar region (inclination of  $89^\circ$ ) at a geocentric radial distance of nearly  $22 R_E$ . The Hawkeye spacecraft provided observations of auroral kilometric radiation up to 46 hours for a given 52 hour orbit from launch on June 3, 1974, until it reentered the atmosphere on April 28, 1978. The apogee of IMP-6 was near the equatorial plane (orbit inclination of  $28.7^\circ$ ) at about  $33 R_E$ . IMP-6 observed auroral kilometric radiation less than 50% of the time.

Each of these satellites had a long dipole antenna for electric field-measurements. The Hawkeye antenna was the shortest, measuring 42.45 meters from tip-to-tip and the IMP-6 antenna had a 92.5 meter tip-to-tip length. To determine the electric field intensity at various frequencies the antenna signals were periodically analyzed with spectrum analyzers. The spectrum analyzers on both Hawkeye and IMP-6 had 16 frequency bands with center frequencies from 36 Hz to 178 kHz on IMP-6 and from 1.78 Hz to 178 kHz on Hawkeye. Only observations of auroral kilometric radiation at 178 kHz will be used in this study.



Plotted in polar form, Figure 5 shows equal intensity contours of AKR power flux measurements from 3.3 years of Hawkeye observations and 3.1 years of IMP-6 observations for two different local time and latitude coordinate systems. Observations made at radial distances less than  $5 R_E$  are not used in the determination of the intensity distribution of the emission cone in order to avoid complications due to near earth propagation effects, such as reflection or refraction of AKR at the plasmapause (see Green et al. [1977]). The left hand panel of Figure 5 organizes all the satellite observations into the familiar earth-centered coordinate system of magnetic latitude and magnetic local time. In this coordinate system the position of the satellite at the time of an electric field observation is determined to be in one of 864 bins which divide up the northern hemisphere into blocks of size one-half hour local time ( $7 \frac{1}{2}^\circ$  longitude) by  $5^\circ$  latitude. The observation is placed into the appropriate bin after the normalization factor,

$$P = \left( \frac{R}{7 R_E} \right)^2 P_o \quad (1)$$

has been applied, where  $P_o$  is a spin-averaged power flux measurement. The  $(R/7 R_E)^2$  factor takes into account the  $1/R^2$  radial dependence of auroral kilometric radiation and normalizes all observations as if they were made by one satellite in a circular polar orbit of radius  $7 R_E$ . The  $R$  factor in the  $(R/7 R_E)^2$  normalization term is the distance from the center of the earth (coordinate origin for left panel Figure 5) to the satellites position at the time of each observation. All the power

flux measurements in each bin, after all the data has been sorted, are averaged to obtain a representative measurement at that local time and latitude from which intensity contours can easily be drawn.

Ideally, the  $R$  in the normalization term should be the distance from where the radiation was generated to the observation position. The right hand panel of Figure 5 shows the results of a coordinate transformation on the same data used in the left hand panel, which takes into account the  $1/R^2$  drop in the intensity of the AKR emission cone by taking as the coordinate origin the average AKR source region. The average source region used is consistent with the observational results of Gallagher and Gurnett [1979] ( $2.5 R_E$  along a  $70^\circ$  invariant latitude geomagnetic field line at 23 hours magnetic local time). Each Hawkeye and IMP-6 position is transformed into a new local time and latitude coordinate with respect to the average source region origin. The noon-midnight and dawn-dusk planes in the new source-centered coordinate system are parallel to the respective planes in the earth-centered system. Each observation is scaled to take into account the  $1/R^2$  drop in intensity, relative to the average source, and placed into one of the new 864 latitude and local time bins where it is averaged. The source-centered contour pattern of Figure 5 would be the same as what would be derived from observations made by a hypothetical satellite in a circular polar orbit of radius  $7 R_E$  about the average AKR source position used in this study.

The shaded region (in both polar plots of Figure 5) is the AKR emission cone as defined by the  $4 \times 10^{-16}$  watts/(m<sup>2</sup>Hz) contour. Note that in either coordinate systems the emission cone is well filled in. The earth-centered plot shows many large "islands" of enhanced intensity  $\geq 3 \times 10^{-15}$  watts/(m<sup>2</sup>Hz) inside the emission cone. From a comparison between both panels in Figure 5 it is evident that most of the large intensity islands in the earth-centered plot can be attributed to the use of the earth-centered coordinate system and not to any real physical intensity enhancements. Islands of enhanced intensity above the average power flux level of the cone in the source-centered plot which are not transformed away may be due to possible motion of the source region or perhaps to multiple sources which are effects that are impossible to correct for at this time.

A detailed look at data partially making up the source-centered plot of Figure 5 is shown in Figure 6. The side panels of Figure 6 show the bin averaged points in the 5° latitude bins (all spin-average data in each bin was averaged) at five representative local times. The error bar at the lower right in each side panel is the maximum probable error found in the latitude bins for each of the local times shown. Over 645,000 spin-averaged power flux observations from Hawkeye and IMP-6 went into this emission cone survey. The smallest number of observations in a bin was 71 and the largest was 1917. Thus, the intensity contour plots of Figure 5 (and Figure 6) are statistically well substantiated. Note the rapid drop in the average power flux (2 to 3 order of magnitude) as a function of decreasing latitude for the 8.5

and 4 hours local time side panels of Figure 6. The two dark shaded areas ( $\geq 2 \times 10^{-14}$  watts/(m<sup>2</sup>Hz)) inside the emission cone (also found in the earth-centered system of Figure 5) are observations from two separate intense kilometric radiation storms lasting tens of minutes which dominated the total averaged power flux in one or two coordinate bins. The 18.5 and 0.5 hours local time side panels of Figure 6 illustrate the extent to which the AKR emission is uniformly illuminated. There is less than 10 db variation in the averaged power flux intensity in almost all of the emission cone when plotted in the source-centered system.

It is now of interest to determine if individual bursts of auroral kilometric radiation uniformly and simultaneously illuminate the large emission cone illustrated in Figure 6 or could this region be the result of a much narrower cone or beam which varies in time. IMP-6 and Hawkeye were simultaneously in orbit from June to late September 1974. A computer search found six separate time periods for which both satellites were in the AKR emission cone in the northern hemisphere and simultaneous data were available. The top panel of Figure 7 presents simultaneous power flux spin-averaged observations from Hawkeye and IMP-6, for one specific case which is representative of the six other examples found by computer. The power flux observations have a  $(R/7 R_E)^2$  normalization relative to the average AKR source region. The open circles are the IMP-6 observations and the solid circles represent Hawkeye observations. The trajectories of these satellites within the emission cone depicted in Figure 5 are illustrated in the bottom panel of Figure 7 and they show that during the time of the simultaneous

observations the satellites were separated by more than  $60^\circ$  in latitude and as much as 12 hours in local time.

At 22 hours universal time (UT) IMP-6 is near perigee inside the plasmasphere (crossed-hatched region in the top panel of Figure 7). It is not until 2245 UT that IMP-6 crosses the plasmopause and by 23 hours UT is well situated in the average AKR emission cone. Meanwhile, Hawkeye from its position inside the emission cone at radial distances  $\geq 18 R_E$  has been observing intense bursts of auroral kilometric radiation during the entire time period. Because of the large densities found in the plasmasphere, auroral kilometric radiation cannot propagate inside the plasmasphere (see Gurnett [1974] or Green et al. [1977]). The moderately intense noise burst seen shortly after 2230 UT by IMP-6 (top panel, Figure 7) is called upper hybrid resonance noise and is commonly observed near the plasmopause (see Shaw and Gurnett [1975]). All enhanced emissions observed by IMP-6 after 23 hours are attributed to auroral kilometric radiation.

It is clear in Figure 7 that both satellites are observing the same intense source(s) of auroral kilometric radiation since at times the power flux observed by Hawkeye and IMP-6 are nearly identical to within less than 1 db. The variations in intensity between the simultaneous observations in Figure 7 are almost always less than 10 db which is consistent with the intensity variations in the detailed time-averaged intensity distribution of the emission cone shown in Figure 6. It is interesting to note that there is a difference of over 6 orders of magnitude in the power flux observed by IMP-6 from inside the

plasmasphere (2215 UT) to the time when it is in the AKR emission cone (2300 UT). Figure 7 illustrates that the source of auroral kilometric radiation illuminates the entire emission cone uniformly (within 10 db) and simultaneously, thus, supporting the results from Figure 6 on a much shorter time scale.

This section clearly demonstrates that multi-satellite comparisons can be carried out without considering Hawkeye's position in the emission cone. The size of the uniformly illuminated emission cone (see Figure 6) makes it possible to reliably use observations of auroral kilometric radiation from a large part of Hawkeye's orbit. To properly scale the radial dependence of kilometric radiation a  $(R/7 R_E)^2$  normalization factor relative to the average source region must be applied to each power flux measurement. This normalization factor scales all intensity measurements with an uncertainty of less than 10 db. With Hawkeye properly monitoring the integrated power flux of kilometric radiation generated in the auroral zone, simultaneous observations with low altitude polar orbiting satellites can now be employed to study correlations between auroral kilometric radiation and auroral particle precipitation.

### III. A CORRELATION BETWEEN AURORAL KILOMETRIC RADIATION AND FIELD-ALIGNED CURRENTS

#### A. Observations Of Field-Aligned Currents From Triad

The field-aligned currents used in this study are determined from triaxial fluxgate magnetometer measurements taken by the Triad spacecraft over College, Alaska. Launched on September 2, 1972, into nearly a circular orbit of 800 km altitude and inclination of  $90.1^\circ$ , Triad is gravity gradient stabilized and, thus, has a spin period of one revolution per orbit.

The determination of field-aligned currents from Triad magnetometer data is illustrated in Figure 8. The right-hand side of Figure 8 is a plot of the measured ambient field ( $B_M$ ) for the three sensors A, B, and Z on the spacecraft minus a theoretical geomagnetic model field ( $B_T$ , IGRF 1965.0 updated to time of data) as a function of time for day 78 of 1975. The vertical axis for each panel on the right side of Figure 8 is plotted in units of gammas and covers a range of 1000V. The magnetometer on board Triad measures ambient magnetic fields to a resolution of 12V. In the three panels on the right-hand side of Figure 8, deviations of  $B_M - B_T$  from 0V are due to sources such as field-aligned currents, spacecraft bias fields, inaccuracies in the model field, and slow deviations of the spacecraft altitude from a nominal position. Several of these sources can easily be recognized. For example, the difference



between the spacecraft altitude or position from its predicted position produces low frequency deviations with a period as long as 20 minutes in plots of  $B_M - B_T$  (see panels A, B, and Z in Figure 8). The spacecraft bias fields, due to inflight maneuvers just after launch, produce a constant magnetic field within the spacecraft which is also measured by the Triad magnetometer [see Armstrong and Zmuda, 1973]. Field-aligned currents produce obvious deviations from a baseline formed by  $B_M - B_T$  as easily seen in the A panel of Figure 8 from 25820 to 25970 seconds universal time. Little or no deflection in  $B_M - B_T$  due to field-aligned currents is seen in the B or Z panels which aids in the identification of this source as an external current. The orientation of the current sheets with respect to the spacecraft is believed to be the reason that the deflection from the baseline of  $B_M - B_T$  was almost entirely seen in the A panel (see below). The magnetic perturbations in the A panel of Figure 8 from 25840 to 25870 seconds and from 25915 to 25940 seconds are due to two east-west current sheets flowing out of and into the ionosphere, respectfully.

The orientation of the three magnetometer sensors on board Triad is illustrated on the left side of Figure 8. The A and B sensors are both horizontal with respect to the ground and are  $90^\circ$  apart. The B sensor is mounted  $45^\circ$  away from the spacecraft velocity vector (black arrow). The Z sensor completes the orthogonal coordinate system and points anti-parallel to the geomagnetic field vector at auroral zone latitudes in the northern hemisphere. When Triad is tracked by the College, Alaska station, the horizontal A sensor measures the component of the ambient



magnetic field that points nearly along constant invariant latitude. Field-aligned current sheets which lie entirely along constant invariant latitude produce magnetic fields which partially cancel the geomagnetic field measured in the A sensor. This can easily be seen by applying Ampere's law to a field-aligned current sheet. Using a coordinate system whose unit vectors ( $\hat{X}$ ,  $\hat{Y}$ ,  $-\hat{Z}$ ) are in the direction of the Triad magnetometer sensors (B, A, Z) a field-aligned current sheet of thickness  $dx$  and infinite length (in  $\hat{Y}$  direction) has a current  $j_z$  where

$$(\vec{\nabla} \times \vec{B}_c)_z = \mu_0 j_z \quad (2)$$

and  $B_c$  is the magnetic field of the current. Equation 2 becomes

$$\frac{\partial B_{cy}}{\partial x} - \frac{\partial B_{cx}}{\partial y} = \mu_0 j_z \quad ,$$

and as illustrated on the right side of Figure 8 panel B, if  $B_{cx} \simeq 0$ , i.e., no deflection or perturbation to the geomagnetic field then

$$\begin{aligned} \frac{\partial B_{cy}}{\partial x} &= \mu_0 j_z & ; \\ \int dB_{cy} &= \mu_0 \int j_z dx & ; \\ \Delta B &= \mu_0 J_c & ; \end{aligned} \quad (3)$$

thus,

$$J_c = 8 \times 10^{-4} (\Delta B) \text{ Amps/m}$$

where  $\Delta B$  is in gammas and is the magnetic deflection from the baseline formed by  $B_M - B_T$  in the A panel of Figure 8 and  $J_c$  is the integrated current across the sheet current. From Figure 8 panel A,  $\Delta B = 343\gamma$  or  $J_c = 0.27 \text{ A/m}$ .

#### B. Constraints On the Triad and Hawkeye Observations

Triad magnetometer measurements enabled Iijima and Potemra [1976] to determine a magnetic local time and invariant latitude summary of the large scale field-aligned currents flowing into and out of the ionosphere. Figure 9 illustrates the auroral zone current system during weakly disturbed times from Iijima and Potemra [1976]. Note that in Figure 9 field-aligned currents are observed at all magnetic local times and that the current sheets are oriented nearly along constant invariant latitude. In contrast, the intense auroral kilometric radiation is believed to be generated on the nightside between 19 and 01 hours magnetic local time (see region bounded by the crossed-hatched lines in Figure 9) and in the auroral zone near  $70^\circ$  invariant latitude.

Several characteristics distinguish the field-aligned currents in the local evening from those observed at other local times. In Figure 9 from 22 hours to 0 hour magnetic local time, on the average, a complicated system of current sheets exist being first into, then out of,

and finally poleward, a current sheet into the ionosphere. Zmuda and Armstrong [1974] believe that this complicated current system is a transition region between the two patterns of current flow in the dawn and dusk local times. In addition, the complicated current system illustrated in Figure 9 between 22 and 01 hours, in part, is believed to be associated with the intensification and intrusion of the westward electrojet into the evening sector [Iijima and Potemra, 1978]. The simultaneous observations of auroral kilometric radiation with field-aligned currents are selected from times when Hawkeye is in the AKR emission cone (see Section II) at radial distance  $\geq 7 R_E$  (to avoid local propagation cutoff effects) and when Triad is in the auroral oval from 19 to 01 hours magnetic local time in the northern hemisphere. The 19 to 01 hour magnetic local time region is where the most intense kilometric radiation is generated and the most complicated pattern of field-aligned currents are found.

### C. Qualitative Comparison Of Auroral Kilometric Radiation and Field-Aligned Currents

Between the period June, 1974, to August, 1975, there were 257 Triad auroral zone passes meeting the criterion outline in the previous section while Hawkeye was in the AKR emission cone. Some typical simultaneous measurements from Hawkeye and Triad are illustrated in Figure 10. The top panel of Figure 10 are electric field intensities in units of power flux at 178 kHz from the plasma wave instrument on board Hawkeye. All the radio emission above the

receiver noise level are attributed to auroral kilometric radiation. Simultaneous magnetic field observations made by the Triad spacecraft on four consecutive passes through the auroral zone in the northern hemisphere at about 23 hours magnetic local time are shown in the panels marked A, B, C, and D. The magnetic field measurements are from the A sensor on board Triad and are plotted in terms of  $\Delta B$  deviation from the baseline formed by  $B_M - B_T$ . The A panel illustrates that the Triad pass through the auroral zone shows little evidence of east-west field-aligned current sheets. The maximum deviation occurs at about 0816:30 UT with  $\Delta B \simeq 43\gamma$ . Simultaneously, the Hawkeye plasma wave experiment does not detect auroral kilometric radiation (see arrow labeled A in the top panel of Figure 10). Approximately ninety minutes later on the next pass through the auroral oval in the northern hemisphere the Triad magnetometer experiment revealed an extremely complicated system of east-west field-aligned current sheets which is a typical Triad observation in this magnetic local time sector (see Section III-B). The integrated current across the major current sheet (0957 to 0959 UT) of the Triad pass in the B panel is 0.52 Amps/m. Meanwhile, Hawkeye observed intense auroral kilometric radiation from its position in the emission cone of more than  $10^{-16}$  watts/(m<sup>2</sup>Hz) (see arrow labeled B in Figure 10). Panels C and D of Figure 10 also indicate complex east-west current sheets in the auroral oval as seen in these perturbations from the geomagnetic field. In both cases intense bursts of auroral kilometric radiation are detected by the Hawkeye plasma wave experiment simultaneously as pointed

to by the C and D arrows in the top panel of Figure 10. The integrated current intensity of the field-aligned current sheets at 1320 UT in panel D of Figure 10 is nearly 0.85 Amps/m while the AKR power flux, the largest observed for this time period was greater than  $10^{-14}$  watts/( $m^2 Hz$ ). Figure 10 is consistent with the idea that intense auroral zone field-aligned currents are correlated with intense bursts of auroral kilometric radiation.

#### D. Quantitative Analysis Of Auroral Kilometric Radiation and Field-Aligned Currents

To provide a quantitative evaluation of the relationship between auroral kilometric radiation and field-aligned currents, Figure 11 is a scatter plot of simultaneous three-minute average AKR power flux measurements at 178 kHz versus the integrated current intensity across the largest current sheets observed on each Triad pass. A three-minute average of the electric field measurements from Hawkeye takes into account any spin modulation effect and gives a power flux determination on a time scale comparable to the complete crossing of Triad across the auroral zone. To take into account the radial dependence of auroral kilometric radiation, a  $(R/7 R_E)^2$  normalization is applied to the average power flux measurements. The R variable is the distance from the satellite to the average source region of auroral kilometric radiation. The triangles in Figure 11 are the times when auroral kilometric radiation was not detected by Hawkeye above the receiver's noise level and thus represent an upper limit. A correlation can be

seen which is, as the AKR power flux increases so does the integrated current intensity increase. Statistically, the linear correlation coefficient of the log of the power flux versus the log of the integrated current intensity is 0.57. From Figure 11, when the AKR power flux was weak ( $< 10^{-18}$  watts/(m<sup>2</sup>Hz)) the integrated current intensity is less than 0.36 Amps/m while for integrated current intensities greater than 0.6 Amps/m the AKR power flux is moderately intense ( $10^{-15}$  to  $10^{-14}$  watts/(m<sup>2</sup>Hz)) to very intense ( $> 10^{-14}$  watts/(m<sup>2</sup>Hz)). The correlation in Figure 11 indicates that field-aligned currents may play an important role in the generation of auroral kilometric radiation, since the currents are always observed by Triad in the auroral zone when Hawkeye observes AKR (see Section V).

#### E. Possible Sources Of Scatter In the Correlation Between AKR and Field-Aligned Currents

Several sources of uncertainty and fluctuation could have contributed to the scatter in Figure 11 which we will presently discuss. The result of Section II shows that the scatter in Figure 11 due to the position of Hawkeye in the AKR emission cone is expected to be less than 10 db. Kaiser and Alexander [1977a] found that the peak in the emission spectrum of auroral kilometric radiation decreases with increasing AE. Since the 178-kHz channel on Hawkeye is near the average spectral peak, changes in the peak frequency could produce an increase in the observed power flux. The enhancement at 178 kHz due to this effect could produce a maximum increase of much less than

10 db. Probably the largest source of scatter in Figure 11 is due to using global (power flux) versus point (field-aligned currents) measurements. Triad on any given pass, cuts through the nighttime auroral oval at nearly constant local time and it is certain that Triad will not always observe the most intense part of the pre-midnight field-aligned current system. Hawkeye, however, from its position in the AKR emission cone observes an integrated power flux of auroral kilometric radiation from the entire evening active auroral region. Global versus point measurements could easily produce the scatter in Figure 11 since many intense bursts of auroral kilometric radiation ( $> 10^{-16}$  watts/(m<sup>2</sup>Hz)) would then be associated with relatively small field-aligned currents ( $< 0.3$  Amps/m), but there would be no cases of intense field-aligned currents ( $> 0.6$  Amps/m) associated with weak ( $< 10^{-17}$  watts/(m<sup>2</sup>Hz)) auroral kilometric bursts. The relatively low linear correlation coefficient (0.57) indicates that the correlation between auroral kilometric radiation and pre-midnight field-aligned currents is not particularly good. However, from the present discussion of the sources of scatter in Figure 11 it is obvious that many factors may have contributed to the determination of the low correlation coefficient.



#### IV. AN INVESTIGATION OF THE RELATIONSHIP BETWEEN AURORAL KILOMETRIC RADIATION AND AURORAL PARTICLE PRECIPITATION

##### A. Constraints On the AE-D and Hawkeye Observations

One of the most important questions which can be investigated by using simultaneous observations is what are the energies of the particles which can play a major role in the generation of auroral kilometric radiation. To determine such a particle distribution requires in situ observations of the precipitating auroral particles at relatively low altitudes in the region where the radiation is generated. Although its apogee was below the average source region of auroral kilometric radiation, the low altitude satellite, AE-D, examined in detail auroral particle precipitation during part of the time Hawkeye was in orbit. This section will study simultaneous observations of auroral kilometric radiation from Hawkeye and auroral particle precipitation as observed by AE-D.

AE-D was launched on October 6, 1975, into a polar orbit with initial apogee and perigee altitudes of 4,000 km and 150 km, respectively, and an inclination of 90°. During its brief 4-month lifetime, the Low Energy Electron (LEE) experiment measured electron fluxes in 16 energy channels ranging from 200 eV to 25 keV in a one-second instrument cycle. Each of the Low Energy Electron detectors has an acceptance angle of about 15° and an energy acceptance band ( $\Delta E/E$ ) of 30%.



Since auroral kilometric radiation is well correlated with the occurrence of discrete auroral arcs, it has been assumed that AKR must also be correlated with inverted-V electron precipitation because this type of auroral precipitation has been found to be associated with discrete arcs. Lin and Hoffman [1979] have shown that inverted-V electron precipitations observed by the LEE experiment on board AE-D are found at all local times not only in the auroral zone, but in the polar cap region as well. In contrast, as mentioned earlier, Gallagher and Gurnett [1979] and others have determined that the most intense bursts of auroral kilometric radiation originate from 22 to 24 hours magnetic local time in the auroral zone. There are, however, several characteristics which distinguish the inverted-V electron precipitations in the local evening (from about 19 to 01 hours magnetic local time) from those observed at other local times. Lin and Hoffman [1979] determined that the inverted-V events observed in the local evening are on the average much broader in invariant latitude and the characteristic peak energies of the events are on the average higher than those at other local times.

In order to insure that Hawkeye has the highest probability of observing auroral kilometric radiation, if it is being generated, the Hawkeye observations are again selected from the times when Hawkeye was in the AKR emission cone as discussed in Section II and at radial distances  $\geq 7 R_E$  to avoid local propagation cutoff effects. Only the AE-D observations from 19 to 01 hours magnetic local time will be used since this is the region where the most intense bursts

of auroral kilometric radiation are believed to originate and interestingly, the most energetic inverted-V events are observed. The simultaneous AKR power flux measurements and AE-D particle observations are taken from the times when both satellites were in the northern hemisphere.

B. Qualitative Comparison Of Auroral Kilometric  
Radiation and Auroral Particle Precipitation

During the 4 months that Hawkeye and AE-D were simultaneously in orbit there were 93 passes which met the criterion outlined in the previous section. Figure 12 is a qualitative comparison of some typical events. The top panel of Figure 12 shows the electric field intensities detected by Hawkeye at 178 kHz while it is in the AKR emission cone. All these enhanced radio emissions are attributed to auroral kilometric radiation. During this period of Hawkeye observations, AE-D transversed the nighttime auroral oval in the northern hemisphere on three consecutive passes. The energy-time spectrograms from the Low Energy Electron array of stepped detectors on AE-D are shown in the bottom three panels labeled orbits 698, 699, and 700. In the first two auroral passes, orbits 698 and 699, the AE-D spacecraft was in the de-spin mode where the spin period was one revolution per orbit. During these two passes, the stepped electron detectors had a view angle of  $-7^\circ$  to the radius vector and were looking at precipitating electrons with pitch angles of less than  $11^\circ$ . The bottom panel, orbit 700, corresponds to a period

when the AE-D spacecraft was in a spinning mode with a spin period of 15 seconds.

Inverted-V electron precipitation events are characterized by electron fluxes which increase from a few hundred eV to keV energies and then return to a few hundred eV energies as the spacecraft crosses this narrow band of auroral electron precipitation. This type of precipitation creates an inverted-V shaped intensity band in energy-time spectrograms [Frank and Ackerson, 1971]. On orbit 698 in Figure 12, the Low Energy Electron detectors on AE-D measured three energetic inverted-V electron precipitation events at 1102, 1102:15 and 1102:30 UT with peak energies of 1.9 keV, 1.38 keV and 13.1 keV. Approximately two hours later, on the next pass through the auroral oval in the northern hemisphere, the Low Energy Electron experiment measured at least two energetic inverted-V's with peak energies of 6.88 keV and 3.62 keV plus moderately intense electron plasma sheet precipitation. Simultaneously, the Hawkeye plasma wave experiment measured moderately intense bursts of auroral kilometric radiation at 178 kHz in excess of  $10^{-16}$  watts/(m<sup>2</sup>Hz) (see arrows labeled 698 and 699 in top panel of Figure 12). Much of the electron precipitation referred to here as plasma sheet precipitation has the same characteristics that Winningham et al. [1975] described as coming from the central plasma sheet region of the magnetotail and corresponds to regions of diffuse aurora. The plasma sheet precipitation has large electron fluxes at low energies extending in latitudinal width to as much as 10° and is quite easily distinguishable from inverted-V

events in the energy time spectrograms. On orbit 700, moderately intense electron plasma sheet precipitation is observed by AE-D while no evidence of inverted-V precipitation is found. The spin modulation of the electron fluxes in the bottom panel indicates the precipitating nature of these electrons. No auroral kilometric radiation is detected during the last AE-D auroral pass (arrow labeled 700) in Figure 12.

The results of the qualitative survey of simultaneous observations of auroral kilometric radiation and electron precipitation in the nighttime auroral oval are summarized in Table 1. The Hawkeye observations are classified according to whether or not auroral kilometric radiation is detected above the noise level of the plasma wave instrument. The electron measurements are classified according to all possible combinations of two basic types of electron precipitation patterns measured by AE-D in the nighttime auroral oval; inverted-V and plasma sheet precipitation. Energetic inverted-V precipitation and no plasma sheet precipitation (see the E-t spectrogram from orbit 698 in Figure 12 as an example) occurred on 15% of the simultaneous observations and Hawkeye always detected AKR at those times. During 49% of the auroral zone passes where AE-D observed inverted-V and electron plasma sheet precipitation (see the E-t spectrogram of orbit 699 as an example), Hawkeye detected auroral kilometric radiation. However, on two auroral passes (2% of the time) when AE-D observed energetic particle precipitation in the form of inverted-V and plasma sheet precipitation, Hawkeye did

not detect AKR. AE-D observed electron plasma sheet precipitation and no inverted-V precipitation on 25% of the simultaneous observations (see the orbit 700 E-t spectrogram in Figure 12 as an example) while Hawkeye did not observe auroral kilometric radiation above the receiver's noise level. The plasma sheet precipitation on seven of these AE-D auroral passes when Hawkeye did not detect AKR had intense energy fluxes  $> 10^8$  keV/(sec cm<sup>2</sup> ster) (comparable to the energy fluxes in many of the inverted-V events). In addition, by far the largest percentage of times for which Hawkeye did not detect AKR (column sum of 27%) occurred while AE-D was simultaneously observing electron plasma sheet precipitation and no inverted-V precipitation (25% of the time). This qualitative survey supports the conclusion of Gurnett [1974] that auroral kilometric radiation is more closely associated with inverted-V electron precipitation than with plasma sheet precipitation in the nighttime auroral zone.

If auroral kilometric radiation is generated by precipitating inverted-V electrons, then an explanation must be sought for the cases in which AKR was detected when AE-D observed plasma sheet precipitation and no inverted-V precipitation (9% of the time). Quite obviously the AE-D detectors do not survey the nature of the particle precipitation over the entire pre-midnight active auroral region in one pass. Since the precipitation pattern of inverted-V events, like discrete auroral arcs, does vary considerably in local time it is reasonable to assume that inverted-V structures could be missed.

### C. Quantitative Analysis Of Auroral Kilometric

#### Radiation and Inverted-V Events

It is of importance to explore more quantitatively any relationship between auroral kilometric radiation and energetic inverted-V electron precipitation if indeed these particles are the ultimate source of energy for this electromagnetic radiation. If auroral kilometric radiation and inverted-V events are correlated, as suggested by Figure 12 and Table 1, then it is reasonable to expect that as the energy in the inverted-V events increases, so might the intensity of the kilometric radiation. Figure 13 is a scatter plot of simultaneous three-minute average AKR power flux measurements at 178 kHz versus the inverted-V peak energy which is used here to characterize the particle energy in the event. A three-minute averaged power flux measurement takes into account any spin modulation effect and gives an electric field measurement on a time scale comparable with the complete crossing of AE-D across the auroral oval. A  $(R/7 R_E)^2$  normalization is again applied to the average power flux measurements to take into account the radial dependence of this radiation. The variable R is the distance from the satellite to the average source region (see Section II) of the most intense bursts of AKR. The two triangles represent the minimum detectable signals by Hawkeye since no AKR was detected at those times. During AE-D passes where several inverted-V events were observed, only the event with the largest peak energy is plotted. The peak energy is the center energy

of the channel where the peak particle flux associated with the inverted-V event is observed. There appears to be an obvious relationship between these two parameters, that is, as the AKR power flux measurements increase so does the characteristic peak energy of the precipitating inverted-V. Statistically, the linear correlation coefficient of the log (power flux) versus the peak energy is 0.65.

An examination of the distribution functions at  $\sim 0^\circ$  pitch angle at the time of the peak in the inverted-V events used in Figure 13 reveal striking differences when ordered by increasing magnitude of the simultaneous power flux observations of auroral kilometric radiation. The distribution function at  $0^\circ$  pitch angle ( $\pm 7\frac{1}{2}^\circ$ ) is the most field-aligned part assuring us of examining electrons of magnetospheric origin which have been presumably accelerated down to AE-D altitudes and possibly through the AKR source region (see Section V-B). Figure 14 shows three representative electron distribution functions when Hawkeye observed weak (top panel), moderate (center panel), and intense (bottom panel) auroral kilometric radiation in the AKR emission cone. The actual power flux measurements associated with the AE-D observations of Figure 14 are given in the upper right corner of each panel. The electron distribution functions  $F(V_{||})$  of Figure 14 are calculated from the observed differential fluxes  $J$  at energies  $E$  by

$$F(V_{||}) = \frac{m_e^2}{2} \frac{J}{E} = 1.616 \times 10^{-7} \frac{J}{E} \quad (4)$$



with

$$F(V_{\parallel}) \text{ in electrons sec}^3/\text{km}^6 \quad ,$$

$$J \text{ in } \frac{\text{electrons}}{\text{cm}^2 \text{ sec ster keV}} \text{ (at } 0 \pm 7 \frac{1}{2}^\circ \text{ pitch angle) } ,$$

$$E \text{ in keV} \quad ,$$

$$m_e \text{ equals the electron mass in kg} \quad .$$

A major difference between the distribution functions in Figure 14, as suggested by Figure 13, is that the peak in each inverted-V event increases as the AKR power flux associated with the event increases. The peaks of the inverted-V events in the top, center, and bottom panels occur at parallel velocities of about  $3 \times 10^4$ ,  $4 \times 10^4$ , and  $6.7 \times 10^4$  km/sec, respectively. In general, for the times when Hawkeye observes weak auroral kilometric radiation  $< 10^{-17}$  watts/( $\text{m}^2 \text{ Hz}$ ) (normalized to  $7 R_E$ ) the peaks of the inverted-V events observed by AE-D have values of  $F(V_{\parallel})$  that range from 1.0 electron  $\text{sec}^3/\text{km}^6$  to as high as 40 electrons  $\text{sec}^3/\text{km}^6$  and are easily distinguishable in the  $F(V_{\parallel})$  distributions (see for example top panel of Figure 14). In contrast, when Hawkeye observes very intense auroral



kilometric radiation  $> 10^{-14}$  watts/(m<sup>2</sup>Hz) (normalized to  $7 R_E$ ) the value of  $F(V_{||})$  at the peak of the inverted-V events range from 0.1 to 4.0 electrons sec<sup>3</sup>/km<sup>6</sup> with the peaks almost indistinguishable from a plateau-like structure in these distribution functions. A plateau or horizontal flattening in  $F(V_{||})$  at large velocities (see for example the bottom panel in Figure 14 from  $2 \times 10^4$  to  $6 \times 10^4$  km/sec) is a common feature for the distribution functions associated with power fluxes of auroral kilometric radiation  $> 10^{-15}$  watts/(m<sup>2</sup>Hz) (normalized to  $7 R_E$ ). The slope of the plateau or tail in the distribution functions can be quantitatively determined by calculating an effective tail temperature given by

$$T_{||} = \frac{m_e}{k_B} \frac{\int_{V_A}^{V_B} V_{||}^2 F(V_{||}) dV_{||}}{N} \quad (5)$$

where

$k_B$  equals Boltzmann's constant,

$V_A$  equals  $4 \times 10^4$  km/sec,

$V_B$  equals  $8 \times 10^4$  km/sec, and

$$N = \text{density} = \int_{V_A}^{V_B} F(V_{||}) dV_{||} \quad .$$

The quantity  $T_{||}$  is an effective temperature since calculation of the temperature requires knowledge of the distribution function at all

velocities plus knowledge of any streaming in the distribution. Figure 15 is a scatter plot of the power flux measurements of auroral kilometric radiation versus the effective tail temperature  $T_{||}$  in the distribution functions at  $\sim 0^\circ$  pitch angle of the inverted-V events simultaneously observed by AE-D. The integration limits for calculating  $T_{||}$  are determined such that at the high velocity (very high energy) limit the observed fluxes for all the inverted-V events are above the threshold of the LEE detectors and the lower velocity (low energy) limit is above major inverted-V peaks in the distribution functions. The correlation coefficient in Figure 15 between the log of the power flux and the effective tail temperature ( $T_{||}$ ) is 0.49. Even though this is a relatively low linear correlation coefficient when the AKR power flux is weak ( $< 10^{-17}$  watts/(m<sup>2</sup>Hz))  $T_{||}$  is less than  $1.8 \times 10^8$  °K while for  $T_{||}$  greater than  $1.8 \times 10^8$  °K the associated AKR power flux is moderate ( $10^{-17}$  to  $10^{-15}$  watts/(m<sup>2</sup>Hz)) to intense ( $> 10^{-15}$  watts/(m<sup>2</sup>Hz)).

Figure 16 is a scatter plot of three-minute average AKR power flux measurements versus the energy flux at the time of the peak in precipitating inverted-V events used in Figures 13 and 15. The energy flux (EF) is determined from numerically integrating the energy (E) of the precipitating electrons times the differential flux (J) at that energy over the energy range of the Low Energy Electron detectors (200 eV to 25 keV).

$$EF = \int_{0.2 \text{ keV}}^{25 \text{ keV}} EJdE \quad (6)$$

The additional vertical scale in Figure 16 (right hand side) is for the corresponding AKR total power output derived from the Hawkeye power flux measurements (PF) and from previous knowledge of the time-averaged AKR bandwidth (BW) of 200 kHz [Kaiser and Alexander, 1977a] and the angular distribution of 3.5 steradians ( $\Omega$ ) [Green et al., 1977].

$$\text{Power}_{\text{AKR}}(\text{watts}) = \text{PF} \left( \frac{\text{watts}}{\text{m}^2 \text{Hz}} \right) * A(\text{m}^2) * \text{BW}(\text{Hz})$$

where

$$A = \Omega r^2$$

and

$$r = 7 R_E \text{ (radius at with PF normalized to)}$$

The top scale is the amount of total power in the precipitating inverted-V events (not counting plasma sheet precipitation) and is derived from the actual measured particle fluxes and assumed average latitudinal width of  $1.5^\circ$  for these events as recently reported by Lin and Hoffman [1979] and an estimated longitudinal width of  $75^\circ$

which is a typical longitudinal extent of a discrete auroral arc.

$$\text{Power}_{\text{IN-V}}(\text{watts}) = EF \left( \frac{\text{keV}}{\text{sec cm}^2 \text{ster}} \right) * \pi(\text{ster}) * A(\text{cm}^2) * C \frac{\text{joules}}{\text{keV}}$$

where

$$\pi = \int_0^{2\pi} d\phi \int_0^{\pi/2} \sin\alpha d\alpha$$

(integration over the precipitating part of the electron distribution with pitch angle  $\alpha$ )

$$A = \Omega r^2$$

$\Omega$  is the assumed solid angle extent of the inverted-V events.

$r$  is the average geocentric radial distance to inverted-V events observed.

$$C = 1.602 \times 10^{-16} \frac{\text{joules}}{\text{keV}} \text{ (unit conversion) } .$$

The far right vertical scale and the top horizontal scale are only used as rough estimates of the auroral kilometric radiation and charged particle power in these events since simultaneous measurements of all the parameters necessary to determine these values is not possible.

An important feature of Figure 16 is that if inverted-V precipitation is the ultimate energy source, the efficiency of converting the charge particle energy into electromagnetic radiation increases to a maximum of about 1% for the most intense AKR bursts. This result is in excellent agreement with earlier estimates. As Figure 16 illustrates, however, a 1% efficiency occurs in only a few percent of the cases. The median of the distribution in Figure 16 is at about 0.001% efficiency with the lowest conversion efficiency near  $10^{-5}\%$ .

In Figure 16 inverted-V events with large energy fluxes  $\approx 10^{10}$  keV/(sec cm<sup>2</sup> ster) have characteristic peak energies ranging from 2.62 keV to 24.9 keV, but the most intense bursts of AKR are associated with inverted-V events which have peak energies  $\geq 7$  keV. This indicates that even though there may be  $\geq 10^{10}$  watts of power in a precipitating inverted-V event it is not necessarily true that at the same time there will be intense kilometric radiation. It is then reasonable to assume that the generation of AKR may be very sensitive to other plasma parameters in the source region and special anisotropies in the distribution function of the precipitating particles.

Figure 15 suggests that the tail temperature  $T_{||}$  of  $F(V_{||})$  may be a special feature of the distribution function needed for the efficient generation or amplification of auroral kilometric radiation. Many of the inverted-V events that are associated with weak-to-moderate AKR ( $< 10^{-16}$  watts/(m<sup>2</sup>Hz)) have large energy fluxes (from  $10^9$  to  $10^{10}$  keV/(sec cm<sup>2</sup> ster) of Figure 16) because they are observed to have very large differential fluxes at low energies and very small differential

fluxes at high energies (small  $T_{||}$ ). The inverted-V events that are associated with intense AKR ( $> 10^{-14}$  watts/(m<sup>2</sup>Hz)) have relatively small differential fluxes at low energies but moderately large fluxes at high energies (large  $T_{||}$ ). To illustrate this effect on the calculation of the energy flux, Figure 17 is a similar scatter plot to Figure 16 except the lower limit of integration has been changed from 0.2 keV (as in Figure 16) to 6.88 keV. The inverted-V events in Figure 17 with energy fluxes less than  $10^8$  keV/(sec cm<sup>2</sup> ster) had comparatively small tail temperatures and are associated with weak-to-moderate auroral kilometric radiation ( $< 10^{-15}$  watts/(m<sup>2</sup>Hz)). In contrast, these data in Figure 17 had energy fluxes greater than  $10^8$  keV/(sec cm<sup>2</sup> ster) illustrating that these inverted-V events were observed to have high electron differential fluxes at low energies ( $< 6.88$  keV). In addition, the most intense bursts of auroral kilometric radiation ( $> 10^{-14}$  watts/(m<sup>2</sup>Hz)) in Figure 16 and Figure 17 were associated with inverted-V events with energy fluxes greater than  $10^9$  keV/(sec cm<sup>2</sup> ster) illustrating that these inverted-V events had large electron differential fluxes in the tail of  $F(V_{||})$  and comparatively large  $T_{||}$ . If the tail of the distribution function  $F(V_{||})$  of inverted-V events is important for the amplification of auroral kilometric radiation through, for example, a possible resonance interaction, then Figure 17 illustrates that in many cases efficiencies as high as 0.1 to 1% may be possible for a dynamic range in AKR intensity as large as 40 db. Since there are some data points in Figure 17 which show that weak AKR bursts are associated with intense particle precipitations and

large differential fluxes at high energies in the tail of  $F(V_{||})$ , the efficient generation of kilometric radiation, in these cases, may still be sensitive to other plasma parameters besides the tail temperature.

#### D. Possible Sources Of Scatter In the Correlation

##### Between AKR and Inverted-V Events

As discussed in Sections II and III-E, the scatter in Figure 13 (also in Figures 15 and 16) due to the position of Hawkeye in the AKR emission cone is expected to be less than 10 db. In addition, scatter due to changes in the AKR spectrum is also estimated as less than an order of magnitude. If the source region of an auroral kilometric storm was different than the average source position used in the  $(R/7 R_E)^2$  normalization to the intensity then this would contribute to the scatter. Any difference in actual source position from the average source used in this thesis would introduce a relatively small scatter of a few db if the AKR source remained in the nighttime auroral zone. Changes in the electron distribution due to the mirroring effect is greatly reduced by using particle observations at  $\sim 0^\circ$  pitch angle ( $\pm 7 1/2^\circ$ ) and, therefore, is not considered to be a large source of uncertainty. It is probable that the largest source of scatter in Figures 13, 15, and 16 is due once again to plotting global (power flux) versus point (inverted-V peak) measurements. Since AE-D cuts through the nighttime auroral oval at nearly constant local time, it is certain that AE-D will not always observe the most intense part of the electron precipitation pattern.

Thus, the correlation between auroral kilometric radiation and the peak energies of the precipitating inverted-V events at  $\sim 0^\circ$  pitch angle as shown in Figure 13 is relatively good despite the problems outlined above.



V. INTERPRETATION AND DISCUSSION OF THE SIMULTANEOUS  
OBSERVATIONS OF AURORAL KILOMETRIC RADIATION  
AND AURORAL PARTICLE PRECIPITATION

A. Possible Role Of Field-Aligned Currents In the  
Generation and Amplification Of AKR

It is important to speculate on the role which field-aligned currents might play in the generation and possible amplification of auroral kilometric radiation as suggested by Figure 11. One direct relationship is that field-aligned currents are probably bringing into the AKR source region the particles or current whose energy, at least in part, is converted into the kilometric radiation. Increases in the integrated current intensities of field-aligned currents may be due to progressively larger and larger particle fluxes at progressively higher velocities. As indicated in Figure 13, increases of the peak energy of inverted-V events (large fluxes at progressively higher energies velocities) are associated with increases in the AKR power flux within the emission cone. Since Triad does not have a particle experiment on-board, the energies and fluxes of the actual precipitating magnetospheric particles and upgoing (out of the ionosphere) ionospheric particles making up the field-aligned currents observed are not known. There are only a few examples of the simultaneous observation of field-aligned currents and particle measurements in the literature. The

basic result from these studies (see, for example, Casserly and Cloutier [1975]) is that the particle fluxes, in the energy range of the particle detectors flown, (typically 0.5 to  $> 20$  keV) usually account for only 20% or less of the inferred current deduced from the accompanying magnetometer data. This result implies that the majority of the current carriers are particles at low energies ( $< 0.5$  keV). Figure 17 suggests that the precipitating tail of inverted-V electron distributions are important for the efficient generation of auroral kilometric radiation. The current carried by the precipitating tail (particle energies  $\geq 5$  keV) of the inverted-V distributions used in this study ranges from a maximum of 46% to a minimum of less than 0.1% of the current in the observed precipitating ( $\sim 0^\circ$  pitch angle) electron distribution. Since the current in the observed distribution may be  $\leq 20\%$  of the total auroral zone field-aligned current (deduced from magnetometer measurements) then the current in the high energy inverted-V tail can at best comprise less than 10% of the total current. This effect may help explain why the inverted-V correlation (see Figure 13) is relatively good and the field-aligned current correlation (see Figure 11), in comparison, is not as good.

If the majority of the field-aligned currents observed by Triad are carried by low energy particles then the correlation between AKR and field-aligned currents as shown in Figure 11 may also indicate more of an indirect relationship. For example, current instabilities producing low frequency wave turbulence, such as electrostatic ion cyclotron waves or ion acoustic waves in the auroral zone, have been postulated by

Kindel and Kennel [1971]. Kintner et al. [1978] have observed intense electrostatic ion cyclotron waves ( $\sim 25$  mV/m at 115 Hz) with the S3-3 spacecraft near 20 hours magnetic local time at an altitude of over 6,000 kilometers in the auroral zone and found them to be consistent with the current driven model proposed by Kindel and Kennel [1971]. Ion heating due to electrostatic ion cyclotron turbulence has been shown theoretically by Palmadesso et al. [1974] to produce anomalous resistivity and, thus, field-aligned potential drops. Field-aligned potential drops or parallel electric fields are generally believed to be responsible for the formation and acceleration of inverted-V electron precipitation events which may be in some way responsible for the generation or amplification of auroral kilometric radiation (see Figure 13). Figure 11 may be illustrating that increasing field-aligned current intensity increases the growth of the electrostatic ion cyclotron waves enhancing anomalous resistivity which leads to larger field-aligned potential drops and the production of auroral kilometric radiation. This is a rather idealized interpretation since the process of producing field-aligned potential drops from anomalous resistivity is not related simply to the current intensity. Double layer and electrostatic shocks, which also produce field-aligned potential drop can be established by a current above a certain threshold. However, the magnitude of the field-aligned potential drop (for inverted-V acceleration) in a double layer or electrostatic shock is determined not from the intensity of the current but from the external generator such as the magnetospheric tail (see for example the review by Goertz [1979]).

From these general considerations of accelerating mechanisms it is clear that the relationship between AKR with field-aligned currents and inverted-V events may be extremely complicated.

There are, in addition to the quantitative results of Figure 11, qualitative features of auroral kilometric radiation and field-aligned currents which deserve mention. The conditions which lead to the generation of auroral kilometric radiation must be easily met since, when Hawkeye is in the AKR emission cone, auroral kilometric radiation is detected above the receiver noise level nearly 90% of the time. Similarly, Triad observes field-aligned currents as a nearly permanent feature of the auroral zone. As easily seen in panels B, C, and D of Figure 10, either much structure exists in the separate current sheets or rapid temporal variations in field-aligned currents exist on a time scale of seconds or both. The question of whether field-aligned currents exhibit rapid temporal fluctuations or have fine structured current sheets within current sheets cannot be discerned with the single Triad spacecraft. It is interesting to note, however, that one basic characteristic of auroral kilometric radiation is that rapid fluctuations in the intensity of this radiation, like field-aligned currents, exists on a time scale of seconds and even less than a second (see Gurnett et al. [1979]).

In summary, Figure 11 illustrates quantitatively that field-aligned currents in the pre-midnight auroral zone are correlated with auroral kilometric radiation such that as the log of the AKR power

flux increases, so does the log of the integrated current intensity increase. It is suggested that field-aligned currents may play not only a direct role in the generation of AKR, but possibly also an indirect one with the development of parallel electric fields that produce inverted-V electron precipitation which has also been associated with auroral kilometric radiation. It is clear that the exact relationship between AKR and field-aligned auroral currents is far from being understood and that much work is needed in this area.

#### B. Possible Role Of Inverted-V Electron Precipitation

##### In the Generation and Amplification Of AKR

It is important to note that Figure 17 is very similar to the correlation of AKR intensity with the AE index shown in Figure 3. AE is directly proportional to the auroral electrojet current and is believed to be fed by field-aligned currents flowing into and out of the ionosphere in the auroral zones. Figure 3 shows that during times of large excursions of the AE index ( $\sim 1000\gamma$ ) a large range of intensities of AKR have been observed (from  $10^{-20}$  to  $10^{-14}$  watts/( $m^2 Hz$ ) normalized to  $30 R_E$ ). However, for times when AE index is below  $158\gamma$  68.7% of the power flux measurements are below  $6.31 \times 10^{-19}$  watts/( $m^2 Hz$ ). Figure 17 in a similar way illustrates that at times when large amounts of power are present in precipitating inverted-V events there is a large range in the observed intensity of AKR bursts (from  $10^{-18}$  to  $10^{-13}$  watts/( $m^2 Hz$ ) normalized to  $7 R_E$ ). Inverted-V events with peak energies  $\sim 7$  keV and with energy fluxes

$> 10^9$  keV/(sec cm<sup>2</sup> ster) are associated with the most intense bursts of auroral kilometric radiation. Figure 17 and Figure 3 suggest that it is not sufficient to have large amounts of power available in the charged particles precipitating in the auroral zone for the simultaneous production of intense auroral kilometric radiation, but in addition to the power requirements, special features or anisotropies in the particle distribution function or in the plasma parameters in the source region are needed for the instability to obtain high efficiencies. A determination of these other important features in auroral zone plasmas may have to wait until the launch of Dynamics Explorer in 1981, since this spacecraft may be able to make simultaneous observations of AKR and particle distributions in the source region of auroral kilometric radiation.

The result of correlating AKR with auroral particle precipitation is that auroral kilometric radiation is more closely associated with inverted-V electron precipitation than with plasma sheet precipitation. It is found that as the observed AKR power flux increases, so does the simultaneously observed peak energy in inverted-V electron precipitation events increase. In addition, there is evidence that suggests that the efficiency of generating auroral kilometric radiation from inverted-V particle precipitation ranges from  $10^{-5}\%$  to a maximum efficiency of about 1%. Any realistic theory on the generation of auroral kilometric radiation must account for such a wide range in efficiencies.



VI. HAWKEYE PLASMA WAVE OBSERVATIONS OF  
 AURORAL KILOMETRIC RADIATION AT LOW  
 ALTITUDES IN THE AURORAL ZONE

A. The Observed Low Frequency Cutoff Of AKR At the  
 Local Electron Gyrofrequency

The initial perigee of the Hawkeye spacecraft after launch was 6,847 km geocentric radial distance in the southern hemisphere. The initial argument of perigee was  $274.6^\circ$  (so that apogee was almost directly over the north pole), but due to orbital perturbations, within two to three years the argument of perigee decreased to less than  $250^\circ$  and perigee increased to near 11,000 km. These changes enabled Hawkeye to cross auroral field lines at geocentric radial distances greater than 13,000 km ( $\geq 2.0 R_E$ ) in the region where auroral kilometric radiation is believed to be generated.

A typical example of auroral kilometric radiation observed by Hawkeye in the auroral zone of the southern hemisphere is shown in Figure 18 (from Gurnett and Green [1978]). The dashed line labeled  $f_g^-$  is the local electron gyrofrequency calculated from measurements made by the onboard triaxial fluxgate magnetometer which measured the ambient magnetic field in the southern hemisphere to  $\pm 125\gamma$  on each axis. The dashed line labeled  $f_p^-$  is an estimate of the local electron plasma frequency determined by the low frequency cutoff

of continuum radiation and the high frequency cutoff of auroral hiss. It has been well established in other regions of the magnetosphere by Gurnett and Shaw [1973] and Gurnett and Frank [1974] that the low frequency cutoff of the left-hand ordinary polarized (L-O) component of continuum radiation can be used as a reliable (at times within  $\pm 1\%$ ) indicator of the local electron plasma frequency. Both  $f_g^-$  and  $f_p^-$  are plotted over the electric field intensities on a frequency versus time scale where the frequency scale at the baseline of each channel is that channel's frequency. Thus, at 0312 UT in Figure 17,  $f_g^- = 178$  kHz and  $f_p^- = 39$  kHz. Note that in Figure 18 auroral kilometric radiation is observed only in regions where the local electron gyrofrequency and local electron plasma frequency are below the wave frequency (178 kHz in this case). A general feature of all the Hawkeye AKR southern hemisphere observations is that no intense auroral kilometric radiation is observed at radial distances below the level where the wave frequency is less than the local electron gyrofrequency. In addition, auroral kilometric radiation was only observed at low altitudes ( $2.0 - 2.5 R_E$ ) on the nightside from 18 to 06 hours magnetic local time.

The low frequency cutoff of auroral kilometric radiation at the local electron gyrofrequency is further illustrated in Figure 19. This figure is a scatter plot of Hawkeye southern hemisphere electric field measurements (over 225 passes) from 18 to 06 hours magnetic local time at 178 kHz plotted as a function of the ratio of the wave frequency to the local electron gyrofrequency ( $f/f_g^-$ ).



To clearly illustrate the cutoff of AKR at  $f_g^-$  passes for which intense auroral hiss emissions at 178 kHz occurred were eliminated. Virtually all the data below  $10^{-16}$  watts/(m<sup>2</sup>Hz) is continuum radiation which is observed not only in regions where the wave frequency is above, but also below the local electron gyrofrequency. This figure shows a sharp cutoff of at least five orders of magnitude in the AKR power flux at the local electron gyrofrequency.

The maximum measured electric field strength of auroral kilometric radiation in Figure 19 occurs where  $f \simeq f_g^-$  and is nearly 12 mV/m. Since Hawkeye does not have the capability of detecting any magnetic component associated with the electric field observations at 178 kHz, it is not known what fraction (if any) of the 12 mV/m fields observed in or near the AKR source region are electrostatic. Note also that the large electric fields in Figure 19 correspond to power fluxes greater than  $10^{-11}$  watts/(m<sup>2</sup>Hz). In order to estimate what fraction of the large ( $\simeq 10$  mV/m) electric fields in Figure 19 is electrostatic it is instructive to compare the observed power fluxes with previous measurements of intense AKR bursts observed far from the earth. Using a  $1/R^2$  extrapolation, escaping electromagnetic radiation with an intensity of  $10^{-11}$  watts/(m<sup>2</sup>Hz) generated at low altitudes would be observed far from the source ( $7 R_E$ ) with an intensity of  $\sim 10^{-13}$  watts/(m<sup>2</sup>Hz) which is in excellent agreement with the maximum intensity of AKR bursts found in this study (see Figures 11, 13, 15 or 16). This close agreement provides additional evidence of the low altitude ( $\sim 2.5 R_E$ ) origin of auroral kilometric radiation,

but more importantly illustrates that large electrostatic fields are not found in association with AKR in the auroral region sampled by Hawkeye.

## B. Interpretation Of the Low Frequency Cutoff

### As a Propagation Effect

An interpretation of the observed low frequency cutoff of auroral kilometric radiation as discussed by Gurnett and Green [1978] is illustrated in Figure 20 (taken from that paper). This figure shows the expected radial variations of the cutoff frequencies  $f_p^-$  and  $f_{R=0}$  for the left hand (L-O) and right hand (R-X) polarized modes of propagation respectively, along a  $70^\circ$  invariant latitude auroral field line. The local electron plasma frequency ( $f_p^-$ ) is qualitatively consistent with the plasma density observations made below 10,000 km by Isis I (see Benson and Calvert [1979]), near 14,000 km by S3-3 (see Tobert et al. [1979]), and from the low frequency cutoff of continuum radiation observed by Hawkeye between 14,000 to 16,000 km geocentric radial distance. The cutoff frequency for the R-X mode ( $f_{R=0}$ ) is calculated from the cold plasma formulation by Stix [1962] and involves knowledge of  $f_p^-$  and  $f_g^-$ ;

$$f_{R=0} = \frac{f_g^-}{2} + \left[ \left( \frac{f_g^-}{2} \right)^2 + (f_p^-)^2 \right]^{1/2} .$$

Under low density conditions the  $f_{R=0}$  cutoff for R-X mode radiation is nearly equal to the local electron gyrofrequency which is in the frequency range from about 50 kHz to 500 kHz in Figure 20. As illustrated

in the upper right corner of Figure 20, if either R-X or L-O mode radiation is generated above both the local electron plasma frequency and the  $f_{R=0}$  cutoff, only the R-X mode would not be able to penetrate into regions below the  $f_{R=0}$  cutoff, or below the local electron gyrofrequency. Since  $f_g^- \simeq f_{R=0}$ , the observed cutoff at  $f_g^-$  provides strong evidence that auroral kilometric radiation is propagating in the right-hand (R-X) polarized mode. Recent direct polarization measurements made by Voyagers 1 and 2 (see Kaiser et al. [1978]) indicate that the degree to which AKR is right-hand polarized (in the plasma convention) may be as high as 95%.

VII. COMPARISON OF THE CHARACTERISTICS OF AKR  
PRESENTED IN THIS STUDY WITH  
PROPOSED GENERATION MECHANISMS

A. Introduction

A brief summary of basic characteristics of all the proposed generation mechanisms for auroral kilometric radiation is given in Table II. As can easily be seen, a wide variety of processes have been proposed which produce electromagnetic radiation into not only purely the R-X or L-O polarization modes, but also a mixture of these free space or escaping modes. The term escaping radiation is used here to characterize radiation which can propagate into regions where its wave frequency is much greater than the local characteristic frequencies of the plasma ( $f_g^-$  or  $f_p^-$ ). The results of Section VI provide strong evidence that auroral kilometric radiation is propagating in the R-X mode. As mentioned earlier, Kaiser et al. [1978] measured the degree of right-hand (in the plasma convention) polarization of AKR emission from Voyagers I and II to reach at least 95%. In view of these findings only generation mechanisms which produce electromagnetic radiation in the R-X mode will be discussed in any detail and compared with other findings of this study.

Most of the theories listed in Table II rely on coupling mechanisms to eventually produce auroral kilometric radiation from electrostatic

waves at the upper hybrid resonance frequency,  $f_{\text{UHR}}$ , where (see Stix [1962])

$$f_{\text{UHR}} = (f_p^-)^2 + (f_g^-)^2 \quad 1/2 \quad (8)$$

According to the generation mechanism proposed by Barbosa [1976] (based on linear theory) electrostatic waves with amplitudes from 1 to 3 volts/m at the  $f_{\text{UHR}}$  are needed. Roux and Pellat [1979] propose that the generation of AKR from 100 mV/m electrostatic waves at  $f_{\text{UHR}}$  and  $f_{\text{LHR}}$  (lower hybrid resonance frequency) is possible from non-linear wave-wave interactions. From Equation 8  $f_g^- < f_{\text{UHR}} < f_{R=0}$  and when  $f_g^- \gg f_p^-$  then  $f_{\text{UHR}} \simeq f_g^-$ . As discussed in Section VI the condition  $f_g^- \simeq f_{R=0}$  appears to be a general feature in the high altitude auroral zone (see Figure 20). Thus, the assumption that  $f_{\text{UHR}} \simeq f_g^-$  is believed to be valid in the AKR source region. The large electric fields of  $\simeq 12$  mV/m attributed to auroral kilometric radiation in Figure 19 that are measured by Hawkeye in auroral regions where the wave frequency is greater than the local electron gyrofrequency could conceivably be  $f_{\text{UHR}}$  waves. However, the radiation intensity of these waves are consistent with the electric fields being almost completely electromagnetic in nature and not electrostatic. Another coupling mechanism proposed by Jones [1977a and 1977b] uses a wave-wave interaction from two low frequency electromagnetic Z mode waves to produce auroral kilometric radiation. The Z mode radiation is in a trapped propagation mode (not able to escape) and exists at frequencies below  $f_{\text{UHR}}$ . The generation

of auroral kilometric radiation from a mode coupling mechanism is what is generally described as an indirect process involving one or more steps. The overall efficiency of any indirect mechanism is the product of the efficiencies of each of the intermediate steps. As illustrated in Figures 16 and 17, a maximum efficiency of 1% may be obtained from precipitating inverted-V electrons. From the present knowledge of magnetospheric radio emissions the conversion of charged particle power directly into electromagnetic radiation with an overall conversion efficiency of 1% is an extremely efficient process [Gurnett, 1974]. Thus, the absence in the observations of large electrostatic fields at  $f_{UHR} (\approx f_g^-)$  in or near the average AKR source region plus the large conversion efficiencies which are needed in indirect processes to obtain the observed 1% efficiencies puts serious doubts upon the validity of those generation mechanisms which require the intermediate generation of electrostatic waves (see Table II).

The two remaining generation mechanisms in Table II which produce R-X mode electromagnetic radiation in a direct process are the amplified doppler shifted gyroemission proposed by Melrose [1976] and the relativistic normal cyclotron resonance amplification mechanism of Wu and Lee [1979]. The basic properties of these two mechanisms will be discussed and additional comparisons will be made in the remaining part of this thesis between these direct mechanisms and the results of this study.

The energy of auroral kilometric radiation must come from sources of free energy manifested in either configuration space (density gradients, etc.) or in velocity space (nonthermal features in the particle distributions). The existence and nature of any plasma instability is determined by the form of the free energy. The direct mechanisms of Melrose [1976], and Wu and Lee [1979] are both microinstabilities where the source of free energy is in the electron distribution functions. Both theories use analytic expressions for the electron distribution function which are believed to be representative of the high altitude (1 to 3  $R_E$ ) auroral zone plasmas. The distributions in which free energy is available, in actual auroral zone plasmas, can be examined by AE-D during passes in which it was in the spinning mode. Thus, it may be possible to determine qualitatively if sufficient free energy is available to drive the proposed direct mechanisms.

B. Review Of the Theory Of Amplified Doppler Shifted  
Gyroemission As a Mechanism For the Generation  
and Amplification Of AKR

In the theory of amplified doppler shifted gyroemission the source of free energy driving the instability exists in the descending or precipitating part of the electron distribution function as a supra-thermal beam. The high velocity precipitating beam initially produces escaping doppler shifted gyroemission above the  $f_{R=0}$  cutoff. In order that gyroemission can occur the doppler shift condition must be satisfied,

$$f = \frac{f_g^-}{\gamma(1 - \mu\beta\cos\alpha\cos\theta)} \quad (9)$$

where

$$\gamma = (1 - \beta^2)^{-1/2}$$

$$\beta = v/c$$

$\mu$  is the refractive index

$\alpha$  is the pitch angle

$\theta$  is the wave normal angle (angle between propagation vector  $\vec{k}$  and the geomagnetic field)

$f$  = wave frequency .

The moment of the beam speed  $\beta_s (= v_s/c)$  is  $\langle\beta\cos\alpha\rangle$  and with  $\gamma = 1$  (for discussion purposes) then

$$f \simeq f_g^-(1 + \mu\beta_s\cos\theta) \quad .$$

For escaping R-X mode radiation  $f > f_{R=0} > f_g^-$  then

$$\mu\beta_s\cos\theta > 0 \quad (10)$$

where



$\beta_s$  has been observed to be as large as 0.33 (making  $\gamma = 1.06$ ) but more typically  $\beta_s \approx 0.17$

$\mu$  must be  $\gg 1$ .

The growth rate for the amplification of the doppler shifted gyro-emission as determined by Melrose (see below) is insensitive to wave normal angles  $\theta \leq |60^\circ|$  (see bottom panel of Figure 23). In other words, escaping radiation must be emitted entirely in the forward direction.

Since the total power output of auroral kilometric radiation has been estimated to be as high as  $10^9$  watts [Gurnett, 1974] it is widely held that the actual generation mechanism must be based on a coherent process. Coherent, as used here, means that incoherent emission from particles radiating independently is not applicable and some sort of amplification or collective process is taking place. The type of collective process in Melrose's mechanism is from a negative absorption or amplification of the doppler shift emission by the precipitating electron distribution function. The form of the distribution function which Melrose uses is

$$F(\beta, \alpha) = \frac{1}{(2\pi)^{3/2}} \frac{1}{\beta_{\perp 0}^2 \beta_{\parallel 0}} * \text{EXP} \left[ \frac{-\beta_{\perp 0}^2 \sin^2 \alpha}{2\beta_{\perp 0}^2} - \frac{(\beta \cos \alpha - \beta_s)}{2\beta_{\parallel 0}} \right] \quad (11)$$

Where

$c\beta_{\perp 0}$ ,  $c\beta_{\parallel 0}$  are the mean perpendicular and parallel velocity spreads (characteristic constants of the distribution function) about the local geomagnetic field.

$c\beta_s$  is the beam velocity.

This distribution function has the advantage of describing the precipitating suprathermal beam in a form such that the absorption coefficient or growth rate can be calculated analytically. Using this distribution function Melrose determines the growth rate of the radiation as

$$\gamma(f, \theta) = 2\pi \frac{\pi}{2}^{1/2} \frac{n_1}{n_e} \frac{f_p^2 \beta_{\perp 0}^2}{f \beta_{\parallel 0} |\cos \theta|} * \exp \left[ \frac{-(f - f_g - \mu \beta_s \cos \theta)^2}{2f^2 \mu^2 \beta_{\parallel 0}^2 \cos^2 \theta} \right] \quad (13)$$

where

$$g(f, \theta) = \frac{f_g}{f} + \frac{\beta_{\perp 0}^2}{\beta_{\parallel 0}^2} \left( 1 - \frac{f_g}{f} - \mu \beta_s \cos \theta \right)$$

and

$n_1$  = the electron density in the beam

$n_e$  = the local electron density

The sign of  $\gamma(f, \theta)$  is determined by the sign of  $g(f, \theta)$ . For amplification,  $\gamma$  must be negative which requires

$$1 - \frac{\beta_{\perp 0}^2}{\beta_{\parallel 0}^2} \mu \beta_{\parallel 0} |\cos \theta| < 0 \quad .$$

Since the index of refraction is close to 1 for the escaping free space modes, then,

$$\mu |\cos \theta| \leq 1 \quad . \quad (14)$$

For amplification the required anisotropy of the distribution function must become

$$\beta_{\perp 0}^2 > \beta_{\parallel 0} \quad . \quad (15)$$

A threshold anisotropy for marginal instability is thus

$$\beta_{\perp 0}^2 = \beta_{\parallel 0} \quad . \quad (16)$$

A qualitative plot of the electron distribution function in velocity space used in Melrose's analysis for the threshold anisotropy of  $\beta_{\perp 0}^2 = \beta_{\parallel 0}$  is given in the bottom panel of Figure 21. The contour values are merely used to indicate orders of magnitude in  $f(v)$ . Note the large velocities to which the beam (contour 1) extends.

The threshold anisotropy in Melrose's model is obtained as a result of the mirroring effect on the initially narrow (confined to very small pitch angles) beam in the precipitating distribution function. The mirroring effect converts some of the beam's parallel energy into perpendicular energy by the conservation of the first adiabatic invariant as the precipitating part of the distribution moves down the auroral field lines. Thus, for this expression

$$\frac{mv_{\perp}^2}{2B} \propto \frac{\beta_{\perp}^2 \sin^2 \alpha}{B}, \quad (17)$$

to remain constant, as  $B$  increases the pitch angle ( $\alpha$ ) must increase. The beam produces doppler shifted gyroemission which is amplified efficiently when  $\beta_{\perp}^2 > \beta_{\parallel}^2$ . At equilibrium, the decrease in the perpendicular energy due to the amplification of the waves is balanced by the increase of the perpendicular energy due to the mirroring effect. The upper limit to the energy density in the waves is estimated by Melrose as

$$W < n_1 m_e \beta_{\perp}^2 c^2. \quad (18)$$

During the times in which the threshold anisotropy condition is maintained the energy density becomes

$$W < n_1 m_e \beta_{\parallel}^2 c^2. \quad (19)$$

C. Review Of the Theory Of Relativistic Normal  
Cyclotron Resonance As a Mechanism For the  
Generation and Amplification Of AKR

In the theory of relativistic normal cyclotron resonance the source of free energy used in the generation and amplification of kilometric radiation exists in the ascending or reflected part of the electron distribution function. The upgoing electrons with energies of  $\sim 1$  keV amplify doppler shifted electromagnetic waves (generated by a relativistic normal cyclotron instability) provided that there exists a loss-cone feature in the ascending part of the distribution function. The loss-cone feature is characterized by a depletion of upgoing electrons having small pitch angles relative to the geomagnetic field. This feature constitutes a population inversion in the perpendicular energy of the electron distribution function. The anisotropy (or population inversion) in the perpendicular part of the ascending velocity distribution is the source of free energy which drives the instability.

In a loss-cone distribution, since the average particle energy parallel to the geomagnetic field is much less than the average particle energy perpendicular to the field the most efficient coupling to excited modes occurs for perpendicular propagation. The dispersion relationship given by Wu and Lee [1979] for electromagnetic waves propagating perpendicular to an ambient magnetic field in the extraordinary mode is:

$$D(\vec{k}, \omega) = 1 - \frac{c^2 k^2}{\omega^2} + \frac{\omega_e^2}{\omega^2 n_e} \int d^3v \left[ \Omega_e \frac{\partial F}{\partial v_{\perp}} + k_{\parallel} v_{\perp} \frac{\partial F}{\partial v_{\parallel}} \right] \\ * \frac{v_{\perp} \left( \frac{dJ_1(b)}{db} \right)^2}{\left( \omega - \frac{\Omega_e}{\gamma} - k_{\parallel} v_{\parallel} \right)} = 0 \quad (20)$$

where

$\omega$  = wave frequency

$$\omega_e = 2\pi f_p$$

$$\Omega_e = 2\pi f_g$$

$$F = n_+ F_+ + n_- F_-$$

$n_+ F_+$  is the ascending part of the electron distribution function and its density ( $n_+$ )

$n_- F_-$  is the precipitating part of the electron distribution function and its density ( $n_-$ )

$$n_e = n_+ + n_- \text{ (total electron density)}$$

and

$$J_1(b) = J_1 \left( \frac{k_{\perp} v_{\perp}}{\Omega_e} \right); \text{ first order Bessel function}$$

In general, for the extraordinary mode, the dispersion relation for perpendicular propagation is represented by a two by two determinant.

The above relationship is a good approximation when  $c^2 k^2 \gg \omega_e^2$  as

demonstrated by Montgomery and Tidman [1964]. In addition, a sum over all particle species and orders of the  $J_N(b)$  Bessel function in  $D(\vec{k}, \omega)$  have been reduced to integrating over just the electron distribution function and the  $J_1(b)$  ( $N=1$ ) Bessel function which produces the largest contribution to the integral. If relativistic effects are neglected an unstable wave mode ( $D(\vec{k}, \omega) = 0$ ) occurs for  $\omega = \Omega_e$  and thus, electromagnetic waves occur at the local electron gyrofrequency. These waves, however, (if they are allowed to grow) can not escape since  $\Omega_e < 2\pi f_{R=0}$ . When relativistic effects are considered then an excited wave mode determined from  $D(\vec{k}, \omega) = 0$  occurs slightly above  $\Omega_e$  by a Doppler shifted amount. When  $\omega_e \ll \Omega_e$ , allowing  $\omega > 2\pi f_{R=0}$  then the Doppler shifted cyclotron emission can escape. The condition  $\omega_e \ll \Omega_e$  according to the Wu and Lee mechanism is satisfied only along auroral field lines where parallel electric fields exist. The parallel electric fields are believed to deplete the very low energy electrons thus reducing  $\omega_e$ .

Wu and Lee [1979] determine under what conditions the Doppler shifted cyclotron emission will grow by examining the sign of  $\omega_i$ . Since plane wave solutions have been assumed, when  $\omega_i > 0$  the cyclotron instability will grow. Assuming that the wave frequency  $\omega$  can be written in terms of a real and imaginary part,  $\omega = \omega_r + i\omega_i$  and that  $\omega_r \gg \omega_i$  then

$$\omega_i = \frac{-D_1(\vec{k}, \omega_r)}{\frac{\partial D_r(\vec{k}, \omega_r)}{\partial \omega_r}}$$

Substitution of the dispersion relation into the expression for  $\omega_i$  yields:

$$\omega_i = \frac{\pi^2 \omega_e}{4\omega_r} \frac{n_+}{n_e} \int dv_{||} \int dv_{\perp} v_{\perp}^2 * \delta \left[ \omega_r - \Omega_e \left( 1 - \frac{v_{\perp}^2}{2c^2} \right) - k_{||} v_{||} \right] * \left\{ \Omega_e \frac{\partial F_+}{\partial v_{\perp}} + k_{||} v_{\perp} \frac{\partial F_+}{\partial v_{||}} \right\} \quad (21)$$

Where only the ascending part of the distribution function ( $F_+$ ) is involved in the growth of the instability. This can be seen by noting that  $\omega_i \neq 0$  when the delta function ( $\delta$ ) in  $\omega_i$  is

$$\omega_r - \Omega_e \left( 1 - \frac{v_{\perp}^2}{2c^2} \right) - k_{||} v_{||} = 0 \quad (22)$$

This condition is possible for particles with  $k_{||} v_{||} > 0$ . For waves generated primarily perpendicular to the local magnetic field but with a small  $k_{||} > 0$  component, only ascending electrons ( $v_{||} > 0$ ) can resonantly amplify the waves. For  $\omega_i$  to be positive,  $F_+$  should contain a loss cone feature  $F_+(v_{||}, v_{\perp} = 0) = 0$  which makes  $\frac{\partial F_+}{\partial v_{\perp}} > 0$  for a certain range of  $v_{\perp}$  velocities. The top panel of Figure 21 is a contour plot of the loss-cone distribution function plotted in velocity space proposed by Wu and Lee which is necessary for growth of the normal cyclotron instability. For  $v_{||} \simeq 0$  the dashed contour lines (top panel of Figure 21) produce a region where  $\frac{\partial F_+}{\partial v_{\perp}} > 0$ . Substituting the loss-cone distribution function



$$F_+(v_{||}, v_{\perp}) = \left(\frac{v_{\perp}}{\alpha_{\perp}}\right)^2 \frac{2}{(\pi)^{3/2}} \frac{\text{EXP}\left[-v_{\perp}^2/\alpha_{\perp}^2\right]}{\alpha_{\perp}^2(\alpha_1 - \alpha_2)} * \left\{ \text{EXP}\left[\frac{-v_{||}^2}{\alpha_1^2}\right] - \text{EXP}\left[\frac{-v_{||}^2}{\alpha_2^2}\right] \right\} \quad (23)$$

where  $\alpha_2 < \alpha_1$  (adjustable velocity parameters)

$\alpha_{\perp}$  is a characteristic perpendicular velocity

and with the condition

$$v_{||} > 0$$

in the expression for  $\omega_1$ , Wu and Lee have determined that the maximum growth rate for the escaping doppler shifted normal cyclotron instability (in the X propagation mode) occurs where  $f = f_{R=0}$  when  $f_{R=0} \simeq f_g^-$ . In addition, the maximum growth rate occurs for waves generated nearly perpendicular to the local geomagnetic field (with initial wave normal angles  $70^\circ < \psi \leq 85^\circ$ ; see Figure 23 top panel).

#### D. Comparison Of the Direct Generation Mechanisms

##### With AE-D Plasma Observations

The direct generation mechanisms discussed in Section II-B and -C require certain features in the electron distribution functions of auroral zone plasmas for the generation and amplification of auroral kilometric radiation. Until the actual distribution functions

responsible for AKR generation are examined in detail the form of the free energy ultimately responsible for this emission will not be precisely known. It is almost certain that the AE-D auroral zone plasma observations are made at altitudes below (not necessarily directly below) the source region for AKR. However, it still is of interest to examine and contrast the suprathermal electron distributions observed in the auroral zone by AE-D with those proposed for the generation of kilometric radiation (in Figure 21). A comparison of this nature would be important if striking similarities were found.

The amplified doppler shifted mechanism proposed by Melrose has many features which are in close agreement with the observations presented in this study. Inverted-V electron precipitation events are essential for AKR generation in Melrose's mechanism. The results of Section IV show that the occurrence of inverted-V events are clearly correlated with auroral kilometric radiation. The AKR power flux as proposed by Melrose is related to the square of the characteristic perpendicular velocity in the precipitating electron distribution:

$$W \propto \beta_{\perp 0}^2 .$$

For the threshold anisotropy of  $\beta_{\perp 0}^2 = \beta_{\parallel 0}$  then

$$W \propto \beta_{\parallel 0} .$$

Since the mean parallel velocity ( $\beta_{||0}$ ) is related to the beam velocity, Melrose's mechanism would thus predict a relationship between the AKR power flux generated and the peak energy in the inverted-V events. A good correlation between these two parameters has been demonstrated in Section IV-C. These results provide strong arguments in favor of the generation of kilometric radiation by amplified doppler shifted gyroemission. However, a closer examination of the auroral zone plasmas is necessary to determine the validity of the Wu and Lee mechanism (additional comments concerning Melrose's mechanism will also be made).

During the passes in which AE-D was in the spinning mode the LEE experiment measured electron particle fluxes with energies from 200 eV to 25 keV at 15 different pitch angles per spin. This enabled a complete electron distribution function  $F(v)$ , with velocities from about 8,000 km/sec to greater than 90,000 km/sec to be determined. The calculation of  $F(v)$  from the observed differential particle fluxes at specific energies is discussed in detail in Section IV-C. Figure 22 shows three inverted-V electron distribution functions and their energy fluxes which are associated with weak (top), moderate (middle) and intense (bottom) auroral kilometric radiation. The actual associated AKR power fluxes are directly below (center) each event. The inverted-V electron distributions on the left hand side of Figure 22 are shown as contour plots in velocity space like those of Figure 21. The dot pattern at the center of each distribution function is the part of the distribution that is not observed by AE-D and is at velocities less than 8,400 km/sec. The corresponding energy flux (defined in

Section IV-C) in each part of the distribution function at the observed pitch angle has been calculated and is plotted in polar form (magnitude versus pitch angle) on the right hand side of Figure 22. The loss-cone angle  $\alpha_L$  for each distribution is calculated from the formula

$$\sin^2 \alpha_L = \frac{B_s}{B_A} = \left( \frac{R_A}{R_s} \right)^3 \left[ \frac{4L - 3R_s}{4L - 3R_A} \right]^{1/2} \quad (24)$$

where

$B_s$  is the magnetic field intensity at the satellite

$B_A$  is the magnetic field intensity at the top of the atmosphere (100 km)

$R_s$  = geocentric radial distance of the satellite

$R_A$  = geocentric radial distance to the top of the atmosphere

$L$  = L value of the satellite

The value of the loss cone is labeled only for the ascending part of the distribution function.

One important characteristic of the inverted-V distribution functions which is clearly evident in Figure 22 is that in the descending part (from  $0^\circ$  to  $90^\circ$  pitch angle) there is a beam or peak at high velocities and nearly centered about  $0^\circ$  pitch angle. The  $6 \times 10^{-1} \text{ sec}^3 / \text{km}^6$  contour in the distribution function 75/328 1734 UT (bottom panel) of Figure 22 is a plateau feature. Note also that there is always from  $1/2$  to 1 order of magnitude more energy flux in the loss cone for the

descending portion of  $F(v)$  than in the ascending (from  $90^\circ$  to  $180^\circ$  pitch angle) portion. A loss cone feature is partially evident in the ascending part of the distribution function 75/323 1715 UT (top panel).

The formation of a loss cone in the ascending portion of an inverted-V electron distribution is widely believed (see, for example, Lin and Hoffman [1979]) to be due to electrons trapped between their mirror points (just above the atmosphere) and the accelerating potential drop (at high altitudes). Isotropic back-scattered electrons fill in the loss-cone feature. It is interesting to note that from an examination of ten inverted-V electron distribution functions at the time of the peak energy (three are shown in Figure 22) the loss-cone feature is not present in six of the distribution functions and only weakly in the remaining four.

It is important to note when comparing these observed auroral zone plasmas (Figure 22) with the theoretical models (Figure 21) that according to the Wu and Lee mechanism the ascending portion of the distributions observed by AE-D are the plasmas whose energy will be used in AKR generation. According to Melrose, the descending portion of the inverted-V distributions observed by AE-D have already been involved in the generation of AKR.

Let's examine the Wu and Lee theory with respect to the observed distribution functions. There appears to be no distinctive loss-cone feature in the ascending part of the inverted-V electron distributions. Since the AE-D plasma observations are made at relatively low altitudes it is not known whether the observed distributions are representative

of those in the source region. If a strong loss-cone feature could develop in these ascending distributions, as they move rapidly upward toward the source, there is still characteristically from 1/2 to 1 order of magnitude less energy available than what was found in the descending portions (see Figure 22). This indicates that conversion efficiencies much higher than 1% may be needed for the amplification of the normal cyclotron waves to the intensities observed for the kilometric radiation.

A major feature in the amplified doppler shifted gyroemission theory proposed by Melrose is the large anisotropy  $\beta_{\perp 0}^2 = \beta_{\parallel 0}$  in the precipitating beam (see Figure 21) required for marginal instability. If the inverted-V events in Figure 2 were the ultimate source of energy for AKR generation then it has been determined that these distributions represent the conditions for the highest efficiencies found (see Figure 17). A qualitative comparison of the inverted-V distributions in Figure 22 with Melrose's model distribution in Figure 21 indicates that the extreme anisotropy required by Melrose for efficient amplification of AKR is not found in the observed inverted-V distributions. Calculations of  $\beta_{\parallel 0}$  (where  $\beta_{\parallel 0}^2 = 2 \langle (\beta \cos \alpha - \beta_s)^2 \rangle$ ) and  $\beta_{\perp 0}^2$  (where  $\beta_{\perp 0}^2 = \langle \beta \sin^2 \alpha \rangle$ ) for the distributions in Figure 22 reveal that  $\beta_{\perp 0}^2$  is too small to satisfy even the threshold anisotropy ( $\beta_{\perp 0}^2 = \beta_{\parallel 0}$ ) by a factor of 12 to 13 for the electron distributions shown in the top and middle panels and by a factor of 5 for the distribution function in the bottom panel. Since the AE-D observations in Figure 22 were from the auroral zone at altitudes of less than 1,000 km it is

expected that  $\beta_{10}$  would have been even smaller for these distributions at altitudes of  $1.5 R_E$  (average AKR source region) due to the conservation of the first adiabatic invariant.

In summary, the features in auroral zone distribution functions necessary for the amplification of doppler shifted gyroemission and normal cyclotron waves are not found at AE-D altitudes ( $< 1000$  km). Whether these features actually exist in electron distribution functions in the source region can not be determined in this study. Since  $1/2$  or  $1$  order of magnitude less energy flux exists in the ascending portion of inverted-V electron distributions than in the precipitating portion conversion efficiencies higher than  $1\%$  may be needed for growth of the normal cyclotron instability.

#### E. Comparison Of the Direct Generation Mechanisms With Hawkeye Emission-Cone Observations

Another observational aspect of this study which can be compared with the two direct generation mechanisms discussed, is the detailed intensity distribution of the AKR emission cone determined in Section II. It is important to recognize at the onset of this discussion that the detailed intensity distribution of the emission cone may be determined by either the generation mechanism itself or by propagation effects. The term propagation effect, as used here, implies that after the radiation has initially been generated its propagation direction is drastically altered by, for example, scattering in or near the source region or reflection or refraction of the radiation by the plasmasphere.



Multiple sources spread out in longitude or latitude could also affect the illumination pattern as observed far from the earth. To exhaustively study all possible propagation effects on the kilometric waves is beyond the scope of this study. But if the illumination pattern plotted in the average source-centered coordinates in Figure 6 is representative of the initial wave normal angles (angle between the propagation vector and the local magnetic field) in the average source region then a straightforward interpretation can be made. The results of ray tracing calculations in the model magnetosphere presented in this study (Figure 20) for the Melrose, and Wu and Lee mechanisms is shown in Figure 23. The initial wave normal angles ( $\psi$  and  $\theta$ ) in the two direct generation mechanisms discussed are considerably different. In Melrose's mechanism (bottom panel of Figure 23), emission along the geomagnetic source field ( $\vec{B}$ ) and to within  $60^\circ$  of  $\vec{B}$  produces a filled in emission cone (shaded region) as observed far from the earth. However, radiation with wave normal angles ( $\psi$ ) almost exclusively perpendicular to  $\vec{B}$  in the source region are the only angles allowed for escaping radiation in the Wu and Lee mechanism producing a hollow emission cone as observed far from the earth (shaded region in the top panel of Figure 23). Tangents to the auroral field lines where AKR is generated, on the average, will point near a latitude of  $60^\circ$  at 0 hours local time in Figure 6. Since the emission cone is uniformly illuminated throughout this region then only the generation of AKR along  $\vec{B}$ , as demanded in Melrose's mechanism, in the absence of propagation effects, would qualitatively reproduce the observations.



If auroral kilometric radiation is generated initially perpendicular to  $\vec{B}$ , as demanded by the Wu and Lee mechanism, then propagation effects must be responsible for the resultant illumination pattern. It seems unlikely that multiple sources alone could be distributed well enough and emit comparable power independently to fill in the emission cone, on the average, to within 10 db as illustrated in Figure 6 if, in each source region, only radiation perpendicular to  $\vec{B}$  was allowed to escape. In addition, all the simultaneous observations of auroral kilometric radiation from Hawkeye and IMP-6 in the northern emission cone (see Figure 7 as an example) indicate that they are observing the same source which illuminates the entire emission cone simultaneously and uniformly. Green et al. [1977] observed that the plasmasphere on the nightside of the earth acts as a propagation barrier to AKR. The ray tracing of the Wu and Lee mechanism shown in the top panel of Figure 23 illustrates that radiation generated nearly perpendicular to  $\vec{B}$  in the average source region suffers less than a  $70^\circ$  refraction from the nightside plasmasphere. For refraction or reflection off the nightside plasmasphere, to fill in the emission cone, up to nearly  $180^\circ$  deflections of the incoming waves would be required. If auroral kilometric radiation is generated perpendicular to the geomagnetic field then scattering in or very near the source region would be the most likely explanation for the filled-in beam pattern at 178 kHz observed far from the earth (see Figure 6).

## VIII. CONCLUSIONS

A study of the detailed intensity distribution of the AKR emission cone revealed that the source or sources of auroral kilometric radiation illuminate the emission cone nearly uniformly (to within 10 db) and simultaneously when examined in a coordinate system with the average AKR source region at the origin. It is found on the basis of the emission cone study that auroral kilometric radiation is correlated with auroral particle precipitation in the 19 to 01 hour magnetic local time sector. The correlations are:

- 1) As the observed AKR power flux increases, so does the integrated current sheet intensity of field-aligned auroral zone currents increase.
- 2) Qualitative AKR emission is more closely correlated with inverted-V electron precipitation than with plasma sheet precipitation.
- 3) As the observed AKR power flux increases, so does the simultaneously observed peak energy in inverted-V electron precipitation events increase.
- 4) As the observed AKR power flux increases, so does the tail temperature at  $\sim 0^\circ$  pitch angle in inverted-V distribution functions increase.

- 5) As the observed AKR power flux increases, so does the energy flux in the high energy tail of the precipitating inverted-V events increase.

A study of the amount of power in inverted-V particle precipitations and the amount of power in simultaneous AKR bursts has lead to the conclusion that the efficiency of converting charge particle power into auroral kilometric radiation ranges from  $10^{-5}\%$  to as high as 1%.

Analysis of low altitude ( $\sim 2.0$  to  $2.5 R_E$ ) southern hemisphere auroral zone observations of auroral kilometric radiation from the Hawkeye spacecraft have led to the following conclusions:

- 1) Intense auroral kilometric radiation has an observed low frequency cutoff near the local electron gyrofrequency when  $f_p^- \ll f_g^-$ .
- 2) This low frequency cutoff is consistent with AKR propagating primarily in the right-hand extraordinary (R-X) polarized mode.
- 3) The maximum electric field strength of AKR observed in or near the average source region is 12 mV/m.
- 4) The maximum power flux of AKR observed in or near the average source region is consistent with this radiation being almost completely electromagnetic.

The generation mechanisms of auroral kilometric radiation proposed by Melrose [1976] and Wu and Lee [1979] have many features which are consistent with the observations presented in this study. These are:

- 1) Direct conversion of particle energy into electromagnetic radiation is the most probable explanation for the observed high efficiencies.
- 2) The radiation is generated primarily in the R-X polarized mode.
- 3) The radiation can escape only in regions where  $f_g^- \gg f_p^-$ .

Evidence has been presented which supports the following features in the amplified doppler shifted generation mechanism proposed by Melrose:

- 1) The inverted-V electron precipitation events are the source of energy for auroral kilometric radiation.
- 2) Under certain circumstances the AKR intensity increases as the beam speed of the inverted-V event increases.
- 3) The AKR emission cone as observed far from the earth would be filled in.

However, the conditions for amplification of auroral kilometric radiation from large perpendicular velocity components in the inverted-V beam as proposed by Melrose, qualitatively, are not found in the low altitude AE-D observations.

Several observations presented in this study are not in close agreement with predictions by Wu and Lee [1979] of AKR generation from a normal cyclotron resonance instability. These include:

- 1) Strong loss-cone features necessary for the wave growth of the normal cyclotron instability were not found in the ascending inverted-V electron distributions at altitudes below 1000 km.
- 2) If intense auroral kilometric radiation was generated from the available energy in the observed ascending portions of inverted-V distributions conversion efficiencies greater than 1% would be necessary.
- 3) In the absence of propagation effects near the source region the emission cone (as observed far from the earth) of the escaping normal cyclotron radiation would be hollow.

Since the auroral electron distribution functions presented in this study are not observed in the AKR source region, it is not possible to conclusively determine if either of the direct generation mechanisms plays a major role in the generation of auroral kilometric radiation.

## REFERENCES

- Ackerson, K. L., and L. A. Frank, Correlated satellite measurements of low-energy electron precipitation and ground-based observations of a visible auroral arc, J. Geophys. Res., 77, 1128, 1972.
- Alexander, J. K., and M. L. Kaiser, Terrestrial kilometric radiation  
1. Spatial structure studies, J. Geophys. Res., 81, 5948, 1976.
- Armstrong, J. C., and Zmuda, A. J., Triaxial magnetic measurements of field-aligned currents at 800 kilometers in the auroral region: Initial results, J. Geophys. Res., 78, 6802, 1973.
- Barbosa, D. D., Electrostatic mode coupling at  $2\omega_{UH}$ : A generation mechanism for auroral kilometric radiation, Ph D. Dissertation, Dept. of Physics, Univ. of California, Los Angeles, 1976.
- Benson, R. F., Source mechanism for terrestrial kilometric radiation, Geophys. Res. Letts., 2, 52, 1975.

- Benson, R. F., and W. Calvert, Isis 1 observations at the source of auroral kilometric radiation, Geophys. Res. Lett., (accepted for publication), 1979.
- Boswell, R. W., Energetic ions and electromagnetic radiation in auroral regions, Geophys. Res. Lett., 5, 395, 1978.
- Casserly, R. T., Jr., and P. A. Cloutier, Rocket-based magnetic observations of auroral Birkeland currents in association with a structured auroral arc, J. Geophys. Res., 80, 2165, 1975.
- Dulk, G. A., Characteristics of Jupiter's decametric radio source measured with arc-second resolution, Astrophys. J., 159, 671, 1970.
- Dunckel, N., B. Ficklin, L. Rorden, and R. A. Helliwell, Low-frequency noise observed in the distant magnetosphere with Ogo 1, J. Geophys. Res., 75, 1854, 1970.
- Frank, L. A., and K. L. Ackerson, Observations of charged particle precipitation into the auroral zone, J. Geophys. Res., 76, 3612, 1971.
- Galeev, A. A., and V. V. Krasnosel'skikh, Strong langmuir turbulence in the earth's magnetosphere as a source of kilometric radio emission, JETP Lett., 24, 515, 1976.

Gallagher, D. L., and D. A. Gurnett, Auroral kilometric radiation: Time-averaged source location, J. Geophys. Res., (submitted for publication), 1979.

Goertz, C. K., Double layers and electrostatic shocks in space, Rev. Geophys. Space Phys., 17, 48, 1979.

Green, J. L., D. A. Gurnett, and S. D. Shawhan, The angular distribution of auroral kilometric radiation, J. Geophys. Res., 82, 1825, 1977.

Gurnett, D. A., The earth as a radio source: Terrestrial kilometric radiation, J. Geophys. Res., 79, 4227, 1974.

Gurnett, D. A., and L. A. Frank, Thermal and suprathermal plasma densities in the outer magnetosphere, J. Geophys. Res., 76, 2355, 1974.

Gurnett, D. A., and R. R. Shaw, Electromagnetic radiation trapped in the magnetosphere above the plasma frequency, J. Geophys. Res., 78, 8136, 1973.

Gurnett, D. A., and J. L. Green, On the polarization and origin of auroral kilometric radiation, J. Geophys. Res., 83, 689, 1978.



- Gurnett, D. A., R. R. Anderson, F. L. Scarf, R. W. Fredricks, and E. J. Smith, Initial results from the ISEE-1 and -2 Plasma Wave Investigation, Space Sci. Rev., (accepted for publication), 1979.
- Iijima, T., and T. A. Potemra, Field-aligned currents in the dayside cusp observed by Triad, J. Geophys. Res., 81, 5971, 1976.
- Iijima, T., and T. A. Potemra, Large-scale characteristics of field-aligned currents associated with substorms, J. Geophys. Res., 83, 599, 1978.
- Jones, D., Mode-coupling of Z-mode waves as a source of terrestrial kilometric and Jovian decametric radiations, Astron. Astrophys., 55, 245, 1977a.
- Jones, D., Jovian and terrestrial "harmonic" radiations, Geophys. Res. Lett., 4, 121, 1977b.
- Kaiser, M. L., and J. K. Alexander, Source location measurements of terrestrial kilometric radiation obtained from lunar orbit, Geophys. Res. Lett., 3, 37, 1976.
- Kaiser, M. L., and J. K. Alexander, Terrestrial kilometric radiation  
3. Average spectral properties, J. Geophys. Res., 82, 3273, 1977a.

Kaiser, M. L., and J. K. Alexander, Relationship between auroral substorms and the occurrence of terrestrial kilometric radiation, J. Geophys. Res., 82, 5283, 1977b.

Kaiser, M. L., J. K. Alexander, A. C. Riddle, J. B. Pearce, and J. W. Warwick, Direct measurements by Voyagers 1 and 2 of the polarization of terrestrial kilometric radiation, Geophys. Res. Lett., 5, 857, 1978.

Kindel, J. M., and C. F. Kennel, Topside current instabilities, J. Geophys. Res., 76, 3055, 1971.

Kintner, P. M., M. C. Kelley, and F. S. Mozer, Electrostatic hydrogen cyclotron waves near one earth radius altitude in the polar magnetosphere, Geophys. Res. Lett., 5, 139, 1978.

Kurth, W. S., M. M. Baumbach, and D. A. Gurnett, Direction finding measurements of auroral kilometric radiation, J. Geophys. Res., 80, 2764, 1975.

Lin, C. S., and R. A. Hoffman, Characteristics of the inverted-V event, J. Geophys. Res., 84, 1514, 1975.

- Melrose, D. B., An interpretation of Jupiter's decametric radiation and the terrestrial kilometric radiation as direct amplified gyroemission, Astrophys. J., 207, 651, 1976.
- Montgomery, D. C., and D. A. Tidman, Plasma Kinetic Theory, McGraw-Hill, New York, 1964.
- Palmadesso, P. J., T. P. Coffey, S. L. Ossakow, and K. Papadopoulos, Topside ionosphere ion heating due to electrostatic ion cyclotron turbulence, Geophys. Res., Lett., 1, 105, 1974.
- Palmadesso, P. J., T. P. Coffey, S. L. Ossakow, and K. Papadopoulos, Generation of terrestrial kilometric radiation by a beam-driven electromagnetic instability, J. Geophys. Res., 81, 1762, 1976.
- Roux, A., and R. Pellat, Coherent generation of the terrestrial kilometric radiation by non-linear beatings between electrostatic waves, J. Geophys. Res., (submitted for publication), 1979.
- Scarf, F. L., A new model for the high frequency decametric radiation from Jupiter, J. Geophys. Res., 79, 3835, 1974.
- Shaw, R. R., and D. A. Gurnett, Electrostatic noise bands associated with the electron gyrofrequency and plasma frequency in the outer magnetosphere, J. Geophys. Res., 80, 4259, 1975.

Stix, T. H., The Theory of Plasma Waves, McGraw-Hill, New York, 1962.

Torbert, R. B., F. S. Mozer, S. von Glinski, and M. Temerin, Observations of the local plasma density below 8000 km on the S3-3 satellite, (abstract), EOS Trans., AGU, 58, 1214, 1977.

Voots, G. R., D. A. Gurnett, and S.-I. Akasofu, Auroral kilometric radiation as an indicator of auroral magnetic disturbances, J. Geophys. Res., 82, 2259, 1977.

Winningham, J. D., F. Yasuhara, S.-I. Akasofu, and W. J. Heikkila, The latitudinal morphology of 10-eV to 10-keV electron fluxes during magnetically quiet and disturbed times in the 2100-0300 MLT sector, J. Geophys. Res., 80, 3148, 1975.

Wu, C. S., and L. C. Lee, A theory of the terrestrial kilometric radiation, Astrophys. J., (submitted for publication), 1979.

Zmuda, A. J., and J. C. Armstrong, The diurnal flow pattern of field-aligned currents, J. Geophys. Res., 79, 4611, 1974.

## APPENDIX A: TABLES

TABLE 1

AE-D ELECTRON MEASUREMENTS	HAWKEYE ELECTRIC FIELD MEASUREMENTS		
	AKR DETECTED	NO AKR DETECTED	ROW SUM
INVERTED-V PRECIPITATION AND NO PLASMA SHEET PRECIPITATION	15%	0%	15%
INVERTED-V AND PLASMA SHEET PRECIPITATION	49%	2%	51%
PLASMA SHEET PRECIPITATION AND NO INVERTED-V PRECIPITATION	9%	25%	34%
COLUMN SUM	73%	27%	100%

THE DISTRIBUTION OF ELECTRIC FIELD MEASUREMENTS WHEN HAWKEYE IS IN THE AKR EMISSION CONE AS A FUNCTION OF AE-D PRECIPITATING ELECTRON MEASUREMENTS IN THE AURORAL OVAL FROM 20 HOURS TO 01 HOUR MAGNETIC LOCAL TIME. PERCENTAGES BASED ON 93 SIMULTANEOUS OBSERVATIONS.

TABLE 2

## PROPOSED GENERATION MECHANISMS

MECHANISMS	AUTHORS	COUPLING	POLARIZATION	SPECIAL CONDITIONS
$\frac{3}{2} F_G^-$ EMISSION	SCARF, 1974 GURNETT, 1974	ES $\rightarrow$ EM	R-X	$F_\omega = \left(\frac{3}{2}\right) F_G^-$ WHERE $F_{R=0} < \left(\frac{3}{2}\right) F_G^-$
STIMULATED PLASMA OSCILLATIONS AT $F_{UHR}$ FROM SUPRATHERMAL ELECTRONS	BENSON, 1975	ES $\rightarrow$ EM $\left(\frac{1}{2}\right) \rightarrow$ EM	L-O	$F_\omega \approx F_P^-$
BEAM-DRIVEN INSTABILITY	PALMADESSO ET AL., 1976	EIC $\rightarrow$ EM	L-O	$F_G^- < F_\omega < F_{UHR}$
AMPLIFIED DOPPLER SHIFTED GYROEMISSION	MELROSE, 1976	DIRECT EM	R-X	$F_\omega \approx 1.2 F_G^-$ WHERE $F_{R=0} < 1.2 F_G^-$
ELECTROSTATIC MODE COUPLING AT $2 F_{UHR}$	BARBOSA, 1976	ES $\rightarrow$ EM	(PARTIALLY) L-O	1-3 V/M ES WAVES AT $F_{UHR}$ $F_\omega = 2 F_{UHR}$
			(PARTIALLY) R-X	

TABLE 2 (con't)

MECHANISMS	AUTHORS	COUPLING	POLARIZATION	SPECIAL CONDITIONS
CAVITON COLLAPSE	GALEEV AND KRASNOSEL'SKIKH 1976	ES $\rightarrow$ EM	L-O	$F_{\omega} \approx 2 F_P^-$
MODE COUPLING OF Z-MODE WAVES (EM WAVE-WAVE INTERACTIONS)	JONES, 1977A AND JONES, 1977B	EM(z) $\leftrightarrow$ EM(z) $\downarrow$ EM	(PARTIALLY) L-O	$F_{\omega} \approx F_P^-$
			(PARTIALLY) R-X	$F_{\omega} \approx F_{L=0} + F_{UHR}$
STIMULATED ES WAVES AT $F_{UHR}$ FROM UPWARD FLOWING IONS	BOSWELL, 1978	ES $\rightarrow$ EM	L-O	$F_{\omega} = F_{UHR}$
NON-LINEAR ES WAVE- WAVE INTERACTIONS AT $F_{UHR}$	ROUX AND PELLAT, 1979	ES $\leftrightarrow$ ES $\downarrow$ EM	(PARTIALLY) L-O	$F_{\omega} = F_{UHR}$
			(PARTIALLY) R-X	$F_{\omega} = 2 F_{UHR}$
RELATIVISTIC NORMAL CYCLOTRON RESONANCE	WU AND LEE, 1979	DIRECT	R-X	$F_{\omega} \geq F_{R=0} > F_G^-$



TABLE 2 (CON'T)

ES	= ELECTROSTATIC WAVE
EM	= ELECTROMAGNETIC WAVE
EM (Z)	= ELECTROMAGNETIC WAVE IN THE Z MODE
EIC	= ELECTROSTATIC ION CYCLOTRON WAVE
$F_{\omega}$	= FREQUENCY OF THE WAVE
$F_P$	= ELECTRON PLASMA FREQUENCY
$F_G$	= ELECTRON GYROFREQUENCY
$F_{UHR}$	= UPPER HYBRID FREQUENCY
$F_{R=0}$	= THE R-X CUTOFF FREQUENCY

## APPENDIX B: FIGURES

Figure 1      Bursts or storms of auroral kilometric radiation as observed by the Hawkeye spacecraft near apogee at 178, 100, 56.2 and 42.2 kHz. The sporadic nature of this radiation is exhibited in the intensity of the noise which varies by more than 20 db in a few minutes or less and 80 db over the course of the storm. Storms of auroral kilometric radiation lasting for several hours are not uncommon.

APRIL 21, 1975

## AURORAL KILOMETRIC RADIATION

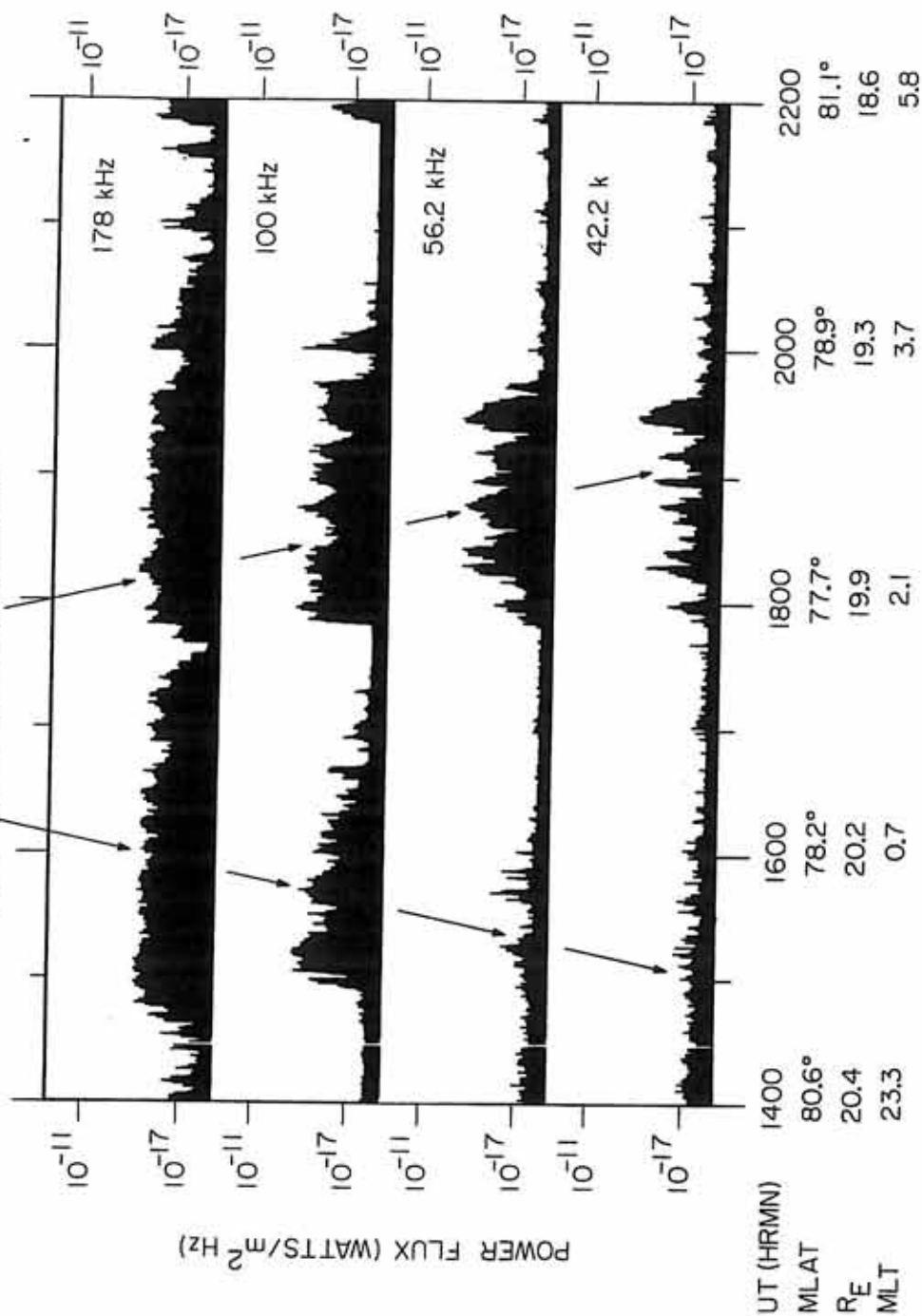


Figure 1

Figure 2

Schematic representation of the results from Gallagher and Gurnett [1979] on their determination of the AKR source region(s). The average source region of auroral kilometric radiation at 178 kHz is found in the 11 to 23 hour magnetic local time meridian at approximately  $2.5 R_E$  (earth radius) geocentric radial distance along auroral field lines ( $\sim 70^\circ$  invariant latitude) on the nightside. The borders of the emission pattern (shaded region) were defined by a drop in the observed AKR power flux by two or more orders of magnitude.

A-678-704-1

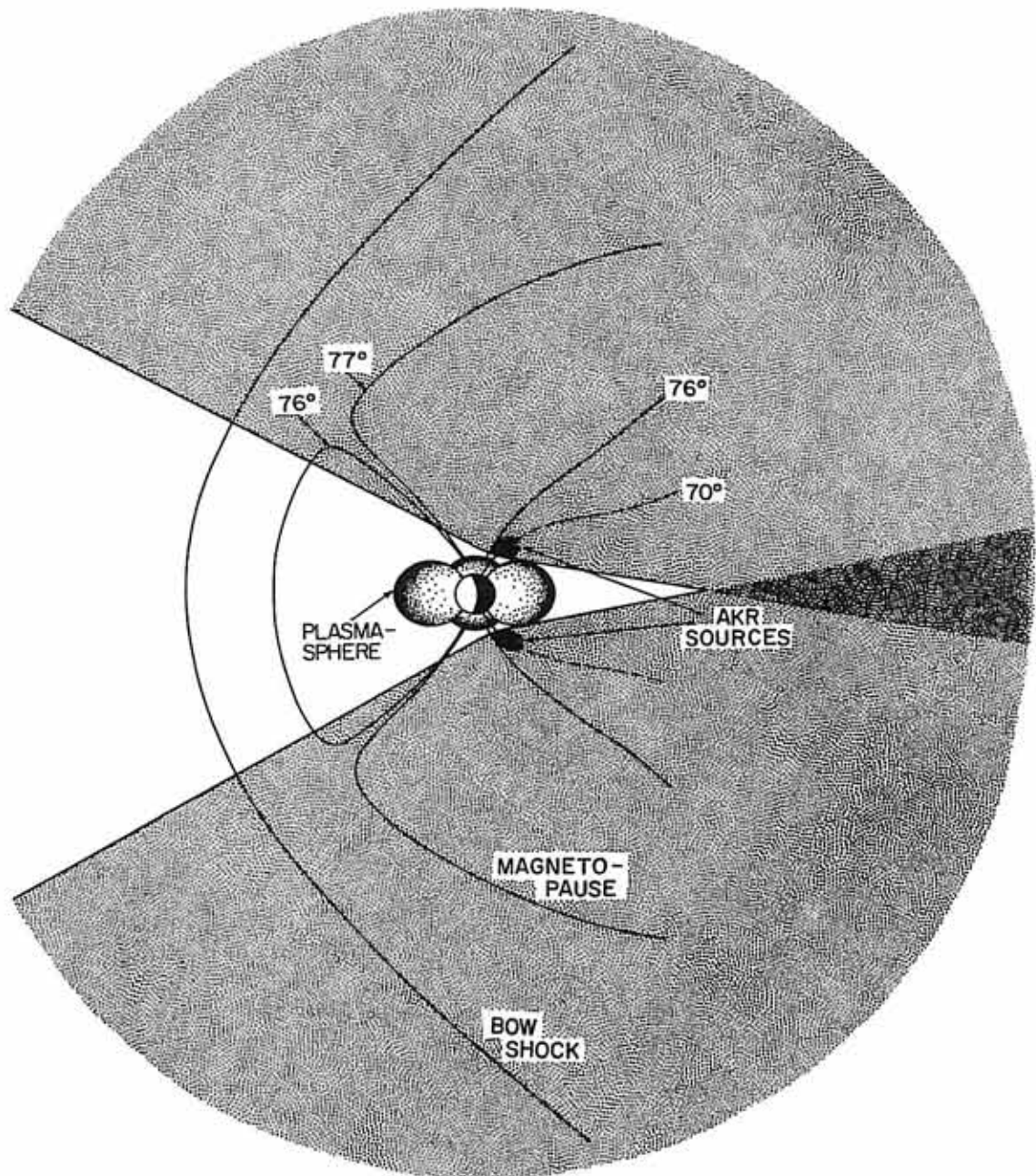


Figure 2

Figure 3      The frequency of occurrence diagram of auroral kilometric radiation (from Green et al. [1977]) as observed from the IMP-6 and Hawkeye spacecraft at 178 kHz as a function of magnetic local time and magnetic latitude. Note that the threshold used varied as  $1/R^2$ . Since the source region of AKR was not well known at the time of this study, the R variable used was the satellite's geocentric radial distance.

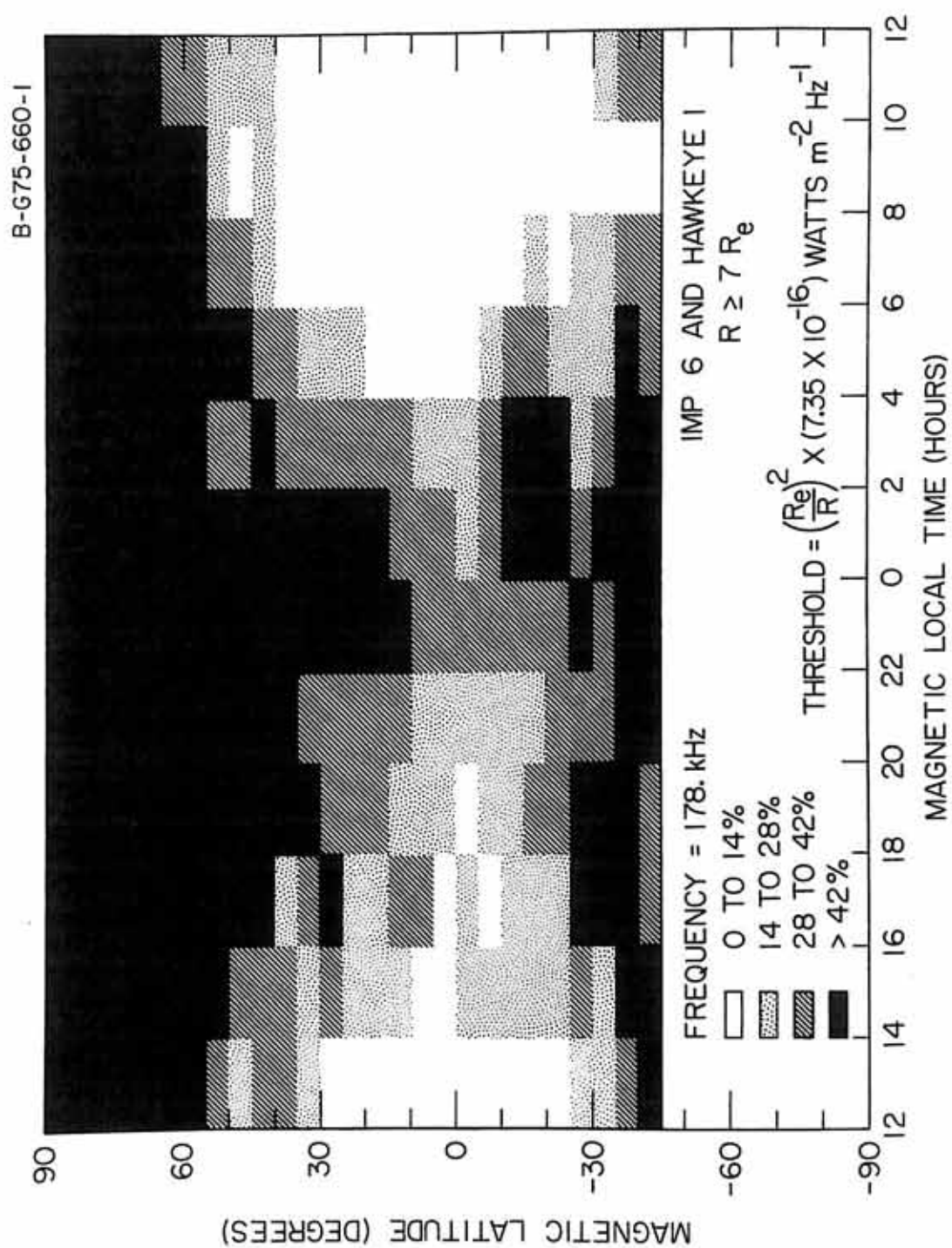


Figure 3



Figure 4 Scatter plot of simultaneous measurements of AKR electric field intensities at 178 kHz from IMP-6 (normalized to  $30 R_E$ ) and the AE index from a paper by Voots et al. [1977]. Each point represents a 10-minute average obtained while IMP-6 was in the AKR emission cone (black shading in Figure 2) which was determined by Green et al. [1977]. The linear correlation coefficient of the log of the AKR power flux versus the log of the AE index was found to be 0.51.

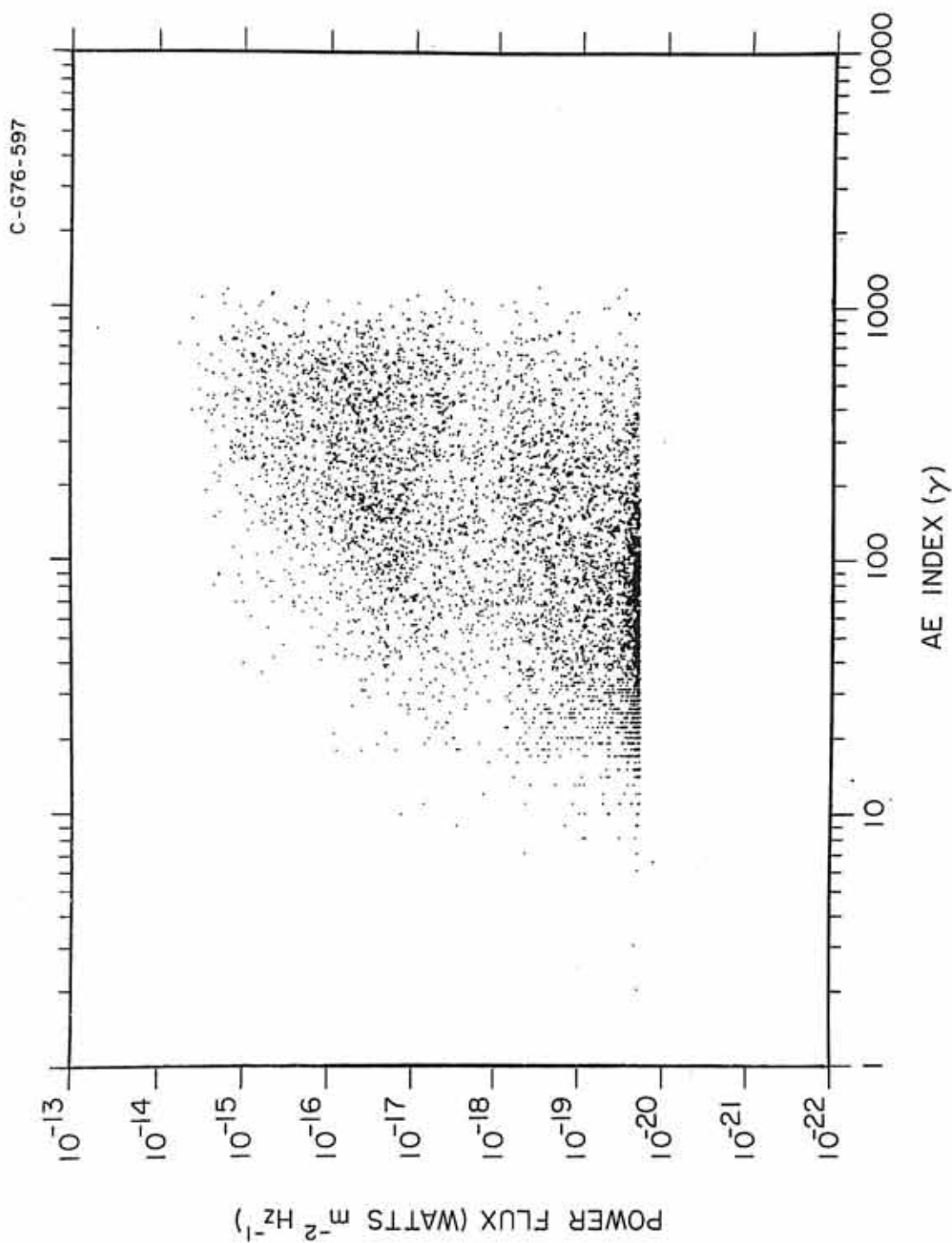


Figure 4

Figure 5 Two dimensional polar plots of the intensity distribution of the AKR emission cone in the northern hemisphere are shown in two latitude and local time coordinate systems. The third dimension, radial distance, is taken into account by applying a  $1/R^2$  scaling to the power flux measurements relative to the origin of each coordinate system and normalizing to  $7 R_E$  about the origin. The left-hand panel has organized all the Hawkeye and IMP-6 observations in the familiar earth-centered system of magnetic latitude and magnetic local time. The best representation of the intensity distribution of the AKR emission cone (shaded) is found in the source-centered plot (right-hand panel) where all the observations are transformed into a coordinate system with the average source region of AKR at the origin. The average source region used is consistent with the results of Gallagher and Gurnett [1979].

## AKR EMISSION CONE AT 178 KHz

EARTH CENTERED

SOURCE CENTERED

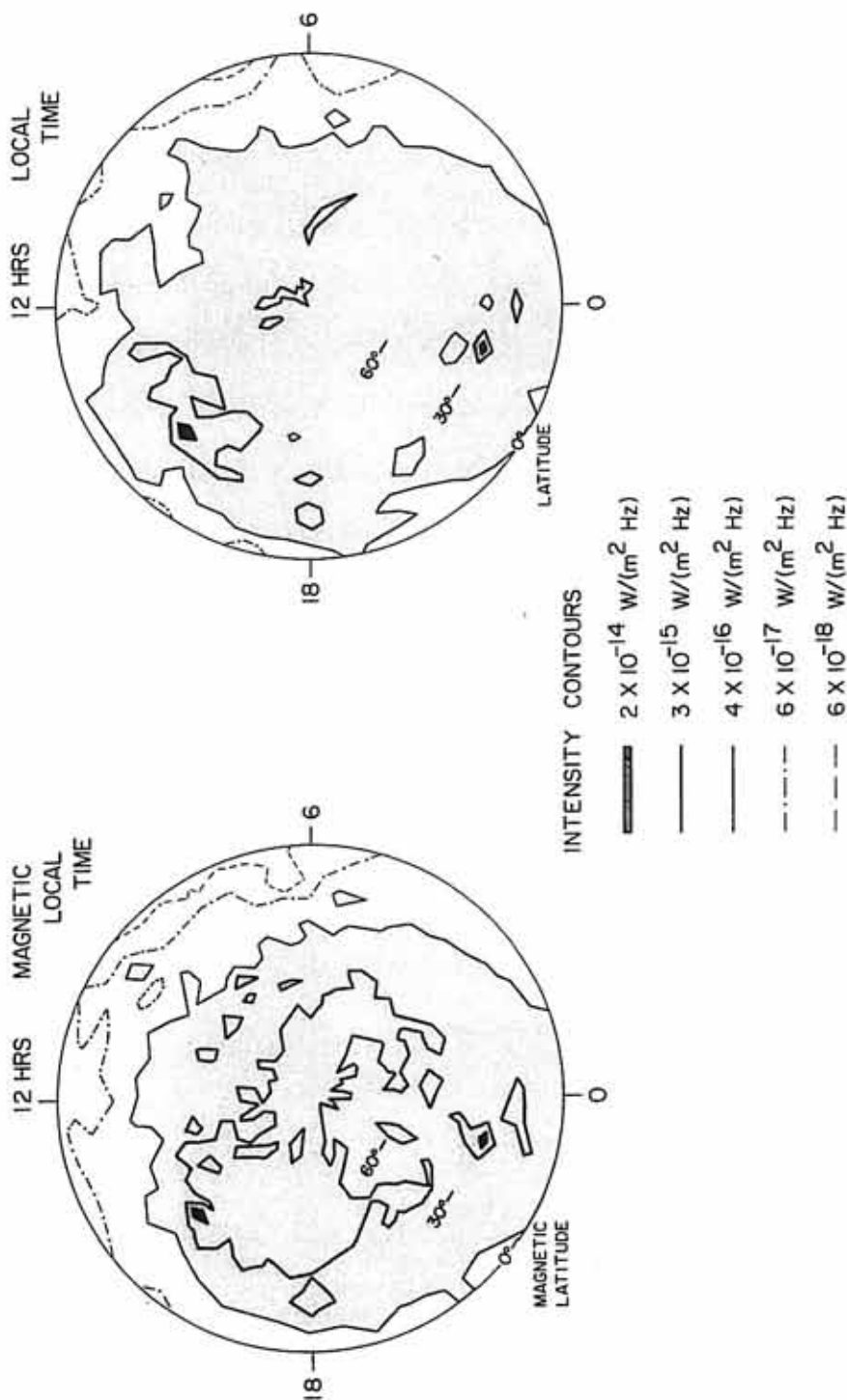


Figure 5

Figure 6

The source-centered AKR emission cone at 178 kHz is shown in greater detail at five representative local times. Note the rapid drop in the average power flux intensity (2 to 3 orders of magnitude) as a function of decreasing latitude for the 8.5 and 4 hours local time side panels. There is less than 10 db variation in the averaged intensity in almost all of the emission cone as illustrated in the 18.5 and 0.5 hours local time side panels. Unlike the intense decametric radio emissions from Jupiter which are believed to be generated into a large hollow cone its terrestrial counterpart, auroral kilometric radiation, is beamed into a nearly homogenous emission cone.

D-G79-309-1

## SOURCE CENTERED EMISSION CONE AT 178 kHz

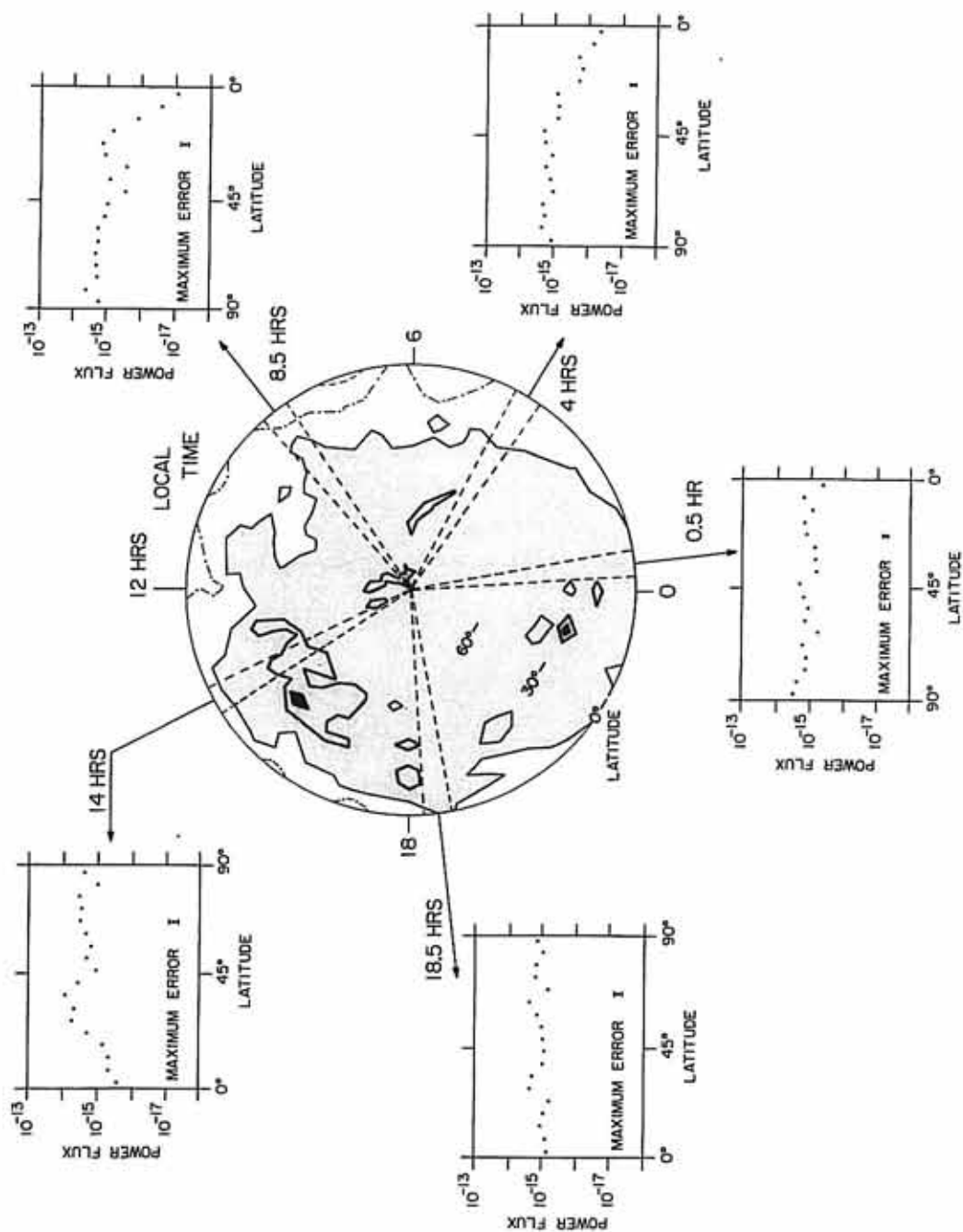


Figure 6

Figure 7

The top panel presents simultaneous  $(R/7 R_E)^2$  normalized (with respect to the average AKR source region, see text) power flux measurements from the Hawkeye and IMP-6 spacecrafts. The bottom shows the trajectories of these two satellites in the emission cone (crossed-hatched boundaries) during the time of the simultaneous observations. All enhanced emissions observed by Hawkeye are attributed to auroral kilometric radiation. When IMP-6 is in the emission cone (after  $\sim 23$  hours universal time) both satellites observe nearly identical AKR power flux illustrating that the source of auroral kilometric radiation illuminates the entire emission cone uniformly and simultaneously.

C-679-301-1

SEPTEMBER 19, 1974

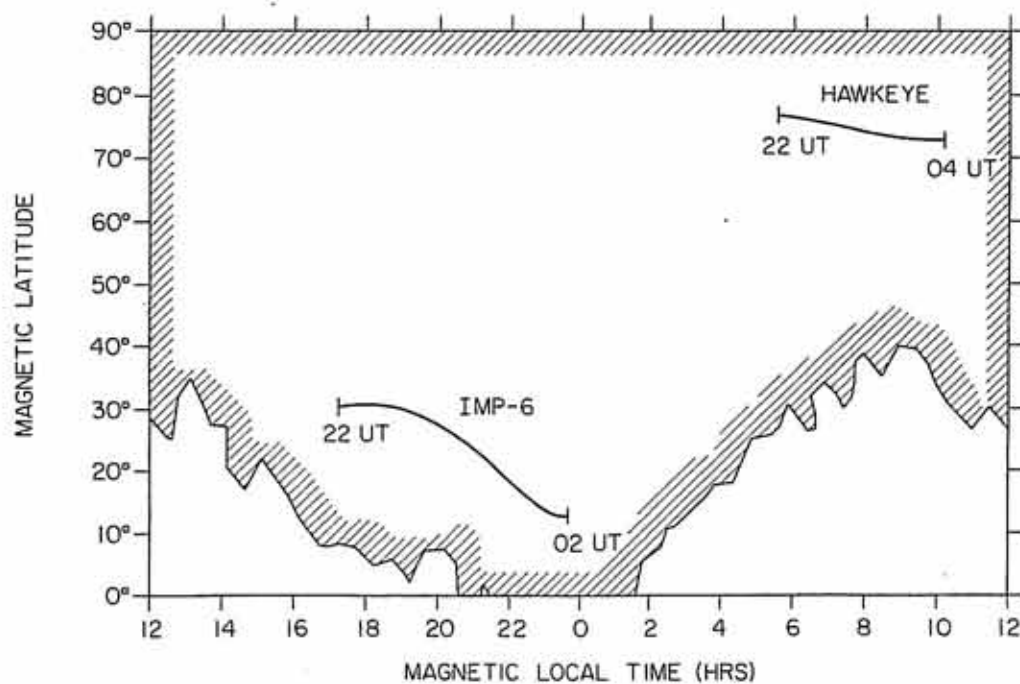
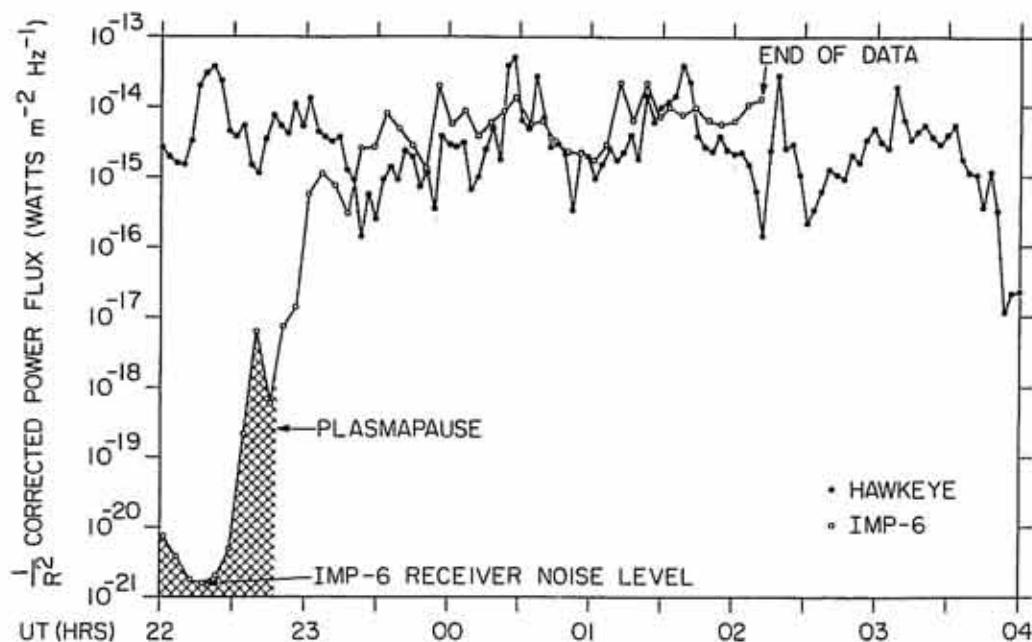


Figure 7



Figure 8      The three panels (A, B, and Z) on the right-hand side are plots of the measured ambient magnetic field ( $B_M$ ) from the triaxial sensors on board Triad minus a theoretical geomagnetic field ( $B_T$ ) in units of gammas. The large perturbation from the baseline formed by the  $B_M - B_T$  curve in the A panel is attributed to two east-west field-aligned current sheets. The left-hand side illustrates the orientation of the A, B, and Z magnetic field sensors onboard Triad during a pass over College, Alaska. The direction of the magnetic field sensors is used in determining the orientation of the auroral zone current sheets.

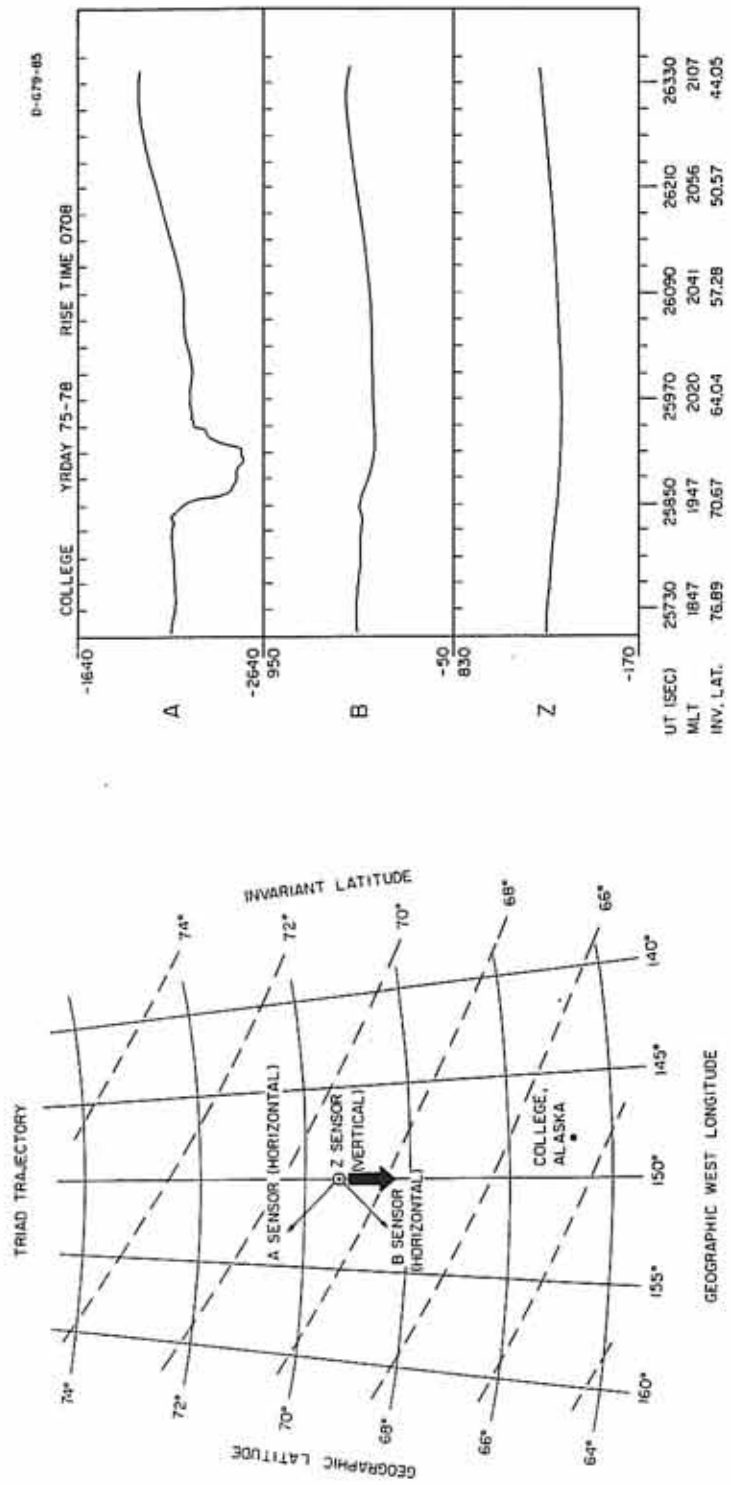


Figure 8

Figure 9

A polar plot in magnetic local time and invariant latitude of field-aligned currents observed by Triad during weakly disturbed times ( $|AL| < 100\gamma$ ) from Iijima and Potemra [1976]. The crossed-hatched section from 19 hours to 01 hours is the magnetic local time region where the most intense bursts of AKR are believed to originate. Note, also, that this is the region where the most complicated auroral zone current system is found. Only Triad magnetometer measurements inside the crossed-hatched region will be used in this study.

C-678-788

## FAC'S DURING WEAKLY DISTURBED CONDITIONS

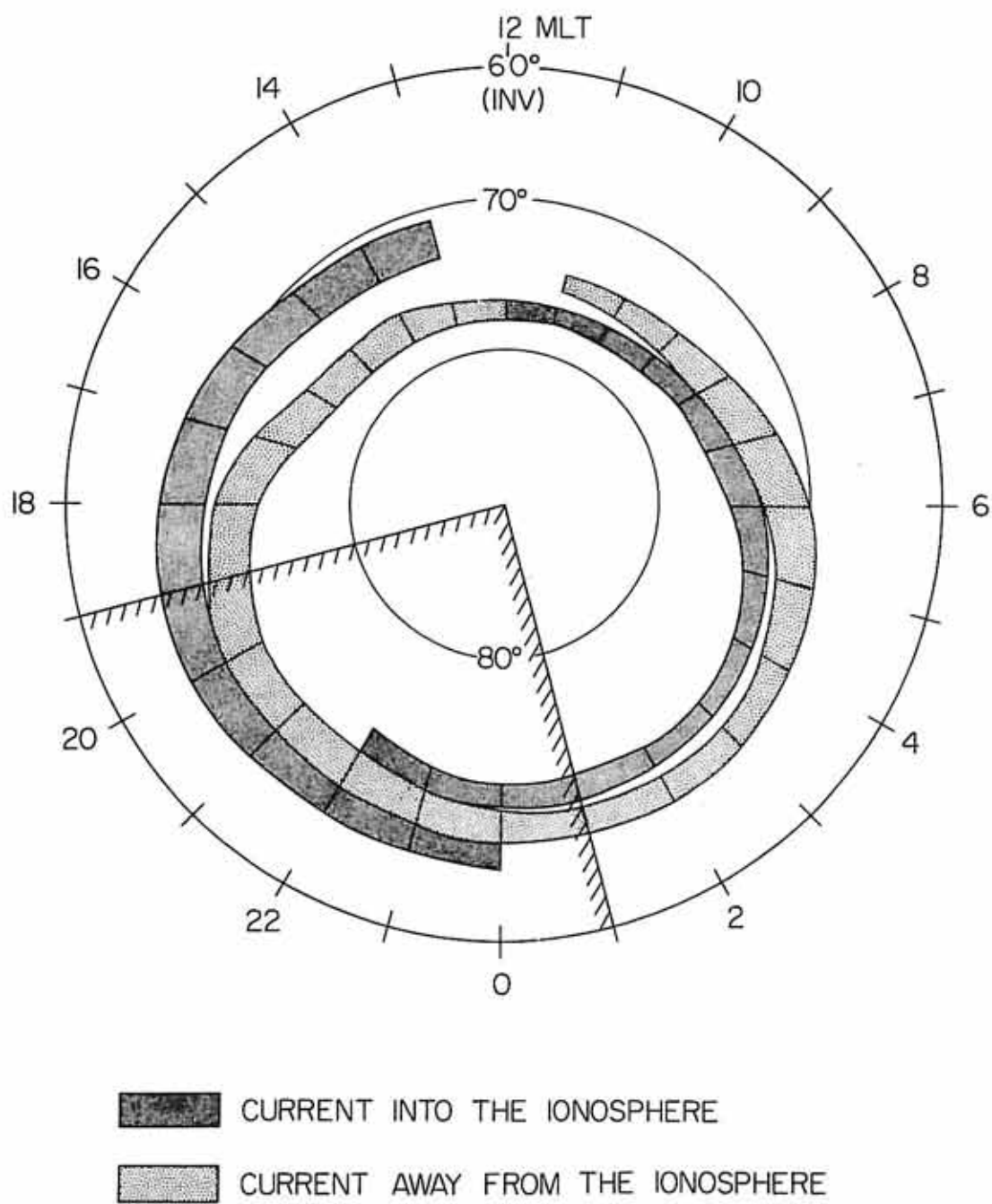


Figure 9

Figure 10

The top panel shows power flux measurements as a function of time from the Hawkeye satellite while it is in the AKR emission cone during the four consecutive passes of the Triad spacecraft through the auroral oval in the northern hemisphere. The Triad magnetometer measurements from the A sensor plotted with respect to the baseline formed by  $B_M - B_T$  are shown in the bottom panels A, B, C, and D. Note that when Triad observes large deflections in the magnetic field due to field-aligned currents Hawkeye observes intense kilometric radiation (times B, C, and D) but when little disturbances in the auroral zones are found, Panel A, Hawkeye does not detect kilometric radiation above the receiver's threshold.

JULY 23, 1974

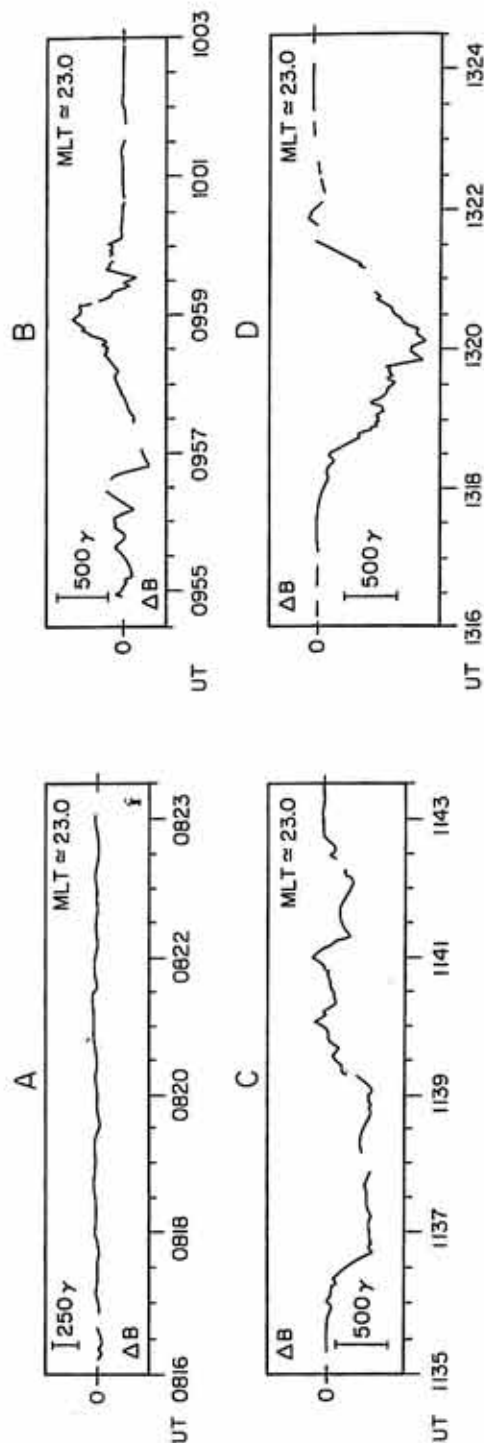
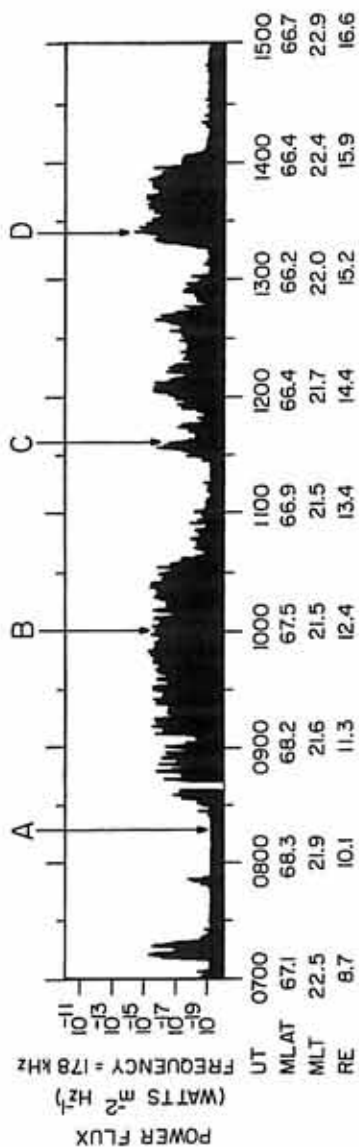


Figure 10

Figure 11 Simultaneous power flux measurements of AKR at 178 kHz versus the integrated current intensity of auroral zone field-aligned currents. A  $(R/7 R_E)^2$  normalization to the power flux measurements is applied to take into account the radial dependence of this radiation. The R variable is the distances from the satellite to the average source region of AKR (see text). The triangles represent an upper limit to the power flux since AKR was not detected at those times. A correlation can be seen in that, as the power flux increases so does the integrated current sheet intensity of field-aligned currents.

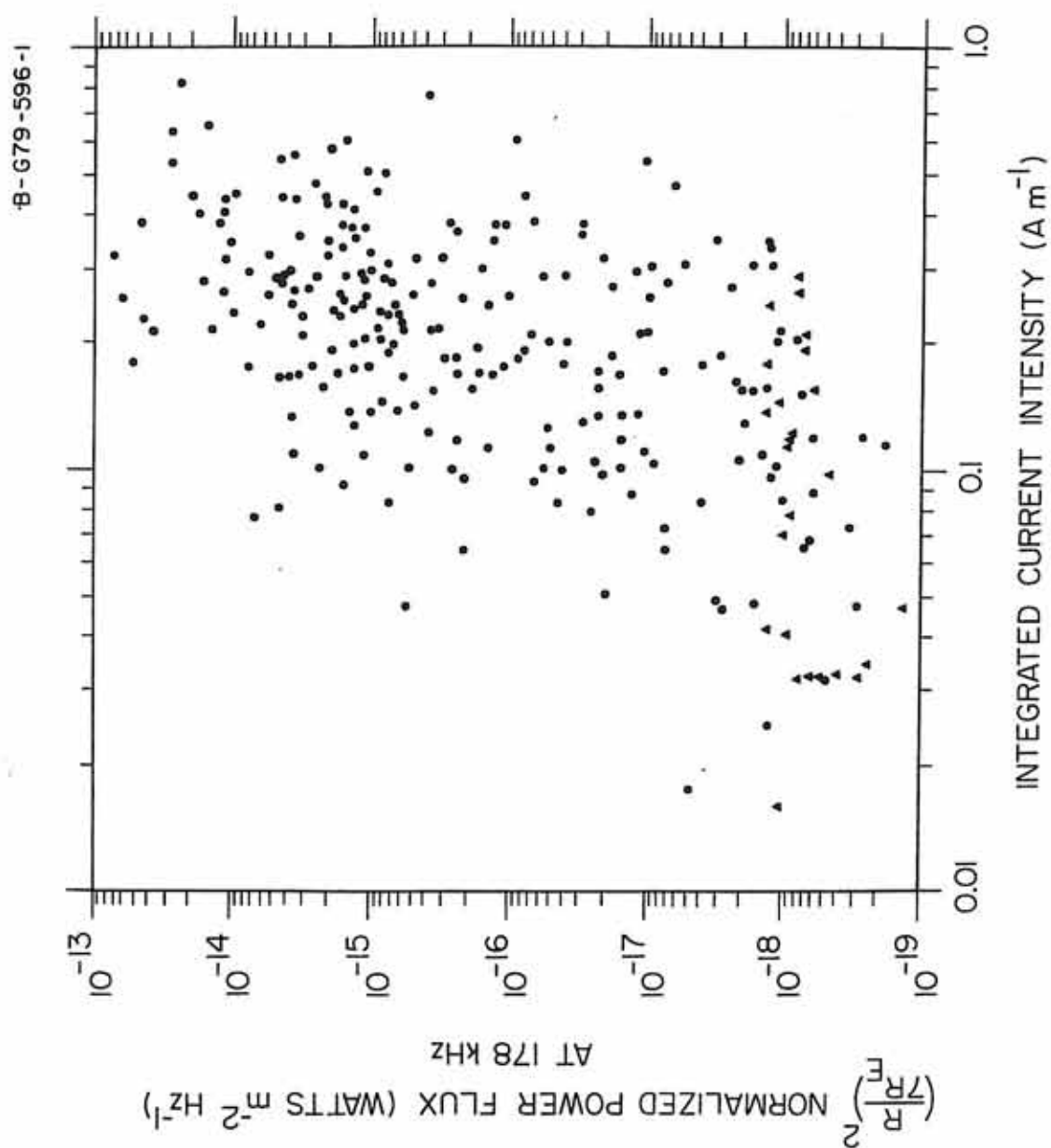


Figure 11



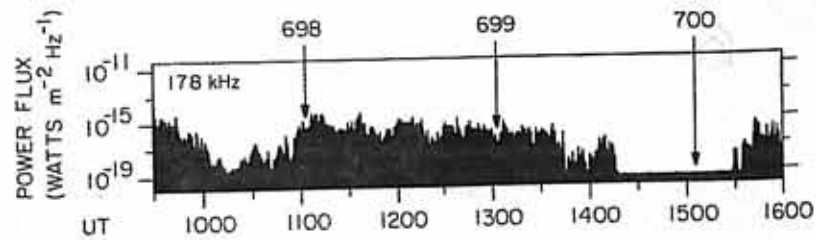
Figure 12

The top panel shows electric field measurements as a function of time from Hawkeye while it is in the AKR emission cone during three consecutive AE-D auroral zone passes. The panels labeled orbit 698, 699, 700 are energy-time spectrograms from the LEE experiment onboard AE-D. Note that AKR appears to be more closely related to inverted-V electron precipitation than to plasma sheet precipitation.

D-678-839-1

DECEMBER 5, 1975

## HAWKEYE ELECTRIC FIELD INTENSITIES



## AE-D ELECTRON FLUXES

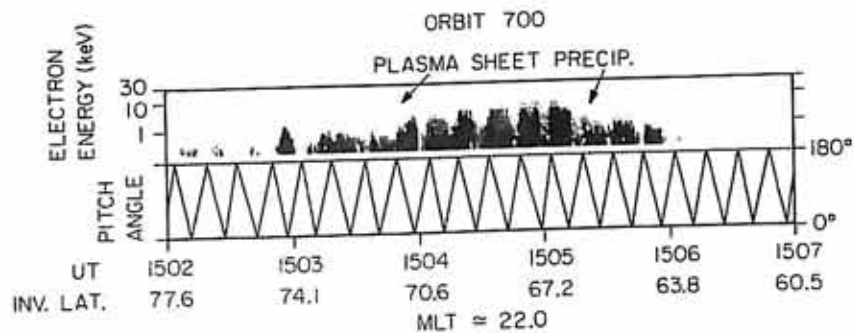
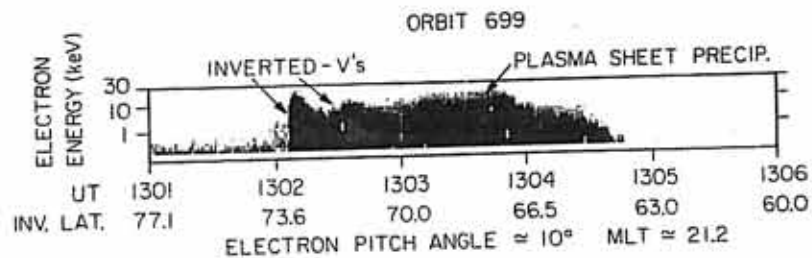
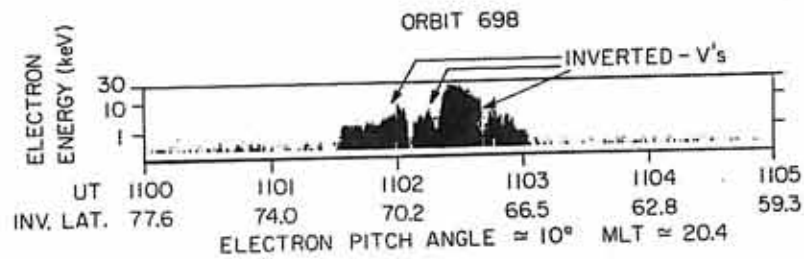


Figure 12

Figure 13 Scatter plot of simultaneous measurements of AKR intensity (normalized to  $7 R_E$  and having a  $1/R^2$  scaling) and the peak energy in inverted-V events observed by AE-D. The correlation coefficient between the log of the power flux and the peak energy is 0.65.

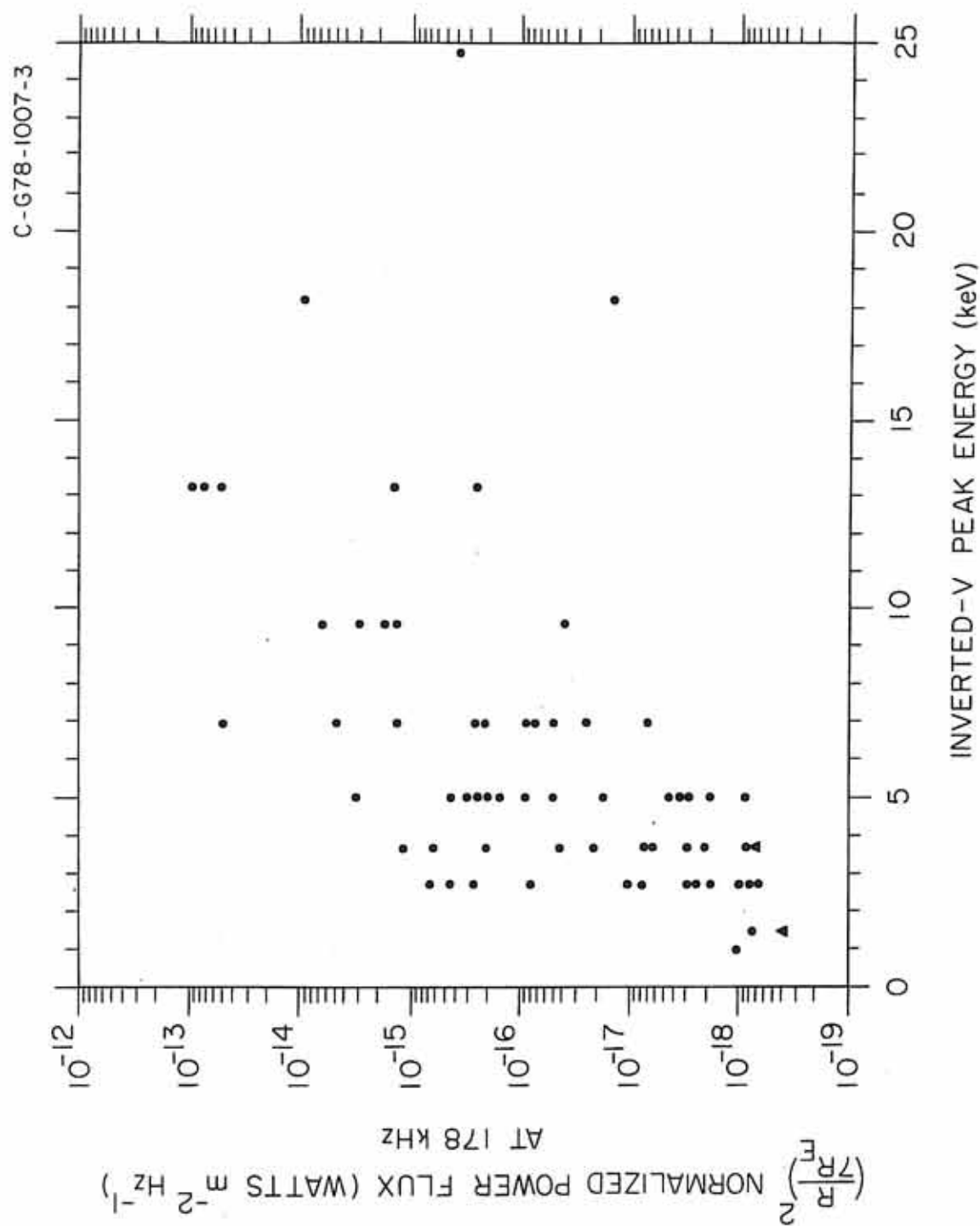


Figure 13

Figure 14 Three electron distribution functions at  $\sim 0^\circ$  pitch angle ( $\pm 7\ 1/2^\circ$ ) during the inverted-V events used in Figure 13. In the upper right corner of each panel is the simultaneous AKR power flux measurement from the Hawkeye spacecraft. These three distribution functions are representative of the AE-D observations during times of weak (top panel), moderate (center panel), and intense (bottom panel) auroral kilometric radiation.

D-679-201-2

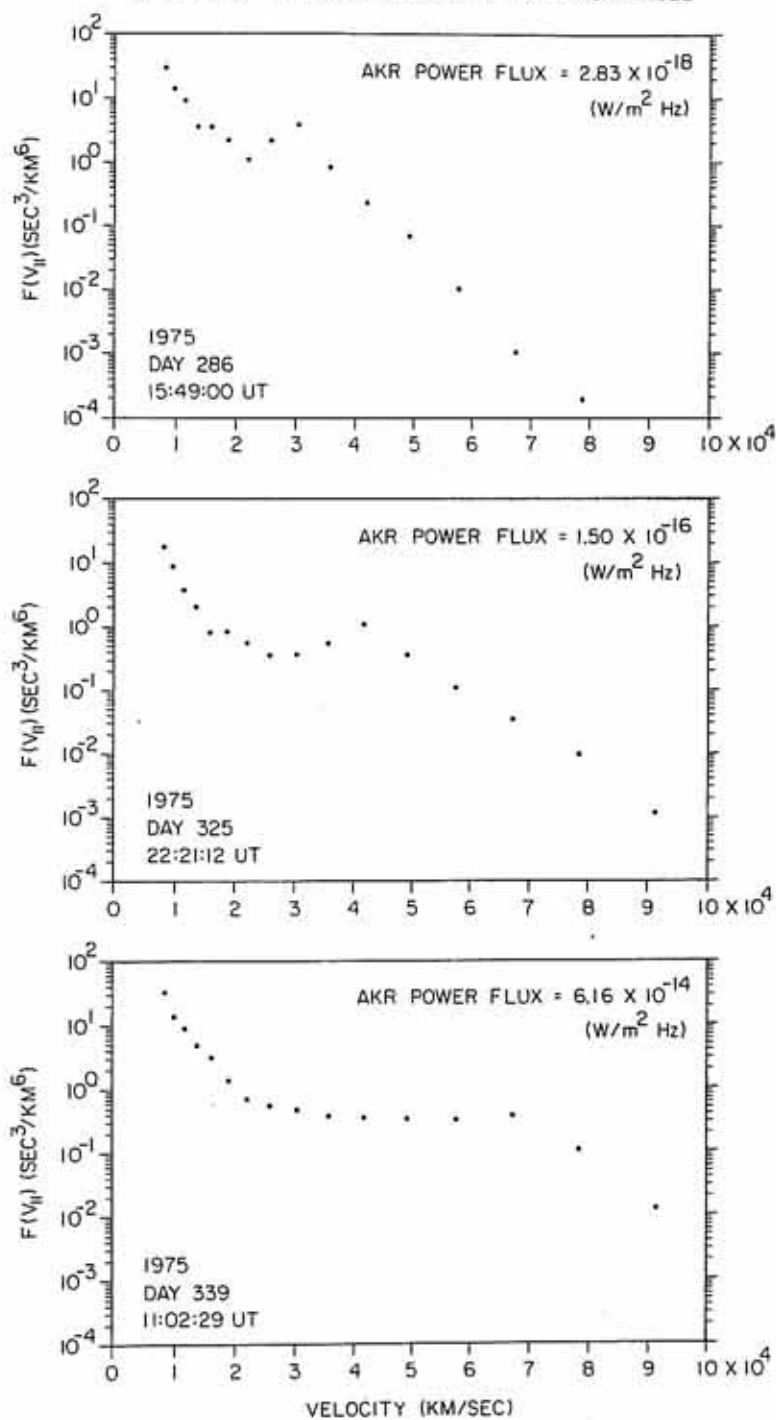
AE-D ELECTRON DISTRIBUTIONS AT  $-0^\circ$  PITCH ANGLE

Figure 14

Figure 15

Scatter plot of the  $(R/7 R_E)^2$  normalized AKR intensity at 178 kHz and the effective tail temperature ( $T_{||}$  defined in text) of the electron distribution functions at  $\sim 0^\circ$  pitch angle of the inverted-V events used in Figure 13. The triangles represent times when auroral kilometric radiation was not detected above the receivers threshold. During times when the power flux is weak ( $< 10^{-17}$  watts/( $m^2 Hz$ ))  $T_{||}$  is less than  $1.8 \times 10^8$  °K. In addition, for  $T_{||}$  greater than  $1.8 \times 10^8$  °K the associated AKR power flux is moderate ( $10^{-17}$  to  $10^{-15}$  watts/( $m^2 Hz$ )) to intense ( $> 10^{-15}$  watts/( $m^2 Hz$ )).

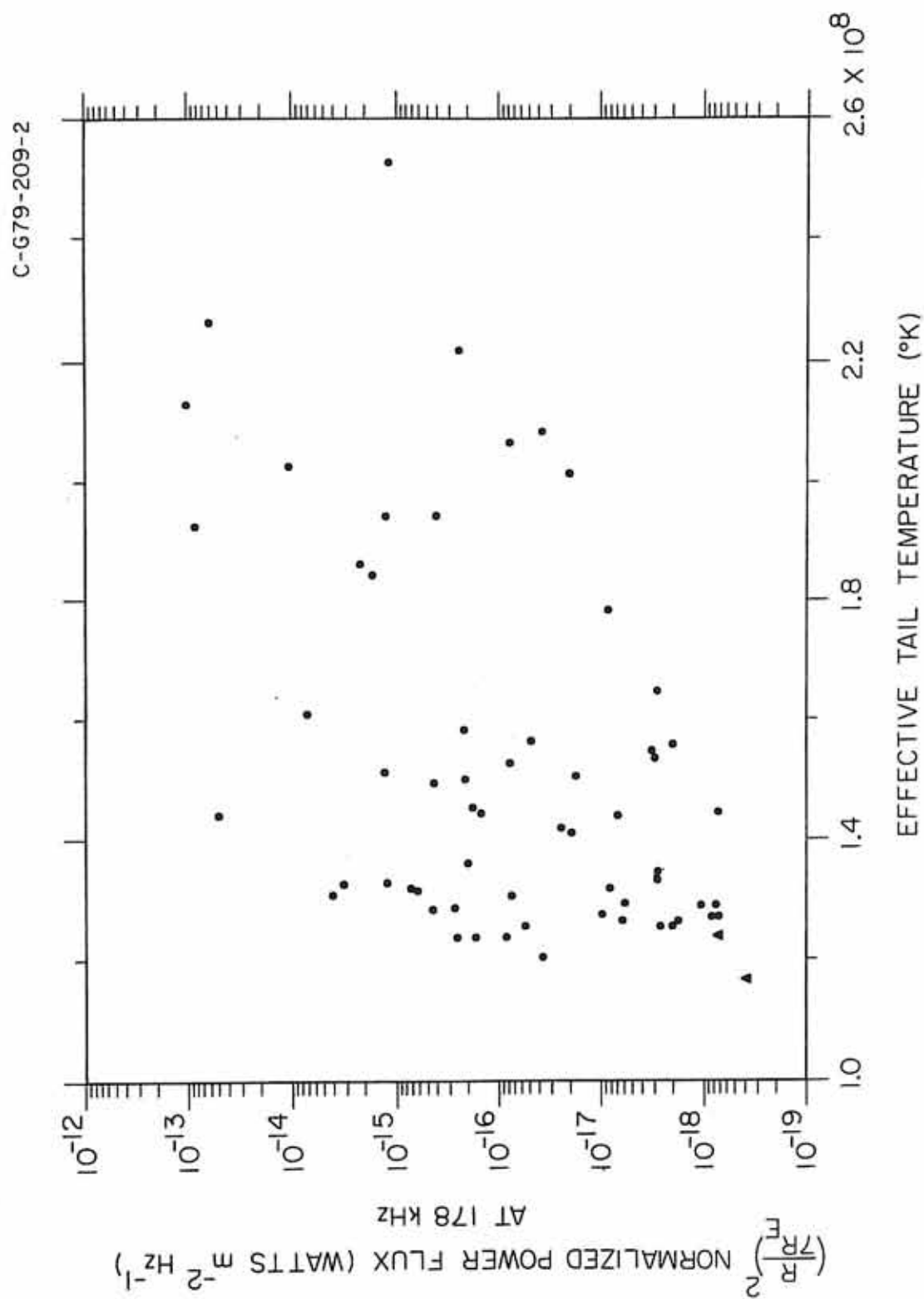


Figure 15



Figure 16

Scatter plot of simultaneous measurements of AKR intensity at 178 kHz (normalized to  $7 R_E$  and having a  $1/R^2$  scaling) and the energy flux of the same inverted-V events plotted in Figures 13 and 15. The top scale is an estimate of the amount of power available in the precipitating inverted-V events. The far right hand scale is an estimate of the amount of power in the AKR bursts. Note that if the precipitating inverted-V events are the sole energy reservoir for AKR that the generation mechanism can have a maximum efficiency of about 1%.

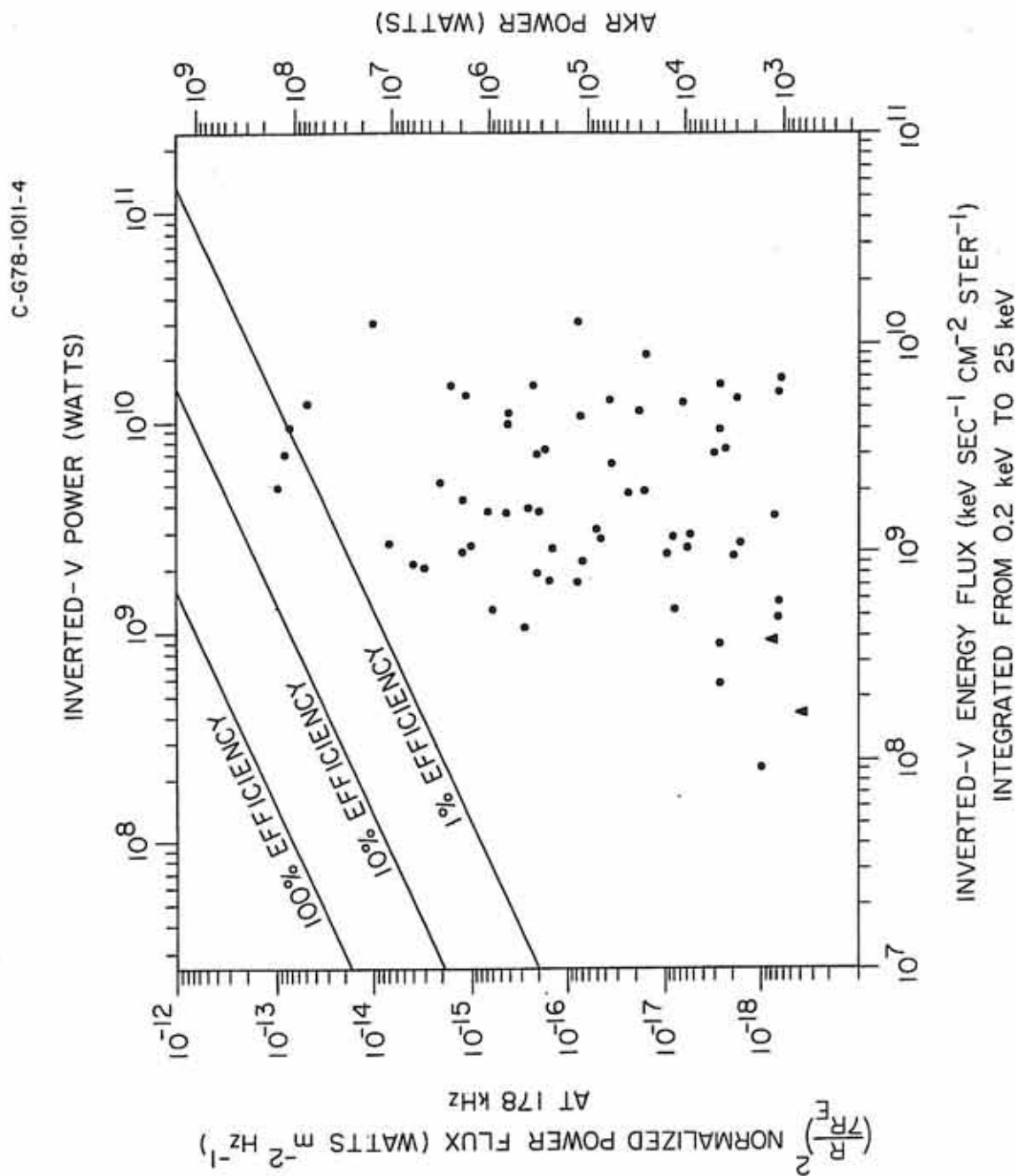


Figure 16

Figure 17 Scatter plot of simultaneous measurements of AKR intensity at 178 kHz (normalized to  $7 R_E$  and having a  $1/R^2$  scaling) versus the energy flux of the inverted-V events in Figure 16 integrated from 6.88 keV to 25 keV. If the high energy tail in the distribution function of the precipitating inverted-V events plays a major role in the generation or amplification of auroral kilometric radiation then efficiencies as high as 0.1 to 1% may be possible for a dynamic range in AKR intensity as large as 40 db.

C-G79-222-1

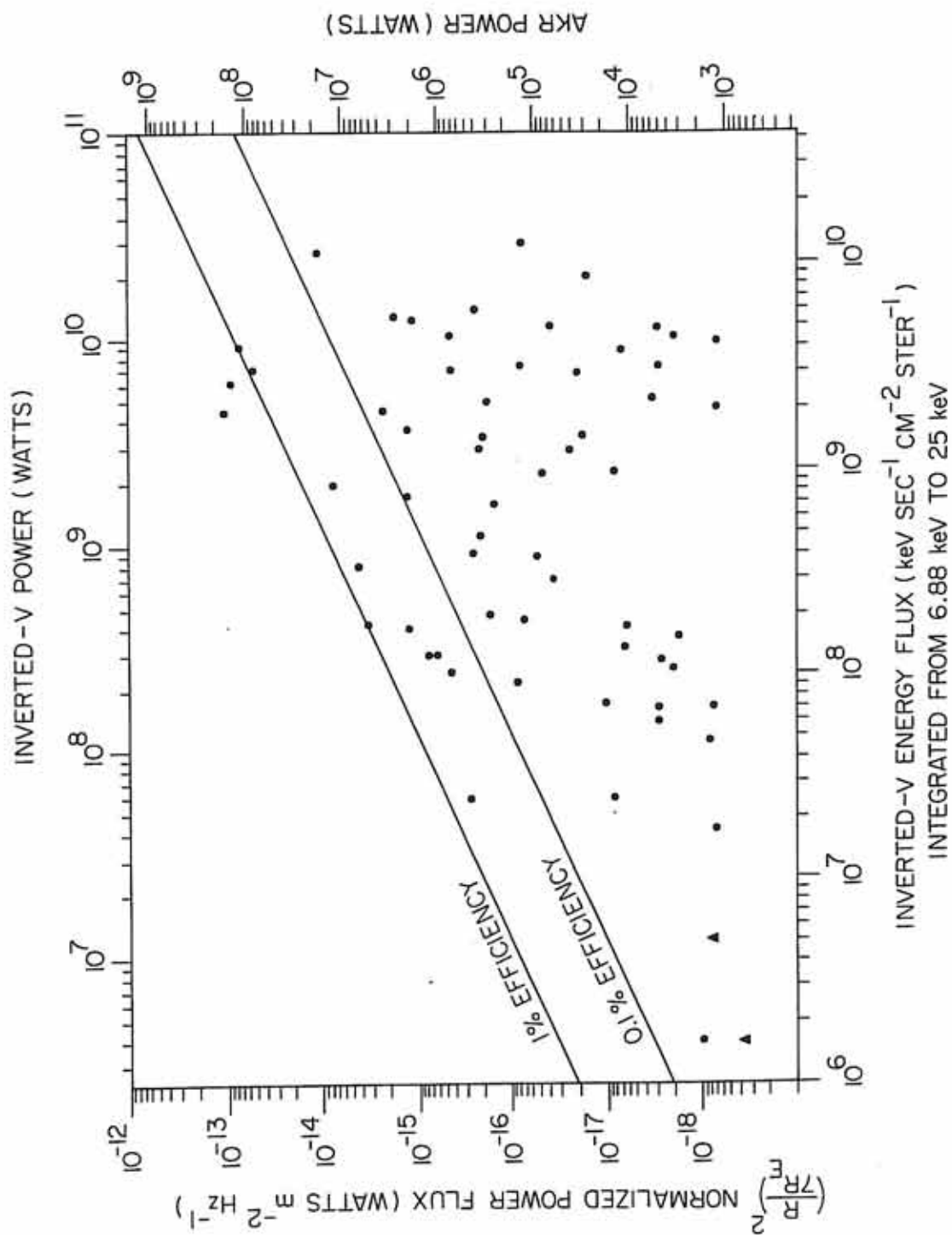


Figure 17

Figure 18

The main feature of intense auroral kilometric radiation observed by Hawkeye during low altitude auroral zone passes is that it occurs in regions where the wave frequency (178 kHz in this case) is greater than both the local electron gyrofrequency and the local electron plasma frequency. The dashed line marked  $f_g^-$  is the measured local electron gyrofrequency. The electron plasma frequency,  $f_p^-$  is estimated on the basis that it is the low-frequency cutoff of the continuum radiation and the upper-frequency cutoff of the auroral hiss.

C-677-227-1

HAWKEYE-I, DAY 132, MAY 11, 1976

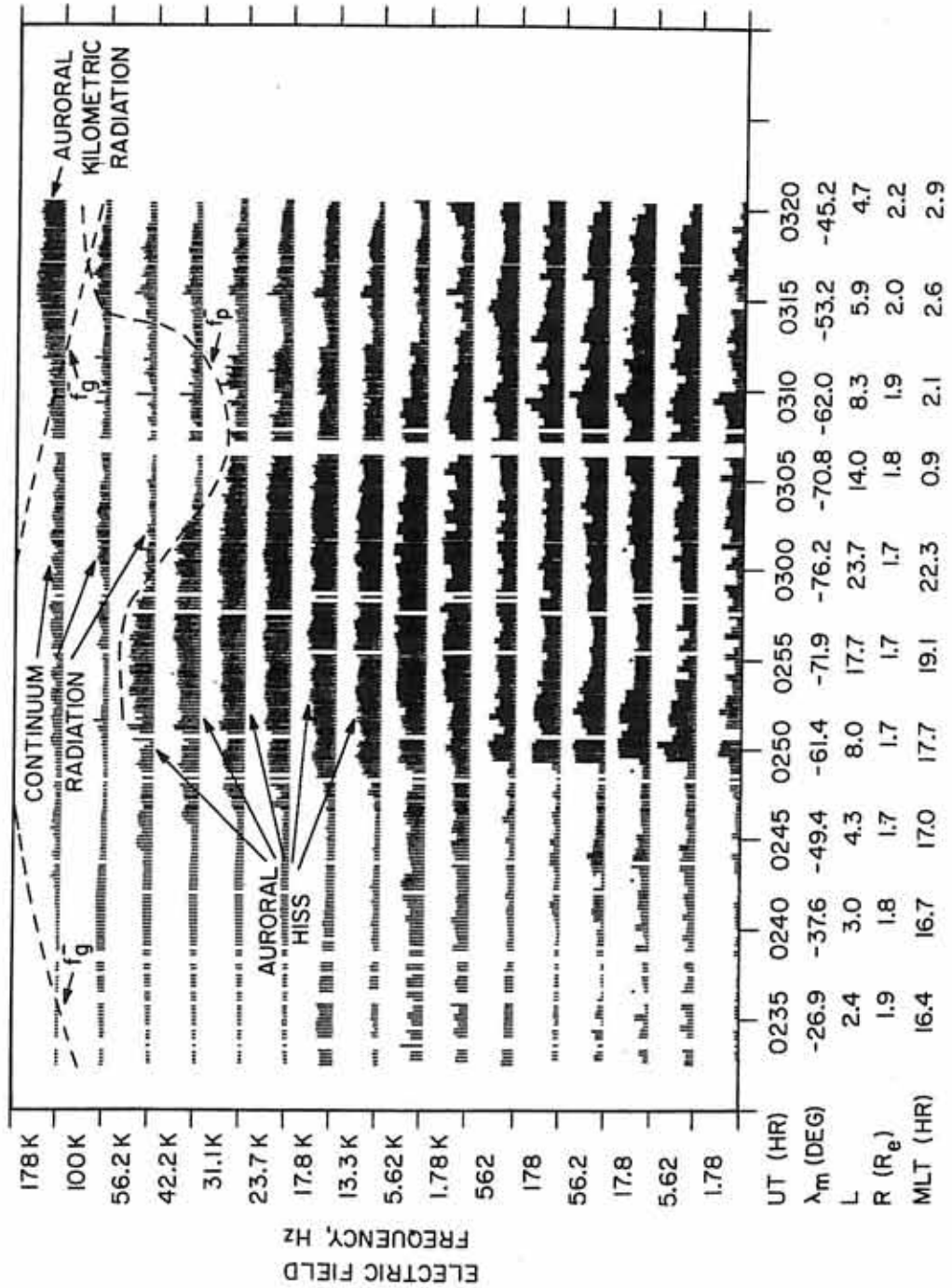


Figure 18

Figure 19

A scatter plot of electric field measurements at 178 kHz from Hawkeye southern passes on the night-side of the earth plotted as a function of the ratio of the wave frequency to the local electron gyro-frequency ( $f/f_g^-$ ). The maximum electric field of AKR measured is nearly 12 mV/m. Note that there is a sharp cutoff of at least five orders of magnitude in the AKR intensity at the local electron gyro-frequency. To clearly illustrate the cutoff of AKR at  $f_g^-$  passes for which intense auroral hiss emissions at 178 kHz occurred were eliminated. Virtually all the data below  $10^{-16}$  watts/(m<sup>2</sup>Hz) is continuum radiation which displays no cutoff at  $f = f_g^-$ .

C-679-160-1

NIGHT SIDE DATA  
18 TO 6 HOURS MAGNETIC LOCAL TIME

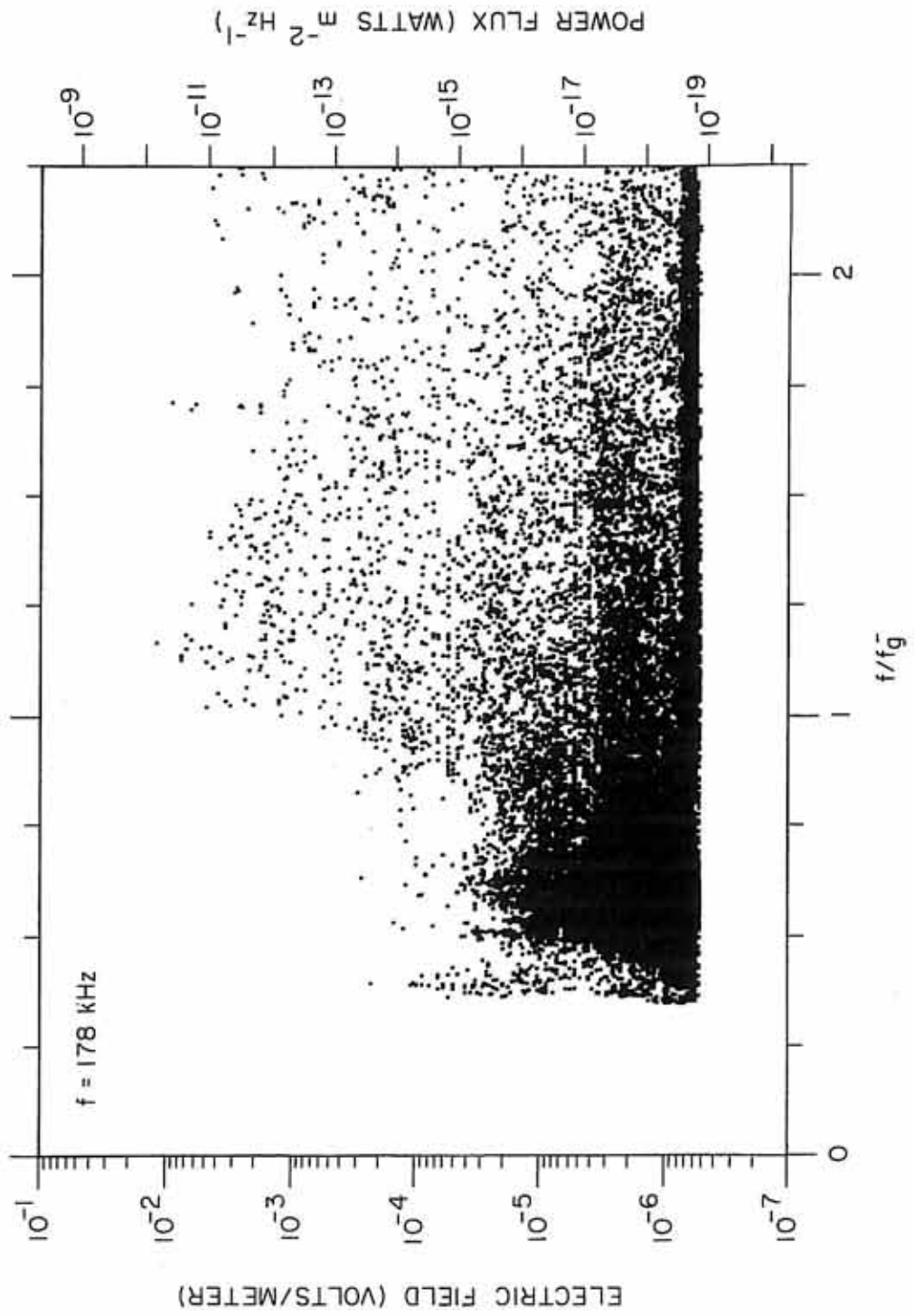


Figure 19



Figure 20

The expected radial variations of  $f_p^-$ ,  $f_g^-$ , and  $f_{R=0}$  along an auroral magnetic field line. The frequencies  $f_p^-$  and  $f_{R=0}$  present propagation barriers or cutoffs to downward propagating radiation with left-hand (L-O) and right-hand (R-X) polarizations, respectively. Note that in regions where  $f_p^- \ll f_g^-$  then  $f_g^- \approx f_{R=0}$ .

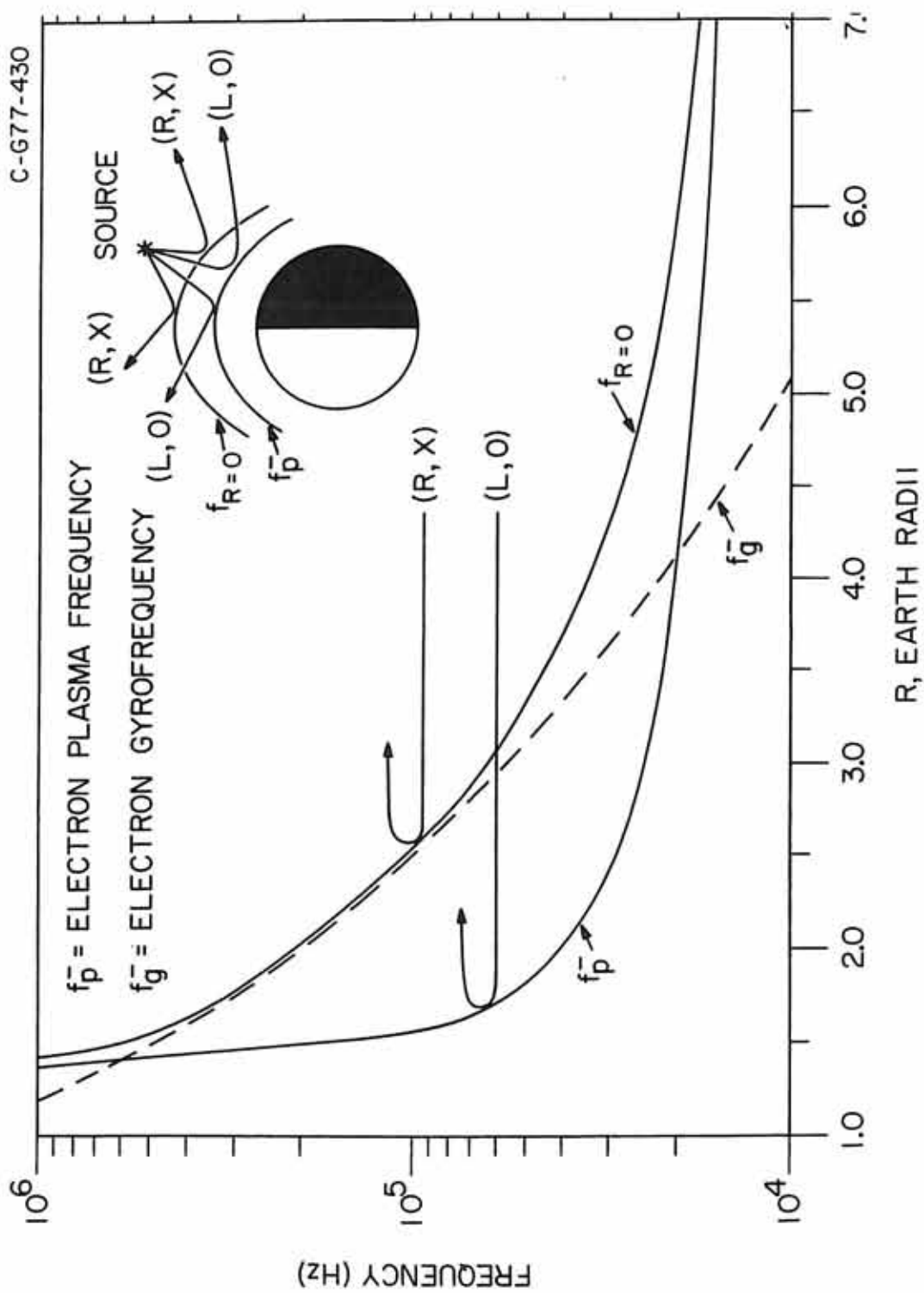


Figure 20

Figure 21

The top and bottom panels are contour plots of typical electron distribution functions  $F(v)$ , in velocity space used in the theories of Wu and Lee [1979] (top panel) and Melrose [1976] (bottom panel) for the generation of AKR. In the bottom panel the source of free energy for AKR amplification is in the precipitating portion of  $F(v)$ . The contour at  $1 \text{ sec}^3/\text{km}^6$  shows the shape of a high velocity precipitating beam (large  $V_{||}$ ) which also extends to large perpendicular velocities. In the top panel the source of free energy is in the ascending part of  $F(v)$ . This distribution has a loss-cone feature which is characterized by a depletion of upgoing electrons having small pitch angles (small  $V_{\perp}$ ).

C-679-484-I

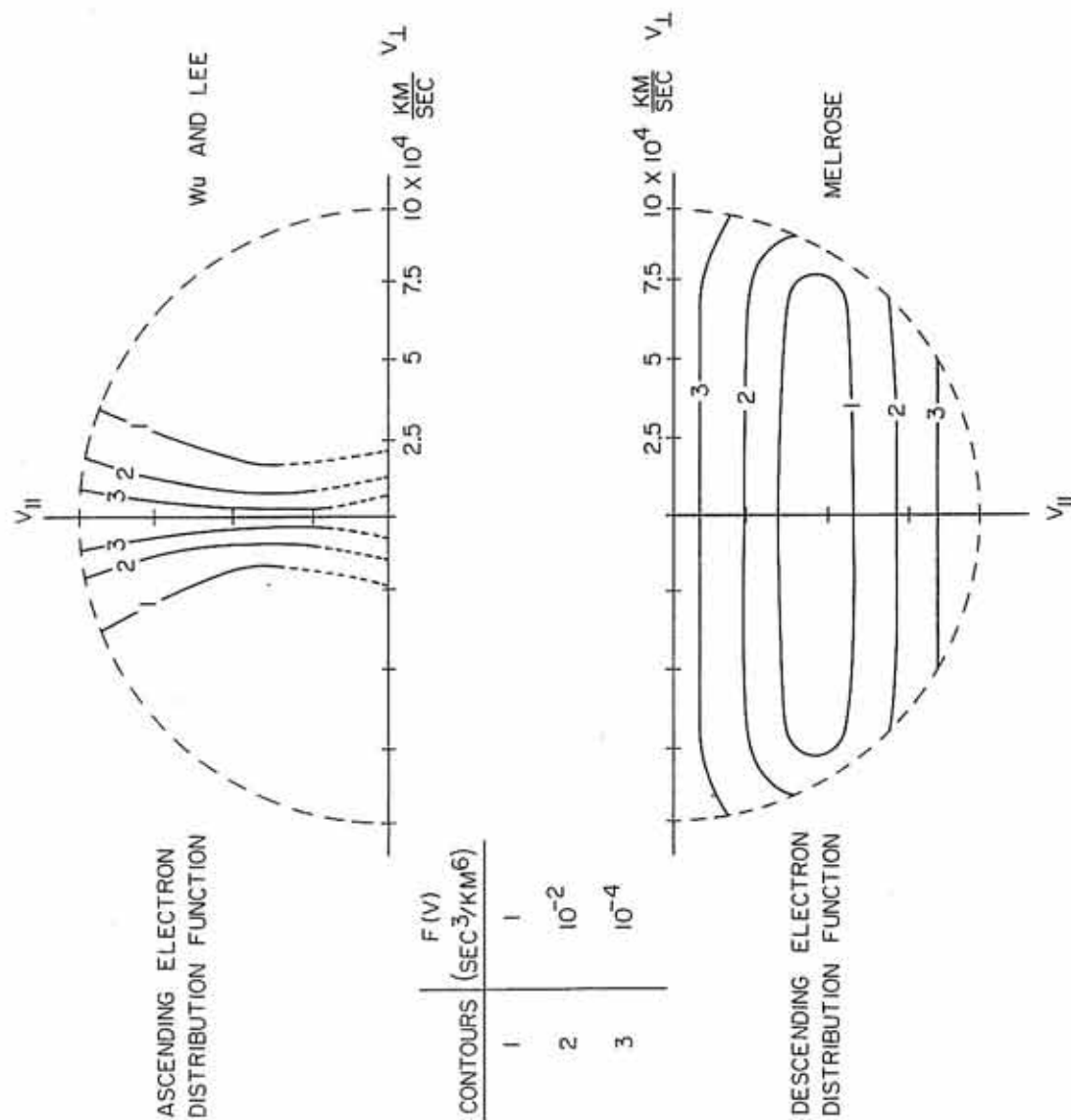


Figure 21

Figure 22

On the left-hand side are three contour plots of inverted-V electron distribution functions in velocity space observed by AE-D. These three distributions are associated with weak (top), moderate (center) and intense (bottom) auroral kilometric radiation observed simultaneously by Hawkeye. The corresponding energy flux of each distribution as a function of pitch angle is shown on the right-hand side. Note that in the precipitating portion of the distribution functions (from 0 to  $90^\circ$ ) there is at least an order of magnitude more energy than in the ascending portion (from  $90^\circ$  to  $180^\circ$ ). The high velocity beam or peak in the distribution functions, nearly centered about zero degrees pitch angle, is a characteristic feature of inverted-V electron distributions.

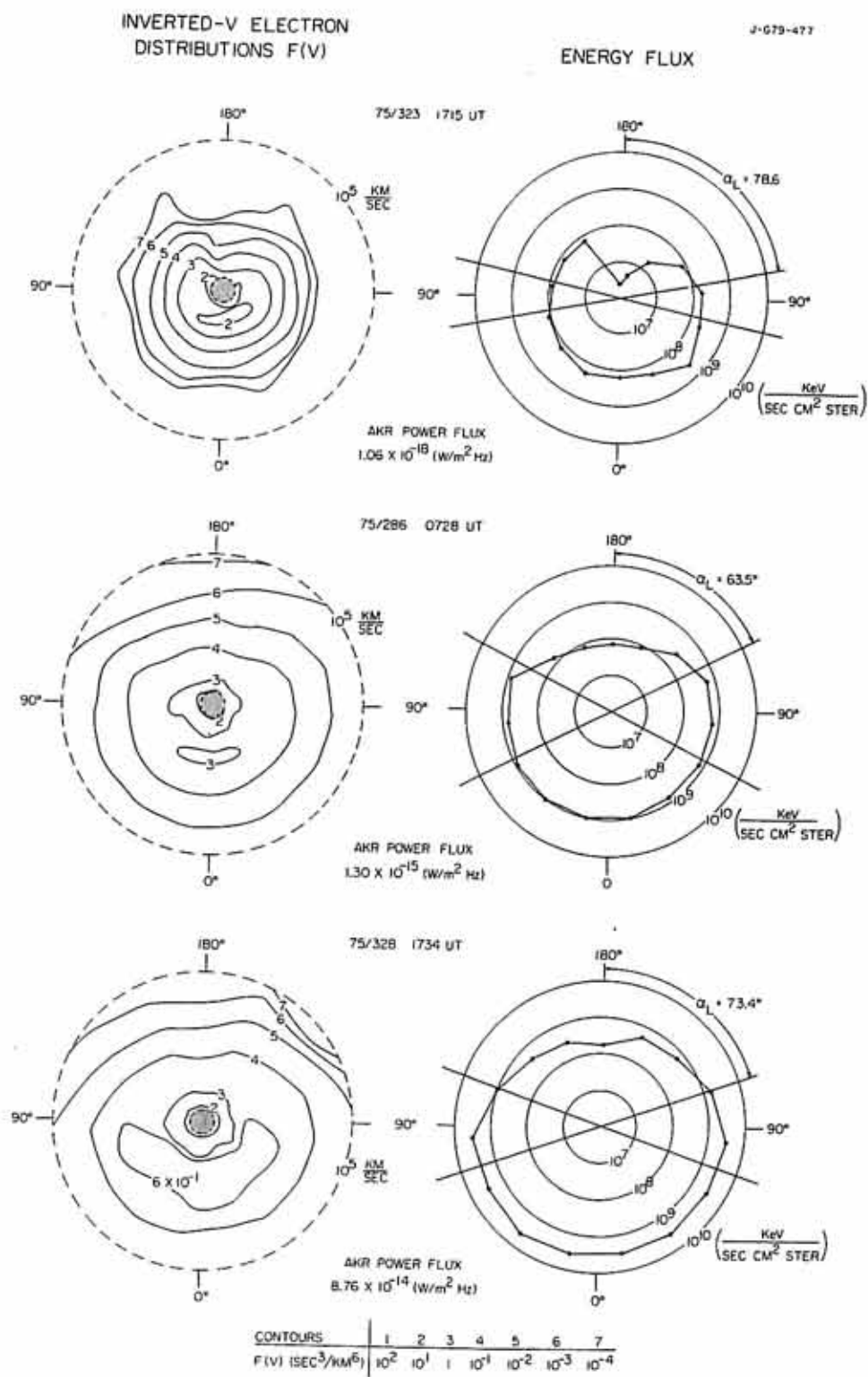


Figure 22

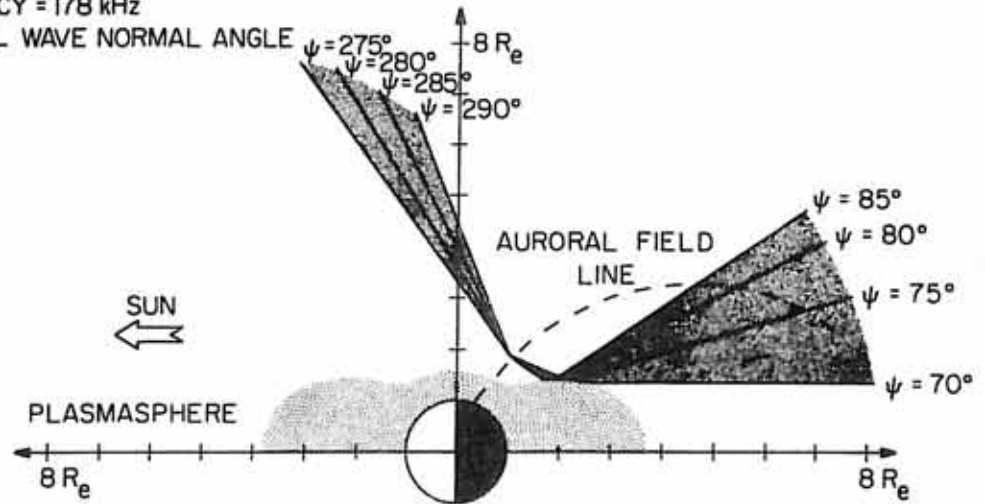
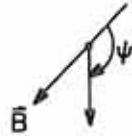
Figure 23 Ray paths in the noon-midnight meridian for the Melrose (bottom panel) and the Wu and Lee (top panel) generation mechanisms in the model magnetosphere shown in Figure 20. The resultant angular distribution for Melrose's mechanism (shaded region, bottom panel) is that of a filled-in emission cone and agrees well with the observations (see Figure 5 or 6). However, in the absence of near source propagation effects the Wu and Lee mechanism (shaded region, top panel) produces a hollow emission cone.

C-679-623

### WU AND LEE ANGULAR DISTRIBUTION

FREQUENCY = 178 kHz

$\psi$  = INITIAL WAVE NORMAL ANGLE



### MELROSE ANGULAR DISTRIBUTION

FREQUENCY = 178 kHz

$\theta$  = INITIAL WAVE NORMAL ANGLE

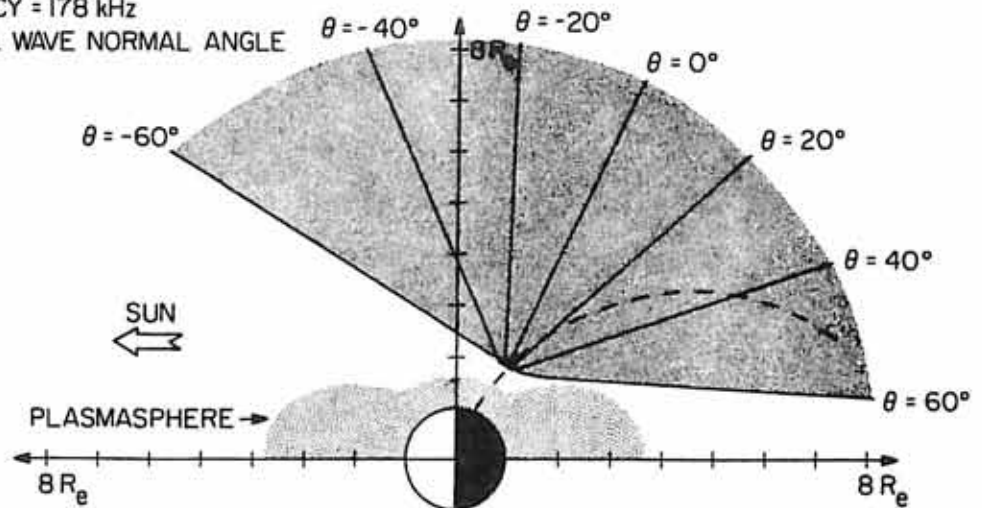
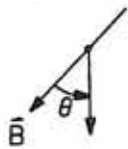


Figure 23